

UNIVERSITY OF TRENTO
Department of Mathematics



PhD school in Mathematics (25th cycle)

Doctor of Philosophy Dissertation

Mathematical modelling of transport across blood vessel walls

Supervisors:

Prof. E. F. Toro
Prof. A. Bellin

PhD student:

Laura Facchini

Trento, 2013

Abstract

The last decade has seen an increasing interest in bio-mathematical modelling and scientific computing, resulting in new applications to relevant physiological phenomena and to a better understanding of the origin of various diseases. A topic of great interest to several degenerative diseases is filtration across microvessel walls. The role of the microvessel wall is to let oxygen and nutrients contained in the blood stream to reach the interstitium, and ultimately the surrounding cells, while blocking macromolecules. An understanding of these processes is important in preventing and curing neuro-degenerative diseases, as well as for exploring possible mechanisms to make drug delivery more efficient. This work presents a one-dimensional, time dependent mathematical model describing transport of blood plasma and macromolecules across blood vessel walls. The model takes into account the heterogeneous microvessel wall composition, in order to accurately describe trans-vascular flow. This results in a multi-layered domain, accounting for variable physical properties across the layers forming the micro-vascular wall. In particular, the glycocalyx and endothelium, accounted for in many biological studies, are represented in our model. This micro-structural, yet simplified description of the vascular wall, allows us to simulate the effect of glycocalyx damage and of other pathologies, such as hypertension, hemorrhage and hypovolemia, both in steady and time-dependent states. Due to the simplicity, and thus efficiency of the proposed model, simulations are fast and provide results which are in line with published experimental studies. Furthermore, the simulation tool may be useful for practical applications in physiological and medical studies, by evaluating the possible consequences of pathological conditions.

Sommario

L'ultimo decennio ha visto un crescente interesse nella modellistica biomatematica e nel calcolo scientifico, che ha portato a nuove applicazioni a rilevanti fenomeni fisiologici e ad una migliore comprensione dell'origine di varie malattie. Un argomento di grande interesse per diversi disturbi degenerativi è la filtrazione attraverso le pareti dei microvasi. Il ruolo della parete microvascolare è infatti di effettuare gli scambi gassosi e di nutrienti tra il sangue e l'interstizio, ed infine le cellule dei tessuti circostanti, bloccando le macromolecole. La comprensione di questi processi è importante per prevenire e curare le malattie neuro-degenerative, nonché per esplorare i possibili meccanismi per una somministrazione più efficiente di farmaci. Questo lavoro presenta un modello matematico unidimensionale e transitorio che descrive il trasporto di plasma sanguigno e di macromolecole attraverso le pareti dei vasi sanguigni. Il modello tiene conto della composizione eterogenea della parete microvascolare per descrivere accuratamente i flussi trasvascolari. Ciò si traduce in un modello multi-strato con proprietà fisiche che variano tra i vari strati della parete microvascolare. In particolare, il glicocalice ed l'endotelio, riscontrati in molti studi biologici, sono rappresentati nel nostro modello. Questa descrizione micro-strutturale, seppure semplificata, dei microvasi sanguigni consente di simulare l'effetto del danneggiamento del glicocalice e di altre patologie, quali ipertensione, emorragia ed ipovolemia, sia nel caso stazionario che transitorio. Grazie alla semplicità, e quindi all'efficienza, del modello proposto, le simulazioni risultano piuttosto rapide e forniscono risultati conformi a studi sperimentali pubblicati. Inoltre, possono inoltre costituire un valido aiuto per le applicazioni pratiche in studi fisiologici e medici, valutando le possibili conseguenze di varie condizioni patologiche.

Contents

Introduction	xxi
1 Micro-vascular exchange	1
1.1 Circulatory system	1
1.2 Trans-vascular pathways	1
1.3 Anatomy of a typical vessel wall	2
1.3.1 Glycocalyx	2
1.3.2 Endothelium	3
1.3.3 Blood-Brain Barrier	4
1.3.4 Modelling a microvessel	5
1.4 Capillarity Permeability	5
1.4.1 The permeability coefficients	5
1.4.2 Modelling the material properties	6
2 A preliminary decoupled model	9
2.1 Conceptual model	10
2.2 Analysis	11
2.2.1 Steady-state solutions for a single-layered vessel wall	11
2.2.2 Steady-state solutions for a vessel wall composed by two layers	13
2.2.3 The travel time through the vessel wall	17
2.3 Preliminary results	17
2.4 Conclusions	19
3 A coupled steady-state model	21
3.1 The mathematical model	22
3.1.1 Statement of the problem	22
3.1.2 Governing equations	22
3.1.3 Dimensionless flow and transport equations	24
3.1.4 Discharge and flux reconstruction	25
3.1.5 Analytical solution of the single- and two-layered model	26
3.1.6 Approximate analytical solutions for a single-layered microvessel	30

3.1.7	Parameters of two-layered model	31
3.2	Numerical approximation	32
3.2.1	Description of numerical schemes	32
3.2.2	Assessment of the computational methods	33
3.3	Results	37
3.3.1	Validation of the numerical scheme	37
3.3.2	Comparison between the two- and single-layered models	37
3.4	Conclusions	44
4	Glycocalyx damage and hypertension	47
4.1	The mathematical model	49
4.2	Relations between the physiological parameters	50
4.2.1	Physiological parameters across the wall	53
4.3	Simulation of glycocalyx shedding	53
4.3.1	How to simulate glycocalyx modulation?	53
4.3.2	Fluxes in the case of glycocalyx damage	56
4.4	Pressure influence on glycocalyx degeneration	58
4.5	Conclusions	60
5	A time-dependent model	63
5.1	The mathematical model	65
5.1.1	Statement of the problem	65
5.1.2	Governing equations in dimensionless form	67
5.1.3	Flux reconstruction	69
5.1.4	Physiological parameters	69
5.1.5	Linearised problem	70
5.1.6	Numerical methods	73
5.2	Validation of the model	74
5.2.1	Steady state	74
5.2.2	Time-dependent model	76
5.3	An application: study of an hemorrhage	77
5.3.1	Initial/boundary conditions in dimensionless form	77
5.3.2	How to model external pressures	79
5.3.3	Comparison between the single- and two-layered models	82
5.4	Conclusions	85
6	Conclusions and further work	87
	List of quantities and their dimension	93
	Bibliography	95
	Index	105

List of Figures

1	Schematic of a capillary, whose wall is composed by folded endothelial cells with glycocalyx coating their luminal side.	xxii
2	Sketch of the domain: a long hollow circular cylinder composed by two homogeneous porous membranes representing glycocalyx for $r \in (r_c, r_g)$ and endothelial cells for $r \in (r_g, r_o)$	xxiii
1.1	Illustration of the glycocalyx layer in a typical microvessel, with the range of dimensions of the most relevant anatomical elements (transverse view).	2
1.2	Illustration of an inter-cellular cleft in the endothelium of a typical microvessel, with some protein complexes either providing anchorage and cell stability (adherens junctions) or forming an almost impermeable barrier to fluid and macromolecules (tight/occludens junctions).	3
1.3	Schematic of a capillary, whose wall is composed by folded endothelial cells with the glycocalyx coated at their luminal side.	4
1.4	Sketch of the domain: a long hollow circular cylinder composed by two homogeneous porous membranes representing glycocalyx for $r \in (r_c, r_g)$ and endothelial cells for $r \in (r_g, r_o)$	5
2.1	(a) The domain is an infinitely long hollow cylinder composed by one layer only, whose inner and outer radii are r_c and r_o . (b) Cross section depicting boundary conditions, where $P_c = p_c - \sigma\Pi_c$ and c_c refer to net blood pressure and solute blood concentration, respectively and $P_o = p_o - \sigma\Pi_o$ and c_o indicate blood pressure and solute concentration in the interstitial fluid.	12
2.2	(a) The domain is an infinitely long hollow cylinder composed by two layers (r_c, r_g) and (r_g, r_o) . (b) Cross section depicting boundary conditions, where $P_c = p_c - \sigma_1\Pi_c$ and c_c refer to net blood pressure and solute blood concentration, respectively and $P_o = p_o - \sigma_2\Pi_o$ and c_o indicate blood pressure and solute concentration in the interstitial fluid.	14

2.3	Discharge per unit length depending on internal hydrostatic pressure, in the arteriolar (dashed line) and in the venular case (solid line). The bullets represent the typical values of internal blood pressure in both cases.	19
2.4	Travel time of a molecule of serum albumin, in arterioles (dashed curve) and in venules (solid curve). The bullets represent the typical values of internal blood pressure in both cases.	20
3.1	Sketch of the domain: a long hollow circular cylinder composed by two homogeneous porous membranes representing glycocalyx for $r \in (r_c, r_g)$ and endothelial cells for $r \in (r_g, r_o)$	22
3.2	Sketch of the domain indicating the relevant geometric elements: the internal radius r_c at luminal side of micro-vessel, the radius of the interface between glycocalyx and endothelial cells, r_g , and the external radius r_o . In addition, p_c and Π_c are hydrostatic and osmotic pressures, respectively, within the lumen, while p_o and Π_o are the same quantities in the external interstitial space.	24
3.3	L_2 -norm $\Delta_k = \ (\Pi, p)_k - (\Pi, p)_{k-1}\ _2$ as function of grid points, for Freeze's finite difference method and Runge-Kutta shooting methods of orders 1 to 4.	34
3.4	Error $E_k = \ (\Pi, p)_k - (\hat{\Pi}, \hat{p})\ _2$ as function of grid points, for Freeze's finite difference method and Runge-Kutta shooting methods of orders 1 to 4.	35
3.5	Error $E_k = \ (\Pi, p)_k - (\hat{\Pi}, \hat{p})\ _2$ as function of CPU time, for Freeze's finite difference method and Runge-Kutta shooting methods of orders 1 to 4.	36
3.6	Relative differences between numerical and analytical solutions of volumetric and solute mass fluxes, as a function of the number of grid points.	38
3.7	Comparison between the numerical solution of osmotic (a) and hydrostatic (b) pressures for the two-layered case, obtained with the Freeze's scheme by using 18433 grid nodes (Numerical, 2-L), and the corresponding analytical solutions (Analytical, 2-L). The single layer analytical solutions (Analytical, 1-L) are also shown together with the linearised analytical solutions (Linearised, 1-L) presented in Section 3.1.6. In all cases $\varepsilon^2 = 0$ and for ease of representation the numerical solution is shown only at a few grid points. The properties of the two layers are reported in Table 3.1 together with Dirichlet boundary conditions at the lumen and interstitial sides of micro-vessel wall.	39

3.8	Osmotic (a) and hydrostatic (b) pressures across micro-vessel wall for $\varepsilon^2 = 0, 10^{-4}, 10^{-3}$. The case $\varepsilon = 0$ is obtained by means of the analytical solutions, while the cases with $\varepsilon^2 = 10^{-4}, 10^{-3}$ are obtained numerically with Freeze's scheme by using 18433 grid nodes.	41
3.9	Behaviour of osmotic and hydrostatic pressures across micro-vessel wall for several values of the osmotic pressure Π_c in the lumen.	42
3.10	Volumetric and solute mass fluxes, relative to the reference case with boundary conditions and material properties as shown in Table 3.1, as a function of blood osmotic pressure Π_c within the lumen.	42
3.11	Behaviour of osmotic (a) and hydrostatic (b) pressures across micro-vessel wall for several values of blood hydrostatic pressure p_c within the lumen.	43
3.12	Volumetric and solute mass fluxes, with boundary conditions and material properties as shown in Table 3.1, as a function of the blood hydrostatic pressure p_c within the lumen.	44
4.1	Diffusional permeability ℓ_d versus ℓ_p and σ . Here the physiological parameters ℓ_p and ℓ_d are dimensionless with respect to the weighted harmonic mean ℓ_p^H for the hydraulic conductivity.	52
4.2	Contour lines of physiological parameters σ , ℓ_p and ℓ_d (divided by the reference value obtained for an integer vessel wall) varying with respect to pore radius r_p and the number N of pores in glycocalyx layer (divided by the corresponding values of an integer glycocalyx).	55
4.3	Contour lines of volume and solute fluxes (divided by reference fluxes) as functions of glycocalyx thickness ℓ_G , pore radius r_p and number of pores N (divided by the corresponding values of an integer glycocalyx).	57
4.4	Contour lines of volume and solute fluxes (divided by reference fluxes) as functions of hydrostatic blood pressure p_c (normalised by its typical value in a microvessel of a normotensive control) and morphological and/or physical parameters ℓ_G , r_p and N (normalised by the corresponding values of an integer glycocalyx).	59
5.1	Illustration of an inter-cellular cleft between endothelial cells in a typical microvessel, with some protein complexes either providing anchorage and cell stability (adherens junctions) or forming an almost impermeable barrier to fluid and macromolecules (tight/occludens junctions).	66

- 5.2 Illustration of glycocalyx in a typical microvessel, with the range of dimensions of the most relevant anatomical elements (transverse view). 66
- 5.3 Sketch of our static mathematical domain: an infinitely-long hollow circular cylinder composed by two homogeneous uniform porous membranes representing glycocalyx for $r \in (r_c, r_g)$ and endothelial cells for $r \in (r_g, r_o)$ 67
- 5.4 Hydrostatic (a) and osmotic (b) pressures for the two-layered model at given times $t \in \{0, 1.02 \cdot 10^{-6}, 1.02 \cdot 10^{-4}, 1.02 \cdot 10^{-2}, 1.02 \cdot 10^{-1}\}$, obtained numerically with a spatial grid of 100 points, $\Delta t = 10^{-6} \cdot (\Delta x)^2$, $\varepsilon = 0$ and tolerance equal to 10^{-9} (thin curves/marks), and compared to the analytical steady-state solutions (thick curves) described in Chapter 3. 75
- 5.5 L_2 -norm of the difference between the transient numerical solution (obtained numerically with a spatial grid of 100 points, $\Delta t = 10^{-6} \cdot (\Delta x)^2$ and $\varepsilon = 0$) and the steady-state analytical solution for the two-layered model of both osmotic (dashed curve) and hydrostatic pressure (solid curve). 75
- 5.6 Hydrostatic (a) and osmotic (b) pressures of the modified problem for the two-layered model after one period ($t = 1$), obtained numerically with a spatial grid of 49 points, $\Delta t = (\Delta x)^2 = 4.3403 \cdot 10^{-4}$ and $\varepsilon = 10^{-2}$ (circles), and compared to exact solutions (solid curves). 76
- 5.7 Behaviour of the boundary conditions, both for constant external pressures (a) as described in equations (5.34)-(5.37) and for pressures varying with time (b) and following equations (5.34)-(5.36). 79
- 5.8 Behaviour of the mean volume (a)-(c) and solute (b)-(d) fluxes, reconstructed from both the complete non-linear system (a)-(b) and from the linearised problem described in Section 5.1.5 (c)-(d). The numerical solutions for the pressures were computed using a spatial grid of 100 points and $\Delta t = (\Delta x)^2$. The external pressures are assumed either constant as in equations (5.36) (solid curves) or varying with time following equations (5.37) (dashed curves). 80

5.9 Comparison of the mean volume (a) and solute (b) fluxes, reconstructed from the full non-linear system (solid curves) and from the linearised problem described in Section 5.1.5 (dashed curves), for external pressures varying following equations (5.37). The numerical solutions for the pressures were computed using a spatial grid of 100 points and $\Delta t = (\Delta x)^2$. The fluxes obtained considering the two-layered model are depicted with thick curves, while the ones of the single-layered model are depicted with thin curves. The equivalent dimensionless parameters are assumed equal to $\sigma^{eq} = 0.7987$, $\ell_p^{eq} = 0.8247$ and $\ell_d^{eq} = 0.5838$ 83

5.10 Hydrostatic (a) and osmotic (b) pressures obtained numerically with a spatial grid of 100 points and $\Delta t = (\Delta x)^2$ for the two-layered model, for external pressures varying following equations (5.37). 84

5.11 Hydrostatic (a) and osmotic (b) pressures obtained numerically with a spatial grid of 100 points and $\Delta t = (\Delta x)^2$ for the single-layered model, for external pressures varying following equations (5.37). The equivalent dimensionless parameters are assumed equal to $\sigma^{eq} = 0.7987$, $\ell_p^{eq} = 0.8247$ and $\ell_d^{eq} = 0.5838$ 84

List of Tables

2.1	Typical values of the parameters used in the computation. K is the hydraulic conductivity for serum albumin, σ is the reflection coefficient for serum albumin, n is the porosity, r is the mean radius of the vessel and Δx is the vessel thickness. A refers to the arteriolar end of capillary bed, while V to the venous end.	17
2.2	Mean pressures in human body, taken from Boron and Boulpaep (2005). p represents hydrostatic pressure, while Π is osmotic pressure and σ is the reflection coefficient. The subscript c refers to the pressure measured inside the vessel, while the subscript o is measured just outside the vessel. ΔP is defined as the difference of the net pressure P between the internal and the external side of microvessels, i.e. $\Delta P = P_c - P_o = (p_c - \sigma\Pi_c) - (p_o - \sigma\Pi_o)$	18
3.1	Typical values of material properties of a micro-vessel: σ is the reflection coefficient, ℓ_p is the hydraulic conductivity, ℓ_d is the diffusional permeability. The coefficient α depends on a Péclet number and is defined such as to respect condition (3.46). The superscripts G and W indicate glycocalyx and endothelial layers, respectively.	31
3.2	Volumetric and solute mass fluxes for the following values of ε^2 , the parameter controlling the smoothness of properties transition between the two layers: $\varepsilon^2 = 0, 10^{-4}, 10^{-3}$	41

4.1	Typical values of material properties of a capillary: σ is the reflection coefficient and ℓ_p is the hydraulic conductivity. The typical values of capillary blood hydrostatic and osmotic pressures (p_c and Π_c) are reported against typical values of interstitial pressures p_o and Π_o . The superscripts G and W refer to glycocalyx and endothelial layers, respectively. μ is kinematic water viscosity, r_s is the mean molecular radius of human serum albumin and D_{free} is its free diffusion coefficient. The coefficient $\alpha > 1$ depends on a Péclet number and is defined such as to satisfy condition (4.10).	54
5.1	Typical values of material properties of a capillary: σ is the reflection coefficient, ℓ_p is the hydraulic conductivity, ℓ_d is the diffusional permeability. Superscripts G and W refer to glycocalyx and endothelial layers, respectively. As described in Section 5.3.1, boundary conditions change following equations (5.34)-(5.36)-(5.37) with initial (at $t = 0$) and final (at $t = T$) values denoted with superscripts 0 and T , respectively. The coefficient β_w refers to the compressibility of horse blood plasma, while β_m is the maximum value of blood vessel wall compressibility measured in dog descending thoracic aorta. The porosity n was measured in an arterial graft prosthesis. .	70
5.2	L_p -norm errors of the numerical solutions obtained with different meshes at time $t = 1$, for the two-layered model and $\varepsilon = 10^{-2}$	77
5.3	Empirical orders of accuracy computed from the different L_p -norm errors reported in Table 5.2 at time $t = 1$ for the two-layered model and $\varepsilon = 10^{-2}$	77
5.4	Mean volume and solute fluxes for certain times, both for the complete non-linear system and for the linearised problem described in Section 5.1.5. The numerical solutions for the pressures were computed using a spatial grid of 100 points and $\Delta t = (\Delta x)^2$. The external pressures are assumed either constant as in equations (5.36) or varying with time (transient BCs) following equations (5.37). The values of the fluxes are reported both for the two-layered model and for the single-layered model with equivalent dimensionless parameters equal to $\sigma^{eq} = 0.7987$, $\ell_p^{eq} = 0.8247$ and $\ell_d^{eq} = 0.5838$, following the procedure described in Chapter 3.	81
1	Notation and dimensions of the quantities. L is the length, T is the time, M is the mass, Θ is the temperature and N is the number of moles.	93

Acknowledgements

I would like to express my sincere gratitude to the following individuals:

- my supervisors, prof. Bellin and prof. Toro, for their direction, enthusiasm and understanding, always providing me with new suggestions and ideas;
- prof. Zanolli, for her precious advise and for her help;
- my office mates, Gino I. Montecinos and Lucas O. Müller, for their invaluable help and constant support;
- my family, for their constant encouragement and trust; thank you all, Luciano, Gabriella, Silvia, Graziosa, Ferruccio, Zelia and Giovanni; you are always in my heart;
- my betrothed Simone, for his patience and listening;
- Flavia, for always being a true friend;
- my colleagues, for their friendship;
- all friends all around the world.

This work was supported by MIUR (Italy) and CARITRO (*Fondazione Cassa di Risparmio di Trento e Rovereto*, Italy).

The Life (of the flesh) is in the Blood

Lev. 17:10-12

*To my family
who has always encouraged me and taught me to believe I could do anything;
to Simone
who helped me to do even the things I never thought I could do;
to all those
who have always supported me with affection in my every choice;
to all those
who helped me along the way;
to all those I love*

Introduction

Trans-vascular flow occurring in small and large vessels plays a decisive role in human physiology by ensuring an endless flow of oxygen and other electrolytes needed to sustain cell metabolism. Altogether, vessel wall operates as a semipermeable membrane, which is selective with respect to the size of molecules, such that water and electrolytes pass through the wall much more easily than proteins. In order to preserve volume homeostasis, the following question should be addressed: how does the interstitium avoid accumulating plasma ultrafiltrate? The traditional view, by now disproved, is that small veins and venules continuously re-absorb interstitial fluid, but this seems no longer true. As a matter of fact, the *lymphatic system*, in addition to its known role in the immuno-surveillance, has the vital task of draining back into the venous part of the circulatory system the fluid filtrated from micro-circulation, the *interstitial fluid* having a substantially reduced protein content, through a complex network of lymphatic vessels (e.g. Levick, 2010; Silverthorn, 2009).

As evidenced by Starling (1896), volumetric flow through microvessel wall is controlled by the net imbalance between the *osmotic pressure* of plasma proteins and the capillary *hydrostatic pressure* generated by heart beat. Both pressures can change to exert a regulatory action on filtration, such as for example during exercise when an increased filtration is triggered by a larger capillary pressure and plasma volume reduces by up 20%. On the other hand, an increased filtration occurs during cardiac failure, which causes excess water accumulation in the tissues (*oedema*). Substantial movement of fluids occurs during rapid swelling of acutely inflamed tissues, while a rapid absorption of interstitial fluid into blood stream follows an acute *hemorrhage*.

Electron micrograph studies (Turner et al., 1983) show that a typical extra-cranial capillary is composed by only two layers: the glycocalyx and the endothelium, as depicted in Figure 1.

Explicit modelling of the effect on glycocalyx and clefts at junctions between endothelial cells has been performed by solving the Navier-Stokes (NS) equations at micro scale (see e.g. Sugihara-Seki and Fu, 2005; Sugihara-Seki et al., 2008). The main drawback of this modelling approach, besides high computational burden, lies in the difficulty to model the interaction between macromolecules and fibre cells composing glycocalyx, which feeds

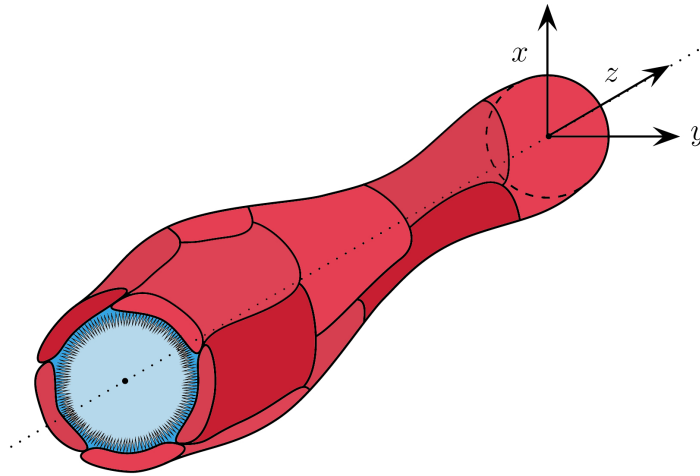


Figure 1: Schematic of a capillary, whose wall is composed by folded endothelial cells with glycocalyx coating their luminal side.

back to volumetric flow through the osmotic pressure (Squire et al., 2001; Weinbaum et al., 2003). To overcome this difficulty, hybrid methods have been used in which the glycocalyx has been modelled as a membrane (porous medium), while the flow through clefts has been modelled by solving the NS equations (Sugihara-Seki et al., 2008). A similar approach has been used by Prosi et al. (2005) and Formaggia et al. (2009) to model mass transfer across arterial walls in patients affected by atherosclerosis.

The glycocalyx layer, or even the whole vessel wall, is often lumped into an interface and considered as a membrane through the non-linear algebraic Kedem-Katchalsky equations (Kedem and Katchalsky, 1958). In this way, pressure distribution inside the membrane is completely neglected and the dilution at the interface between glycocalyx and endothelium, described for instance in Adamson et al. (2004), can not be reproduced.

A further simplified, yet effective, way to represent vessel wall is by the superimposition of two membranes with different properties. The external membrane mimics the effect of the mono-layered of endothelial cells joined edge to edge along segments forming an irregular pattern of connections, in a crazy-paving resemblance, without representing explicitly the structure of the clefts. The connections are partially closed by tight junctions. On the other hand, the internal membrane represents the glycocalyx coating the layer of endothelial cells (Levick, 2010). Considering that the single layer of endothelial cells is folded to form an annular semipermeable barrier around blood stream, the trans-capillary flow can be assumed as mainly radial and orthogonal to blood flow direction z (Figure 2).

This simplified computational domain, with the internal membrane representing the glycocalyx and the external one the endothelium, agrees with

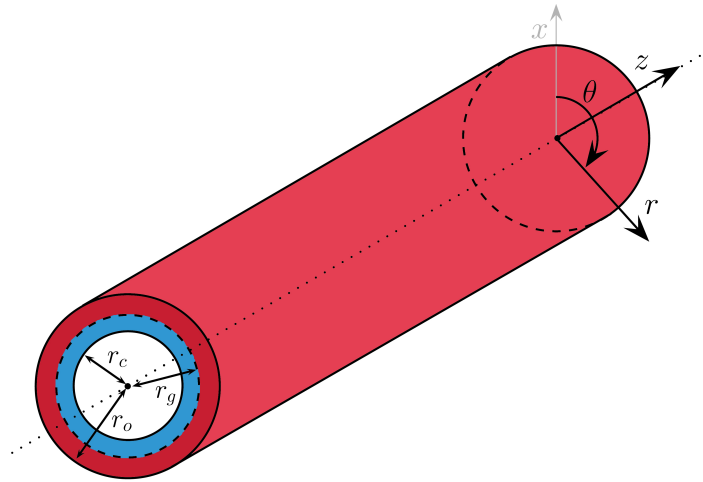


Figure 2: Sketch of the domain: a long hollow circular cylinder composed by two homogeneous porous membranes representing glycocalyx for $r \in (r_c, r_g)$ and endothelial cells for $r \in (r_g, r_o)$.

morphometric measurements (see e.g. Hu et al., 2000; Adamson et al., 2004; Levick, 2010), but differs from existing studies in the way the main structural elements are combined, as previously described. Khakpour and Vafai (2008b; 2008a; 2008d) and Ai and Vafai (2006) decouple the flow equation from the transport equation and in Khakpour and Vafai (2008c) some models with coupled filtration and transport equations are reviewed, but the coupling is algebraic and not differential, as in our model.

The purpose of this thesis is to model filtration and transport phenomena in living tissue, also simulating pathological conditions as hypertension, glycocalyx damage, hemorrhage. . . In order to take into account the link between filtration and solute transport, a time-dependent one-dimensional multi-layered mathematical model described by a parabolic system was built. The equations are written in cylindrical coordinates, to take advantage of the radial symmetry of vessels. An analytic solution of the coupled flow and transport equations in steady-state is presented in the case of the two-layered membrane with discontinuous physiological parameters. Also the case of a smooth variation of media, and thus of the physical parameters, is explored using numerical solutions.

The time-dependent filtration and solute transport processes are investigated both in the case of constant extra-vascular pressures, thus neglecting the plasma/interstitial fluid balance, and in the case of a transient change in the external pressures, due to the transient absorption of interstitial fluid into the lumen which increases plasma protein content in the interstitium and lowers the pressure exerted outside the vessel wall (Levick, 2010; Levick and Michel, 2010).

The outline of this dissertation is as follow.

Chapter 1 provide an overview of the physiology of the micro-vascular exchange system, also recalling main anatomic features of blood microvessels. We also justify simplifications both in the domain and in the radial flows. The permeability coefficients used to model vessel wall are presented and their distribution across the vessel is described.

In *Chapter 2* we present a preliminary study in which we focus on the increase in hydrostatic pressure, therefore neglecting the coupling of flow and transport equations. This simplification permits to solve the flow and transport equations separately and to analyse the typical travel time, namely an approximation of the time needed to a single solute molecule to cross vessel wall.

In *Chapter 3* we present the steady-state one-dimensional multi-layered model used to describe the physiological processes controlling coupled filtration and macro-molecules transport across vessel wall, resulting from the application of general physical and thermodynamic principles. This is a generalisation of the equations presented in Chapter 2, being valid also for low pressures. In the case of a composite vessel wall, comprising two membranes with discontinuous physical properties (and thus physiological parameters), the analytical solution of the coupled flow and transport equations, with the latter being non linear, is reported. Also the case of smooth transition is explored by using a suitable numerical scheme and the results of our model are compared with others taken from the literature. The results of our simulations are discussed, emphasising the combined effect of glycocalyx and endothelial cells on controlling volumetric flow and solute mass transport across microvessel wall. The dilution occurring in the cleft at the contact with the external surface of the glycocalyx (Michel, 1997; Weinbaum, 1998) is reproduced by the model, in contrast to homogeneous single-layered models.

In *Chapter 4* we apply the steady-state model presented in Chapter 3 to investigate the effects on exchange of fluid and macromolecules across a typical microvessel wall, both in the case of glycocalyx deterioration, either due to enzymatic digestion or to agonist recruitment, and in hypertensive zones such as pre- and post-stenotic blood vessels. The change in the physiological parameters needed to simulate glycocalyx deterioration is described, paying attention to the relations among them. What emerges is that a seriously damaged glycocalyx produces an augmentation of flux of both solvent and solute, thus losing its role of transport barrier and macro-molecular sieve, as observed in the experiments of van den Berg et al. (2003). Analogously, the effects of capillary pressure increase, as in the case of hypertension, on both fluxes is investigated, showing an augmentation of both volume and solute fluxes, in agreement with experimental results. The conjunction of glycocalyx degradation and hypertension further raises plasma and solute fluxes, leading in most severe cases to oedema and hemorrhage, as in the case of diabetes.

In *Chapter 5* we present the governing equations of our time-dependent mathematical model with two different sets of external pressures, one constant and the other taking into account the change in interstitial pressure due to transient absorption of plasma and proteins. We solve them using a finite-difference Crank-Nicolson numerical scheme, validating our model first through a test in which, imposing constant boundary conditions, we reach the steady-state analytical solutions in a finite time and then testing also the time-dependent nature of the model. We then apply our model to study the case of sudden capillary pressure drop, as during hemorrhage, confirming that, under normal conditions of internal pressures, the initial absorption of interstitial fluid due to pressure drop is followed by a gradual increase in both volume and solute flux until a steady state of slight filtration and solute leak is attained, as described by Levick and Michel (2010).

Finally, *Chapter 6* summarises the achievements of the dissertation, also suggesting some additional studies.

Chapter 1

Micro-vascular exchange

In this section we summarise anatomic features of mammalian blood vessels useful to describe the geometry of the computational domain used in the present work.

1.1 Circulatory system

The circulatory system is composed by vessels of size ranging from centimetres in the main ones to a few microns in capillary bed. The structure of vessel wall differs between arteries and veins and also between large vessels and capillaries. Each segment of circulation shows an optimal combination of size, wall composition, thickness and cross-sectional area that best fulfils its function. For example, arteries are more muscular than veins because they have to bear the pumping force of heart.

Large vessels are formed of three layers: the *endothelium*, the *middle layer* (composed by smooth muscle cells) and the *connective layer*. On the contrary, small vessels such as capillaries, venules and arterioles are only one-cell thick, in order to optimise the exchange of small hydrophilic molecules from blood stream to interstitial volume before crossing cell membrane.

1.2 Trans-vascular pathways

There are different pathways across which protein and plasma can be transported (Levick, 2010). Not only a system of small pores allows the passage of nutrients and gases. Four primary pathways for passive transport of plasma components have been hypothesised: *inter-cellular cleft*, *trans-cellular pores*, *vesicles* and *fenestrae* (Sugihara-Seki and Fu, 2005), even if a long-standing controversy over the effective existence of vesicular transport and transcytosis exists (Michel, 1996).

It should also be noted that these possible pathways also depend on the capillaries we are considering. As a matter of fact, in microvessels with

continuous endothelium, the principal pathway for water and solutes lies between endothelial cells (see Figure 1.2) through inter-endothelial clefts (Sugihara-Seki and Fu, 2005). Particular attention should be given to the tight blood-brain barrier, across which specific endothelial carriers transport solute to protect neurons from neurotoxic agents and to prevent pathological conditions such as cerebral hemorrhage, inflammation and oedema (Levick, 2010).

1.3 Anatomy of a typical vessel wall

The structure of the vessels is very specialized in relation to their functionality and this specialization results in different permeability and reflection coefficients of vessel wall.

1.3.1 Glycocalyx

Microvessel wall is typically composed of a single layer of endothelial cells, which are internally coated with a 150 – 400 nm thick dynamic negatively-charged hydrated gel, called *glycocalyx*, as depicted in Figure 1.1. The glycocalyx, present chiefly in capillaries since their endothelial surface area accounts for most of the total surface area of the vascular system (VanTeeffelen et al., 2007), extends into outer regions of inter-cellular clefts between endothelial cells composing blood vessel wall (Sugihara-Seki and Fu, 2005) and protrudes into the lumen in hairy tufts, forming a size- and charge-selective molecular sieve to plasma proteins, while being permeable to water and small solutes, including oxygen and other nutrients (Levick, 2010, Ch. 9). The fibre matrix of the glycocalyx was described by Squire et al. (2001) as a quasi-periodic 3D fibrous mesh work with a characteristic spacing of 20 nm and with anchoring foci (thought to form an hexagonal array) emanating from the underlying cortical cytoskeleton, as depicted in Figure 1.1. See also Figure 5 of Arkill et al. (2012), in which the glycocalyx structure is reconstructed using electron tomography.

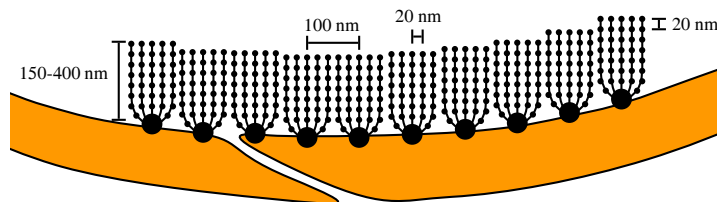


Figure 1.1: Illustration of the glycocalyx layer in a typical microvessel, with the range of dimensions of the most relevant anatomical elements (transverse view).

Often, the role of glycocalyx is ignored, even if it was first introduced in 1963 by Bennett (1963) and is currently recognised as crucial for micro-vascular wall homeostasis, in particular it acts (a) as a transport barrier, regulating micro-vascular perfusion and exchange, (b) as a molecular sieve, maintaining low permeability to macromolecules, (c) as a porous hydrodynamic interface in blood cell motion in microvessels, (d) as a hydrodynamic exclusion layer, inhibiting the adhesion of red blood cells to endothelial cell membrane proteins and modulating leukocyte attachment and rolling and (e) as a transducer of mechanical forces (fluid shearing stresses) to the intracellular actin cortical cytoskeleton of the endothelial cell in the initiation of intracellular signalling and mediation of shear stress-dependent nitric oxide (*NO*) production (e.g. VanTeeffelen et al., 2007; Weinbaum et al., 2003).

1.3.2 Endothelium

Capillary wall is composed by a one-cell-thick layer of *endothelial cells*, separated by inter-cellular clefts. These long slits can be partially sealed by dynamic complexes of cell-cell junctional proteins, as depicted in Figure 1.2, thereby increasing the selectivity of the whole membrane.

They provide anchorage and cell stability, as in the case of the *adherens junctions*, or form an almost impermeable barrier to plasma and macromolecules (*tight/occludens junctions*), in particular in the continuous capillaries composing the *blood-brain barrier* (Levick, 2010; Hawkins and Davis, 2005).

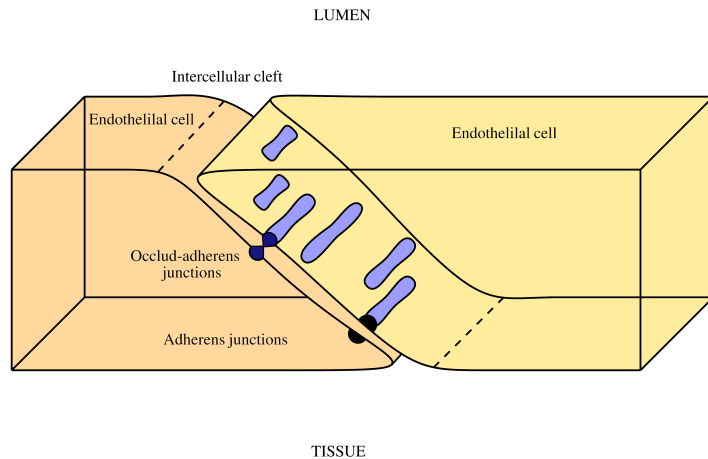


Figure 1.2: Illustration of an inter-cellular cleft in the endothelium of a typical microvessel, with some protein complexes either providing anchorage and cell stability (adherens junctions) or forming an almost impermeable barrier to fluid and macromolecules (tight/occludens junctions).

1.3.3 Blood-Brain Barrier

In fact, the clefts of cerebral capillaries are closed by multiple junctional strands with no gaps, to impede neurotoxic agents contained in blood stream to reach the interstitial fluid, further reducing the permeability to macromolecules. Since nourishment of neurons and glucose supply provided by cerebral capillaries are strongly coupled, a complex structure, called *neuro-vascular unit* exists.

This is composed by some peculiar cerebral cells (Hawkins and Davis, 2005; Li et al., 2010), among which are the *pericytes*, irregularly attached to the abluminal membrane of the endothelium and able to differentiate into various types of cells (in particular during angiogenesis) and responsible to blood-brain barrier stability and blood flow regulation. They are sheathed by the *basement membrane*, a mechanical barrier responsible of cell anchorage and essential for angiogenesis. Outside the basement membrane are attached also the *astrocytes* (part of the neuro-vascular unit), giving biochemical support, providing nutrients to the blood-brain barrier and responsible of the regulation of extracellular ion balance and processes of repair and scarring (Hawkins and Davis, 2005; Li et al., 2010).

The *breakdown of the blood-brain barrier* with the associated increase of vessel permeability has been observed in many brain diseases. Examples include stroke, traumatic head injury, Alzheimer's disease, AIDS, brain cancer, meningitis etc. (see Li et al., 2010). In addition, blood-brain barrier rupture has been associated with multiple sclerosis, as discussed for instance by Zamboni et al. (2009), Singh and Zamboni (2009) and Haacke et al. (2005).

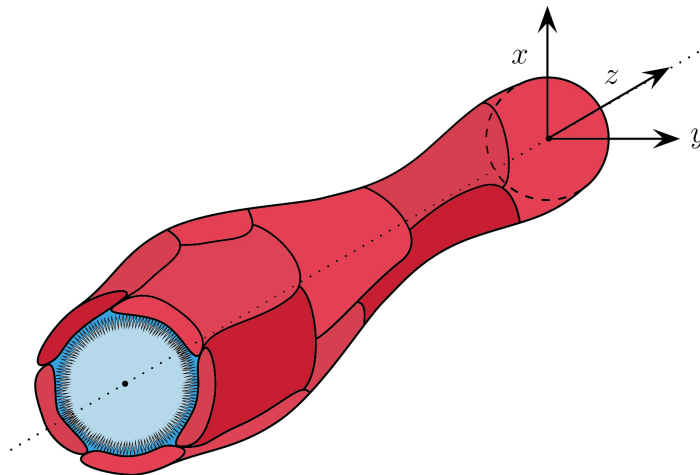


Figure 1.3: Schematic of a capillary, whose wall is composed by folded endothelial cells with the glycocalyx coated at their luminal side.

1.3.4 Modelling a microvessel

We are interested in a typical extra-cranial capillary, composed by only two layers: the glycocalyx and the endothelium, as depicted in Figure 1.3.

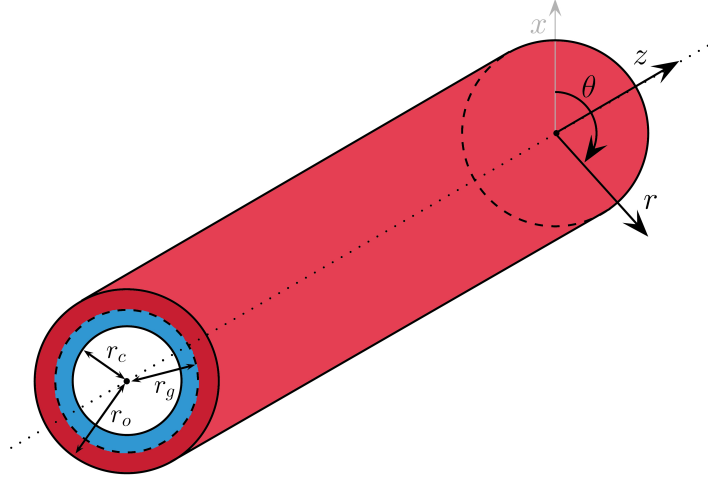


Figure 1.4: Sketch of the domain: a long hollow circular cylinder composed by two homogeneous porous membranes representing glycocalyx for $r \in (r_c, r_g)$ and endothelial cells for $r \in (r_g, r_o)$.

To verify this conceptual model, and avoid complex micro-scale modelling in view of applications at a larger scale, we propose to represent vessel wall as the superimposition of two membranes with different properties, as shown in Figure 1.4. The internal membrane represents glycocalyx, while the external membrane is introduced to mimic the effect of endothelial cells.

1.4 Capillarity Permeability

1.4.1 The permeability coefficients

The *permeability coefficients* describe capillary permeability and are defined for instance in Michel and Curry (1999). Here we recall their definitions.

The *hydraulic permeability* L_p (also called *hydraulic conductivity* or *hydraulic conductance* or *filtration coefficient*) is defined as the flow of fluid per unit area of capillary wall J_v per unit difference in hydrostatic pressure Δp across the wall, under conditions when the difference in osmotic pressure within the capillary lumen and immediately outside the vessel is zero, i.e. when $\Delta\Pi = 0$:

$$L_p := \frac{J_v}{\Delta p}. \quad (1.1)$$

The *diffusional permeability coefficient* P_d is defined as the mass transport of a substance per unit area J_s per unit concentration difference Δc ,

under conditions when the fluid flow through the capillary wall is zero, i.e. when $J_v = 0$:

$$P_d := \frac{J_s}{\Delta c}, \quad (1.2)$$

The *reflection coefficient* σ compares the penetration of a solute with that of the solvent through a membrane. It can be defined either as the fraction of solute “reflected” at the membrane during ultrafiltration in the absence of a concentration difference, i.e. when $\Delta c = 0$:

$$\sigma_f := 1 - \frac{J_s}{J_v \cdot C}, \quad (1.3)$$

or as that fraction of its total osmotic pressure which the solute can exert across the membrane, i.e. when $J_v = 0$:

$$\sigma_d := \frac{\Delta p}{\Delta \Pi}. \quad (1.4)$$

The equivalence of these definitions only applies to ideal solutions, i.e. to solutions in which the activity coefficients (which measure deviation from ideality) are equal to one.

If we have a membrane with cylindrical pores of uniform dimensions we can estimate some of these constants. If we assume that the pore radius r is many times greater than the radius of a water molecule, L_p is proportional to r^4 , P_d for small hydrophilic molecules (or water) is proportional to r^2 and σ for a neutral solute is proportional to a function of the ratio of solute radius to the pore radius.

In the following, apart from σ , we will consider some slightly different transport parameters, indicated with small italic letters (ℓ_p and ℓ_d), due to conversion of the formulation from algebraic relations to differential equations. The resultant relationships between the two sets of parameters can be stated as

$$\ell_p = L_P \cdot \Delta x, \quad (1.5)$$

$$\ell_d = \frac{P_D \cdot \Delta x}{\Pi_M}, \quad (1.6)$$

where Δx is the membrane thickness and Π_M is a mean value of the osmotic pressure.

1.4.2 Modelling the material properties

Molecules dissolved in water are driven through the vessel wall by the gradient of the net pressure P , which is given by the difference between the hydrostatic p and osmotic Π pressure: $P = p - \sigma\Pi$, where σ is the reflection coefficient. σ depends on the ratio between the Stokes radius of the molecule and the pore radius, or the size of the cleft between adjacent endothelial cells.

When the size of the molecule is comparable with the pore size (or the aperture), the vessel wall behaves as a perfect membrane and $\sigma \rightarrow 1$. On the other hand, when molecules are much smaller than pore size, the membrane effect vanishes and $\sigma \rightarrow 0$. In the latter case, transport across vessel wall is controlled by the gradient of hydrostatic pressure. For a given pore (or cleft) size, the role of osmotic pressure increases with molecule size. The sieving effect of glycocalyx on macromolecules is represented by a σ value that approaches 1, while in the stratum representing the endothelial cells σ is typically smaller, to reflect the larger aperture of the tight junctions connecting the two sides of the cleft at the border between adjacent cells (Levick, 2010).

For the analytical solution, we consider membrane properties as piecewise constant with a discontinuous (abrupt) change at $r = r_g$, the interface between glycocalyx and endothelial cells. This abrupt transition is convenient for obtaining the analytical solution, but not necessarily represents the real transition of the physical properties. As a possible alternative we consider the following model of smooth transition:

$$\begin{cases} \sigma(r) &= \frac{\sigma_G + \sigma_W}{2} + \frac{\sigma_G - \sigma_W}{2} w(r - r_g), \\ \ell_p(r) &= \frac{\ell_p^G + \ell_p^W}{2} + \frac{\ell_p^G - \ell_p^W}{2} w(r - r_g), \\ \ell_d(r) &= \frac{\ell_d^G + \ell_d^W}{2} + \frac{\ell_d^G - \ell_d^W}{2} w(r - r_g), \end{cases} \quad (1.7)$$

where $w = w(r)$ is the smoothing function defined as follows:

$$w(r) = \frac{r}{\sqrt{\varepsilon^2 + r^2}}, \quad (1.8)$$

where both sub- and super-scripts G and W indicate the properties of glycocalyx and the endothelial cells, respectively. With this function we can control how properties vary at the interface between the two layers, with a discontinuous transition occurring for $\varepsilon \rightarrow 0$. With $\varepsilon > 0$ the transition becomes progressively smoother to simulate possible gradual transitions, with different degrees of smoothness as indicated by Sugihara-Seki and Fu (2005).

Chapter 2

A preliminary decoupled model

The content of this Chapter is taken from Facchini et al. (2013c).

From a physiological point of view, microvessel wall plays an important role in maintaining equilibrium between intra- and extra-vascular fluid compartments. Under normal conditions, vessel walls are nearly impermeable to macromolecules, while lipophilic species and small hydrophilic substances are allowed to cross the wall and reach surrounding tissues. Fluid flow and transport of dissolved molecules across wall depend on permeability and diffusivity of the membrane composing the wall. Therefore, alterations of blood pressure may lead to impaired exchange processes and, in extreme cases, to leakage of hematic fluid. Several alterations of these exchange processes have been observed, mainly in compartments other than the brain, resulting in leakage of macromolecules, which is typically attributed to reduction of osmotic pressure, or inflammatory processes that alter endothelial structure.

In the present chapter we investigate the role of an increased blood pressure as the driving force for alteration of exchange processes and leakage of macromolecules. In particular, we analyse through a simplified, yet realistic, flow and transport model, the impact of alterations in hydrostatic blood pressure on transport of molecules across microvessel wall. Vascular wall is assumed to be composed of two layers with different permeability, as assumed in previous studies on fluid flow and macromolecules transport in heteroporous membranes. The inner layer represents glycocalyx, a membrane composed of extra-cellular polymeric material which is believed to exert an important sieving effect on macromolecules, while the external layer represents the combined effect of the endothelial cells.

With this model we obtain closed-form steady-state solutions for fluid flow and solute transport through microvessel walls, which can be used for a preliminary analysis of leakage of macromolecules due to an increase of blood pressure.

2.1 Conceptual model

Let us approximate microvessel geometry as a rigid circular cylinder, infinitely long in the z -direction, i.e. in the direction of blood stream. We assume vessel wall composed by one or more permeable layers of a given thickness. Physical properties, such as permeability and molecular diffusion are assumed constant within a layer, but may vary across the layers. The porosity is assumed the same in all layers. Molecules of a given Stokes radius are dissolved into blood plasma at a concentration that does not modify its density and viscosity. Furthermore, to simplify the analysis we assume that pressure gradient is small in the longitudinal direction, such that blood flow through vessel lumen can be decoupled from the filtration through its wall. In general, osmotic pressure changes with solute concentration c . For small concentrations, the following linear relationship is often considered: $\Pi = RTc$, where R is the gas constant and T is the absolute temperature. Consequently, flow and transport equations are coupled through concentration c that feeds back through Π to the flow. This leads Levick and Michel (2010) to conclude that microvessels cannot absorb fluid from interstitial space, as is often argued. However, this feedback is important mainly when hydrostatic pressure is abruptly reduced, as in the Landis experiment (Landis, 1932), whereas here we are interested in the increase of hydrostatic pressure. We therefore neglect this feedback and solve the flow and transport equations separately, extending the model by considering also low pressures only in Chapter 3.

Under the above assumptions, mass balance of the solvent and the solute leads to the following governing equations for the pressure $P = P(x, y, z, t)$

$$\frac{\partial P}{\partial t} = \frac{k\rho g}{\mu S_s} \nabla^2 P, \quad (2.1)$$

and for the concentration $c = c(x, y, z, t)$

$$\frac{\partial c}{\partial t} + \frac{\mathbf{q}}{n} \cdot \nabla c = \nabla \cdot (\mathbf{D} \cdot \nabla c). \quad (2.2)$$

where k is wall permeability, ρ is blood density, g is the acceleration due to gravity, μ is blood dynamic viscosity, S_s is the specific storage of the porous material, n is the porosity of the material and \mathbf{D} is diffusion tensor.

The specific water (solvent) discharge $\mathbf{q} = \mathbf{q}(x, y, z, t)$ is proportional to the *net pressure* gradient through Starling's equation (Levick, 2010)

$$\mathbf{q} = -\frac{K}{\rho g} \nabla P, \quad (2.3)$$

where

$$K = \frac{k\rho g}{\mu}. \quad (2.4)$$

Finally, mass flux of solute $\mathbf{f}_m = \mathbf{f}_m(x, y, z, t)$ is given by

$$\mathbf{f}_m = (1 - \sigma)\mathbf{q}c - n\mathbf{D} \cdot \nabla c. \quad (2.5)$$

The above equations written in cylindrical coordinates (r, θ, z) and assuming radial symmetry take the following form

$$\frac{\partial P}{\partial t} = \frac{k\rho g}{\mu S_s} \frac{1}{r} \frac{\partial}{\partial r} \left(r \frac{\partial P}{\partial r} \right), \quad (2.6)$$

$$q = -\frac{K}{\rho g} \frac{\partial P}{\partial r}, \quad (2.7)$$

$$\frac{\partial c}{\partial t} + \frac{q}{n} \frac{\partial c}{\partial r} = \left(\frac{d}{r} + \frac{\partial d}{\partial r} \right) \frac{\partial c}{\partial r} + d \frac{\partial^2 c}{\partial r^2}, \quad (2.8)$$

$$f_m = (1 - \sigma)qc - nd \frac{\partial c}{\partial r}. \quad (2.9)$$

Since the initial and boundary conditions are independent from coordinates z and θ , we only consider the radial component d of the diffusion tensor \mathbf{D} .

Furthermore, we assume that d is given by the sum of molecular diffusion d_m and hydrodynamic dispersion $d_h = Aq$, where A is the dispersivity and q is the radial component of specific discharge \mathbf{q} .

In the next section we consider the steady-state solution of the above flow and transport equations.

2.2 Analysis

The steady-state equations for the solvent and for the solute in cylindrical coordinates assume the following form

$$0 = \frac{d}{dr} \left(r \frac{dP}{dr} \right), \quad (2.10)$$

$$\frac{q}{n} \frac{dc}{dr} = \left(\frac{d}{r} + \frac{dd}{dr} \right) \frac{dc}{dr} + d \frac{d^2c}{dr^2}. \quad (2.11)$$

2.2.1 Steady-state solutions for a single-layered vessel wall

We now consider a geometrical situation as depicted in Figure 2.1(a), which shows a cylinder whose inner surface of the endothelial cells is represented by radius r_c and whose outer wall is determined by radius r_g .

In this case, we obtain two generic solutions

$$P(r) = \alpha + \beta \ln r, \quad r \in [r_c, r_o] \quad (2.12)$$

$$c(r) = \delta + \gamma h(r), \quad r \in [r_c, r_o] \quad (2.13)$$

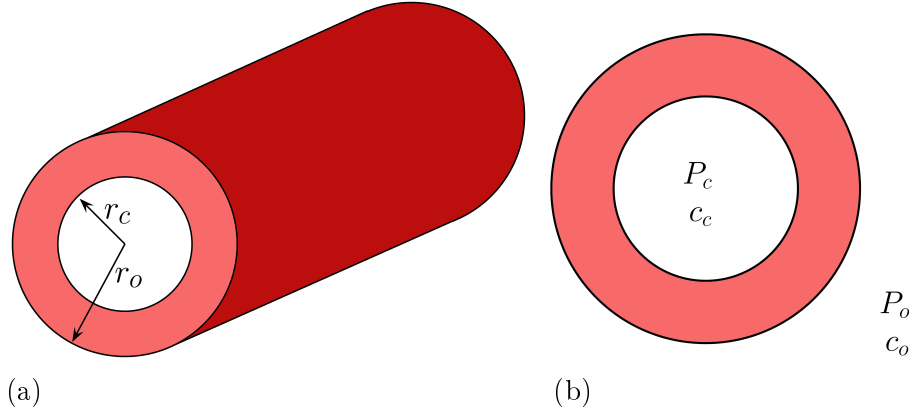


Figure 2.1: (a) The domain is an infinitely long hollow cylinder composed by one layer only, whose inner and outer radii are r_c and r_o . (b) Cross section depicting boundary conditions, where $P_c = p_c - \sigma\Pi_c$ and c_c refer to net blood pressure and solute blood concentration, respectively and $P_o = p_o - \sigma\Pi_o$ and c_o indicate blood pressure and solute concentration in the interstitial fluid.

each of them depending on two parameters which can be computed by imposing boundary conditions, where $h(r)$ is an auxiliary function depending on the permeability and on the boundary conditions

$$h(r) = \begin{cases} -\frac{\mu n}{k\beta} [\mu d_m r - k\beta A] - \frac{k\beta}{n\mu d_m}, & \text{if } k(P_c - P_o) \neq 0 \\ \frac{\ln(\mu d_m r)}{d_m}, & \text{if } k(P_c - P_o) = 0 \end{cases} \quad (2.14)$$

for $r \in [r_c, r_o]$, with

$$\beta = \frac{P_c - P_o}{\ln r_c - \ln r_o}. \quad (2.15)$$

We suppose that boundary conditions are independent from coordinates z and θ . So we set constant pressures and concentrations at the boundary, as depicted in Figure 2.1(b),

$$P(r_c) = P_c, \quad (2.16)$$

$$P(r_o) = P_o, \quad (2.17)$$

$$c(r_c) = c_c, \quad (2.18)$$

$$c(r_o) = c_o, \quad (2.19)$$

where $P_c = p_c - \sigma\Pi_c$ refers to net blood pressure, c_c to solute blood concentration, $P_o = p_o - \sigma\Pi_o$ indicates blood pressure in the interstitial fluid and c_o

the interstitial solute concentration. So we obtain closed-form steady-state solutions for $r \in [r_c, r_o]$, given by

$$P(r) = \frac{P_c \ln(r_o/r) + P_o \ln(r/r_c)}{\ln(r_o/r_c)}, \quad (2.20)$$

$$q(r) = -\frac{k}{\mu r} \frac{P_c - P_o}{\ln r_c - \ln r_o}, \quad (2.21)$$

$$c(r) = \frac{c_c[h(r) - h(r_o)] + c_o[h(r_c) - h(r)]}{h(r_c) - h(r_o)}. \quad (2.22)$$

Mass flux depends on the values of the permeability and on the boundary conditions

$$f_m(r) = \begin{cases} \frac{k\beta}{\mu r} \left[\sigma c(r) - \frac{c_o h(r_c) - c_c h(r_o)}{h(r_c) - h(r_o)} \right], & \text{if } k(c_c - c_o) \neq 0 \\ -\frac{n}{r} \frac{c_c - c_o}{h(r_c) - h(r_o)}, & \text{if } k(c_c - c_o) = 0 \end{cases} \quad (2.23)$$

for $r \in [r_c, r_o]$, with

$$\beta = \frac{P_c - P_o}{\ln r_c - \ln r_o}. \quad (2.24)$$

2.2.2 Steady-state solutions for a vessel wall composed by two layers

We now consider a more complex case in which vessel wall is composed by two layers (r_c, r_g) and (r_g, r_o), as depicted in Figure 2.2(a), with different values of permeability, diffusivity and reflection coefficient. The general case of m layers can be treated similarly.

The generic solution for the pressure assumes the following form

$$\begin{cases} P_1(r) = \alpha_1 + \beta_1 \ln r, & r \in [r_c, r_g] \\ P_2(r) = \alpha_2 + \beta_2 \ln r, & r \in [r_g, r_o] \end{cases} \quad (2.25)$$

while solute concentration is given by

$$\begin{cases} c_1(r) = \delta_1 + \gamma_1 h_1(r), & r \in [r_c, r_g] \\ c_2(r) = \delta_2 + \gamma_2 h_2(r), & r \in [r_g, r_o] \end{cases} \quad (2.26)$$

where, similarly to the previous case, $h_j(r)$ is a function that depends on the

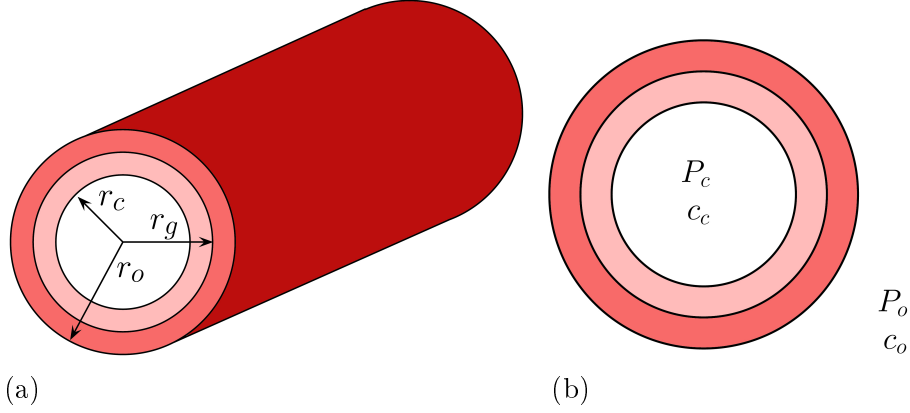


Figure 2.2: (a) The domain is an infinitely long hollow cylinder composed by two layers (r_c, r_g) and (r_g, r_o) . (b) Cross section depicting boundary conditions, where $P_c = p_c - \sigma_1 \Pi_c$ and c_c refer to net blood pressure and solute blood concentration, respectively and $P_o = p_o - \sigma_2 \Pi_o$ and c_o indicate blood pressure and solute concentration in the interstitial fluid.

geometry and the permeability of the layer considered

$$h_j(r) = \begin{cases} -\frac{\mu n}{k_{eq} B} [\mu d_{m_j} r - k_{eq} B A_j] - \frac{k_{eq} B}{n \mu d_{m_j}}, & \text{if } k_1 k_2 (P_c - P_o) \neq 0 \\ \frac{\ln(\mu d_{m_j} r)}{d_{m_j}}, & \text{if } k_1 k_2 (P_c - P_o) = 0 \end{cases} \quad (2.27)$$

for r in the j -th layer, recalling that d_{m_j} is the molecular diffusion and A_j is the dispersivity of the j -th layer. B and k_{eq} are now defined as

$$B = P_c - P_o, \quad (2.28)$$

$$k_{eq} = \frac{k_1 k_2}{k_1 (\ln r_g - \ln r_o) + k_2 (\ln r_c - \ln r_g)}. \quad (2.29)$$

The constants appearing in the above solutions are obtained by imposing suitable boundary conditions for both net pressure and solute concentration, as depicted in Figure 2.2(b)

$$P_1(r_c) = P_c, \quad (2.30)$$

$$P_2(r_o) = P_o, \quad (2.31)$$

$$c_1(r_c) = c_c, \quad (2.32)$$

$$c_2(r_o) = c_o, \quad (2.33)$$

where $P_c = p_c - \sigma_1 \Pi_c$ refers to net blood pressure, c_c to solute blood concentration, $P_o = p_o - \sigma_2 \Pi_o$ indicates blood pressure in the interstitial fluid and c_o the interstitial solute concentration. These boundary conditions should be supplemented by the conditions resulting from imposing the continuity of specific discharge and solute flux at the interface between the two layers at $r = r_g$

$$q_1(r_g) = q_2(r_g), \quad (2.34)$$

$$f_{m,1}(r_g) = f_{m,2}(r_g), \quad (2.35)$$

and that both pressure and solute concentration are continuous at $r = r_g$

$$P_1(r_g) = P_2(r_g), \quad (2.36)$$

$$c_1(r_g) = c_2(r_g). \quad (2.37)$$

With all these conditions, pressures within the first and second layer are given by

$$P_1(r) = \frac{k_2 [P_o \ln(r_c/r) - P_c \ln(r_g/r)] + P_c k_1 \ln(r_g/r_o)}{k_1 \ln(r_g/r_o) + k_2 \ln(r_c/r_g)} \quad (2.38)$$

and

$$P_2(r) = \frac{k_1 [P_o \ln(r_g/r) - P_c \ln(r_o/r)] - P_o k_2 \ln(r_g/r_c)}{k_1 \ln(r_g/r_o) + k_2 \ln(r_c/r_g)} \quad (2.39)$$

respectively.

The resulting expression for specific discharge is the same in the two regions, indeed

$$q(r) = -\frac{k_j}{\mu} \cdot \frac{dP_j}{dr}(r) = -\frac{k_1 k_2 (P_c - P_o)}{\mu [k_1 \ln(r_g/r_o) + k_2 \ln(r_c/r_g)]} \frac{1}{r}, \quad (2.40)$$

for $r \in [r_c, r_o]$, where $j \in \{1, 2\}$ indicates the layer we are considering.

Similarly, under steady-state conditions, solute concentration assumes the following expression

$$c(r) = \begin{cases} c_1(r) = \frac{S_1 + T_1 h_1(r)}{V}, & r \in [r_c, r_g] \\ c_2(r) = \frac{S_2 + T_2 h_2(r)}{V}, & r \in [r_g, r_o] \end{cases} \quad (2.41)$$

where parameters S_1 , T_1 , S_2 , T_2 , V depend on the value of $k_1 k_2 (P_c - P_o)$. Indeed, these parameters are defined as

$$S_1 = \begin{cases} c_c(1 + \sigma_1 - \sigma_2)h_1(r_g)h_2(r_o) - c_o h_1(r_c)h_2(r_g) \\ + c_c(\sigma_2 - \sigma_1)h_1(r_g)h_2(r_g), & \text{if } k_1 k_2(P_c - P_o) \neq 0 \\ c_o h_1(r_c) - c_c[h_1(r_g) - h_2(r_g) + h_2(r_o)], & \text{if } k_1 k_2(P_c - P_o) = 0 \end{cases} \quad (2.42)$$

$$T_1 = \begin{cases} [c_o - c_c(1 - \sigma_1 + \sigma_2)] h_2(r_g) + c_c(\sigma_2 - \sigma_1)h_2(r_o), & \text{if } k_1 k_2(P_c - P_o) \neq 0 \\ c_c - c_o, & \text{if } k_1 k_2(P_c - P_o) = 0 \end{cases} \quad (2.43)$$

$$S_2 = \begin{cases} c_c h_1(r_g)h_2(r_o) + c_o(\sigma_2 - \sigma_1)h_1(r_g)h_2(r_g) + \\ - c_o(1 - \sigma_1 + \sigma_2)h_1(r_c)h_2(r_g), & \text{if } k_1 k_2(P_c - P_o) \neq 0 \\ c_o[h_1(r_c) - h_1(r_g) + h_2(r_g)] - c_c h_2(r_o), & \text{if } k_1 k_2(P_c - P_o) = 0 \end{cases} \quad (2.44)$$

$$T_2 = \begin{cases} [c_o(1 + \sigma_1 - \sigma_2) - c_c] h_1(r_g) + c_o(\sigma_2 - \sigma_1)h_1(r_c), & \text{if } k_1 k_2(P_c - P_o) \neq 0 \\ c_c - c_o, & \text{if } k_1 k_2(P_c - P_o) = 0 \end{cases} \quad (2.45)$$

$$V = \begin{cases} (\sigma_2 - \sigma_1)[h_1(r_g)h_2(r_g) - h_1(r_c)h_2(r_o)] + \\ -(1 - \sigma_1 + \sigma_2)h_1(r_c)h_2(r_g) + (1 + \sigma_1 - \sigma_2)h_1(r_g)h_2(r_o), & \text{if } k_1 k_2(P_c - P_o) \neq 0 \\ h_1(r_c) - h_1(r_g) + h_2(r_g) - h_2(r_o), & \text{if } k_1 k_2(P_c - P_o) = 0. \end{cases} \quad (2.46)$$

The resulting solute flux is the following

$$f_{m,j}(r) = \begin{cases} \frac{k_{eq}B}{\mu r} \left[\sigma_j c_j(r) - \frac{S_j}{V} \right], & \text{if } k_1 k_2(P_c - P_o) \neq 0 \\ -\frac{nT_j}{V} \frac{1}{r}, & \text{if } k_1 k_2(P_c - P_o) = 0 \end{cases} \quad (2.47)$$

for r in the j -th layer, where $j \in \{1, 2\}$ indicates the layer we are considering

and σ_j represents the reflection coefficient that may be different in the two layers.

Similar expressions may be obtained for three and more layers.

2.2.3 The travel time through the vessel wall

An important quantity in exchange processes is the time a single solute molecule takes to cross vessel wall. We call this time the *travel time* τ , in analogy with transport in porous media.

For the single layer case, τ may be approximated by neglecting the diffusive component of the mass flux

$$\tau = \int_{r_c}^{r_o} \frac{n}{(1-\sigma)q(r)} dr = - \frac{n\rho g}{P_c - P_o} \frac{\ln r_c - \ln r_o}{K(1-\sigma)} \frac{r_o^2 - r_c^2}{2}. \quad (2.48)$$

2.3 Preliminary results

The structure of the vessels is very specialised in relation to their functionality and this specialisation results in different permeability and reflection coefficients of vessel wall. Table 2.1 shows typical values of geometrical properties of microvessels together with hydraulic conductivity to serum albumin and the reflection coefficient. Although permeability of venules is expected to be larger than permeability of arterioles, in absence of specific data, and for illustration purposes in the subsequent exercise we assumed the same permeability for both microvessels.

Parameter [unit]	Value	Reference
K [kg sec ⁻³ (cm H ₂ O) ⁻¹]	$2.49 \cdot 10^{-12}$	Michel and Curry (1999)
σ	0.85	Michel (1980)
n	0.5	Robinson (1988)
r_A [μm]	15	Silverthorn (2009)
r_V [μm]	10	Silverthorn (2009)
Δx_A [μm]	6	Silverthorn (2009)
Δx_V [μm]	1	Silverthorn (2009)

Table 2.1: Typical values of the parameters used in the computation. K is the hydraulic conductivity for serum albumin, σ is the reflection coefficient for serum albumin, n is the porosity, r is the mean radius of the vessel and Δx is the vessel thickness. A refers to the arteriolar end of capillary bed, while V to the venous end.

In addition, venules and arterioles are subjected to different internal hydrostatic pressures and external osmotic pressures. Table 2.2 shows the typical mean pressures in different microvessels.

Location	p_c	p_o	$\sigma\Pi_c$	$\sigma\Pi_o$	ΔP
	cm H ₂ O				
arteriolar end of capillary	47.62	-2.72	38.10	0.14	12.38
venular end of capillary	20.41	-2.72	38.10	4.08	-10.88

Table 2.2: Mean pressures in human body, taken from Boron and Boulpaep (2005). p represents hydrostatic pressure, while Π is osmotic pressure and σ is the reflection coefficient. The subscript c refers to the pressure measured inside the vessel, while the subscript o is measured just outside the vessel. ΔP is defined as the difference of the net pressure P between the internal and the external side of microvessels, i.e. $\Delta P = P_c - P_o = (p_c - \sigma\Pi_c) - (p_o - \sigma\Pi_o)$.

The difference of net pressure P between the internal (subscript c) and the external side (subscript o) of the microvessels, i.e.

$$\Delta P = P_c - P_o = (p_c - \sigma\Pi_c) - (p_o - \sigma\Pi_o), \quad (2.49)$$

provides a first rough quantification of the expected flux through vessel wall per unit area, i.e. specific discharge. In Table 2.2, we observe that ΔP is positive for arterioles (12.38 cm H₂O) and negative for venules (-10.88 cm H₂O). This leads to a tendency for absorption at the venular end of capillary bed, which may be contrasted by the parallel increase of osmotic pressure within the clefts just downstream glycocalyx, the membrane coating the internal surface of endothelial cells (Levick, 2010). As mentioned before, in the present chapter we neglect this feedback mechanism.

We start by considering microvessel wall composed by a single layer. Figure 2.3 shows the specific discharge q crossing vessel wall as a function of hydrostatic pressure p_c for both arterioles and venules.

In the case in which vessel wall is composed by only one layer, we can study the behaviour of the discharge per unit length and of the travel time of a molecule, assuming that external pressures p_o and Π_o and internal osmotic pressure Π_c are constant. Luminal hydrostatic pressure p_c is the residual pressure, controlled by cardiac pressure, so we can represent our quantities with respect to it.

For typical values of venular pressure (see the blue bullet on the solid line in Figure 2.3), specific discharge is negative, meaning that venules absorb fluid and dissolved molecules from interstitial volume. On the other hand, arteriolar pressure is positive letting oxygen and nutrients nourish the surrounding tissues.

In Figure 2.4, travel time τ of a target molecule (in this case, serum

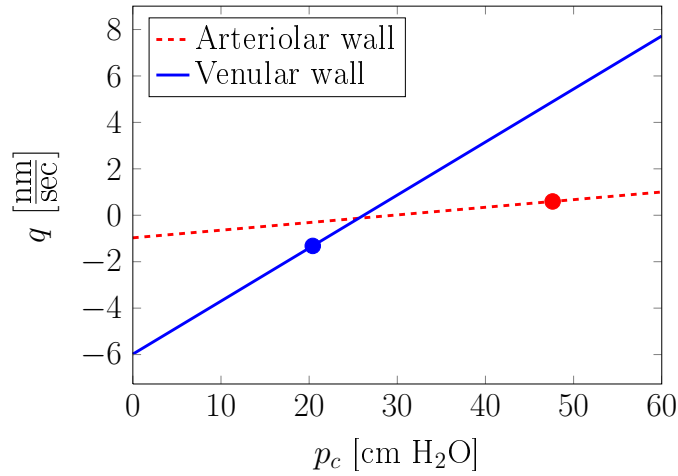


Figure 2.3: Discharge per unit length depending on internal hydrostatic pressure, in the arteriolar (dashed line) and in the venular case (solid line). The bullets represent the typical values of internal blood pressure in both cases.

albumin) is depicted with respect to internal hydrostatic pressure p_c for arteriolar (dashed curve) and venular end (solid curve) of capillary beds.

For typical values of internal pressure (see the bullets in Figure 2.4), τ is positive for arterioles and negative for venules, reflecting the opposite direction of the flow in the two cases. An increase of hydrostatic pressure leads to a reduction of τ for arterioles. In the case of venules, the same increase leads to a larger travel time $|\tau|$. Both occurrences may induce a significant alteration of the exchange mechanisms between the interstitial fluid and the cells. If hydrostatic pressure increases above a given threshold (about 26 cm H₂O, in the present case), flux is inverted across venular wall and travel time becomes positive, thereby leading to leakage of hematic fluid from venules into interstitial volume. Close to this threshold τ is large, but it reduces rapidly as hydrostatic pressure further increases.

Finally, we observe that our simple model is in agreement with the early experiments conducted by Landis (1932) in frog mesenteric capillaries.

2.4 Conclusions

We have presented a simplified analytical model of steady-state flow and transport of a target molecule through the wall of microvessels. The advantage of this model is that it allows us to easily explore the explicit influence of the many parameters controlling transport processes and thereby avoiding, for the time being, the use of numerical methods. With this model we have performed a preliminary analysis of the flux across arterioles and venules by

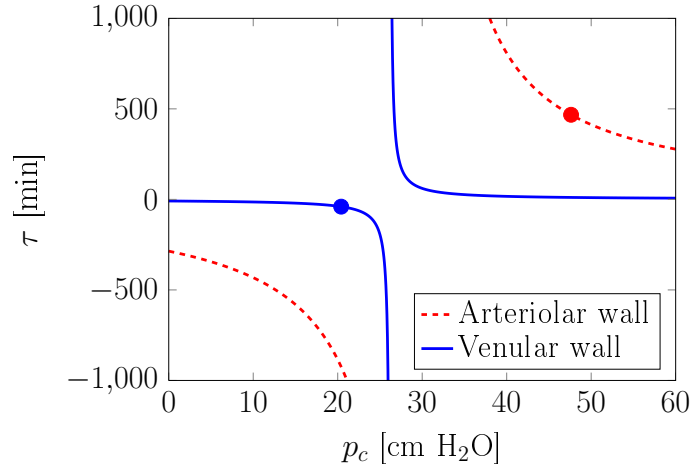


Figure 2.4: Travel time of a molecule of serum albumin, in arterioles (dashed curve) and in venules (solid curve). The bullets represent the typical values of internal blood pressure in both cases.

using parameters taken from existing studies on mesenteric capillaries. In both cases we computed the time a target molecule (with a given reflection coefficient) spends crossing vessel wall, which may provide an indication of the alteration of exchange mechanisms due to modification of hydrostatic pressure at arteriolar and venular ends.

An increase of hydrostatic pressure above the value observed in normal conditions leads to an increase of the flux crossing the wall of arterioles and a corresponding reduction of travel time. In this condition more hydrophilic molecules are released in interstitial fluid surrounding the vessel, thereby potentially reducing downstream the availability of such substances needed for cell metabolism. On venular side, a threshold hydrostatic pressure separates two different ways of functioning. For hydrostatic pressures below such a threshold, flux is negative and venules absorb fluid from the interstitial space, while above this threshold venules leak hematic fluid to interstitial space. An increase of hydrostatic pressure has then a different impact according to the reference hydrostatic pressure. For low reference pressure (i.e. below the threshold) an increase of hydrostatic pressure leads to a reduction of absorption and a parallel increase of travel time. However, if the reference pressure is larger than this threshold, venules behave similarly to arterioles and leak hematic fluid to interstitial space with a travel time that reduces rapidly with the increase of hydrostatic pressure.

Chapter 3

A coupled steady-state model

*The steady-state model presented in this Chapter
is taken from Facchini et al. (2013b).*

The classical way to model flow and transport across a micro-vessel is to represent the glycocalyx and the clefts as an homogeneous membrane, with equivalent properties. *Starling's law* is then applied to this homogenised composite, such that capillary filtration rate can be written as proportional to the difference between the hydrostatic and osmotic pressure drops between blood and interstitial fluid (Fu et al., 1994; Zhang et al., 2006). This simple conceptual model has been shown to be unable to interpret the experiments conducted by Landis (1932) and successively by Adamson et al. (2004) and Hu et al. (2000).

In one of his experiments, Landis (1932) showed that at steady state, fluid exchange in perfused single capillaries of frog mesentery did not invert direction, leading to absorption, when hydrostatic pressure inside the lumen was lowered below the limit value that Starling's law indicates for inversion (Levick, 2010). As a possible interpretation of the apparent breakdown of Starling's law, Michel (1997) and Weinbaum (1998) argued that filtration rate may be controlled by the drop of osmotic pressure between the lumen and a position in the cleft at the contact with glycocalyx, rather than the interstitium. This leads to an important change in the conceptual model, ruling out models with a single equivalent homogeneous membrane lumping the effect of both glycocalyx and clefts at the junctions of endothelial cells.

We thus consider vessel wall as a structure composed by two layers representing glycocalyx and endothelium. This is evidenced by electron micrograph after perfusion with cationized ferritin (Turner et al., 1983) and reflects morphometric measurements performed later (Hu et al., 2000; Adamson et al., 2004; Levick, 2010).

3.1 The mathematical model

3.1.1 Statement of the problem

We idealise micro-vessel wall as two concentric hollow cylinders representing (from the lumen outward) glycocalyx and the surrounding endothelial cells. The two hollow cylinders are considered rigid, owing to the small compliance of micro-vessels, including venules (Levick, 2010). The resulting computational domain is shown in Figure 3.1 with the dimensions of the two membranes reported in Table 3.1. Blood flow is along the longitudinal axis of micro-vessel and we assume that variation of target macro-molecule concentration is small along flow direction (Intaglietta et al., 1996).

A widely accepted rheological model of blood flowing in vessel considers an internal Red Blood Cells (RBCs) rich inner core surrounded by a relatively thin plasma layer, which can be well approximated as a Newtonian fluid (Sriram et al., 2011). With the further assumption that the two cylindrical layers are homogeneous, flow across micro-vessel wall is radial and at a first approximation controlled by local hydrostatic and osmotic pressures. In addition, we consider the case of a single not reacting molecule and isothermal conditions (Katchalsky and Curran, 1965).

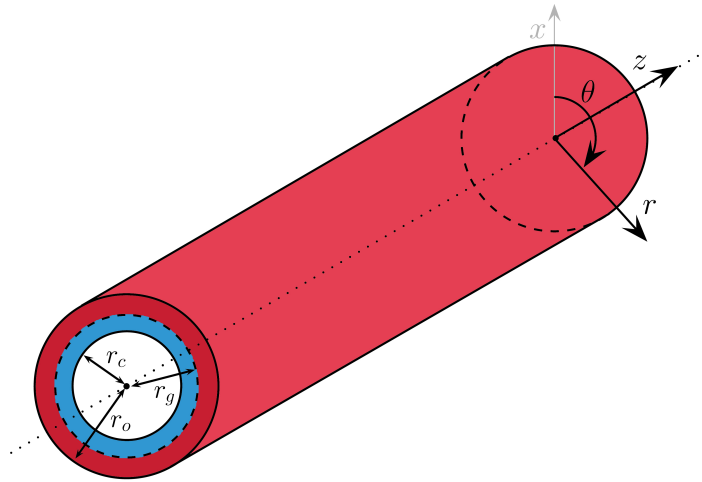


Figure 3.1: Sketch of the domain: a long hollow circular cylinder composed by two homogeneous porous membranes representing glycocalyx for $r \in (r_c, r_g)$ and endothelial cells for $r \in (r_g, r_o)$.

3.1.2 Governing equations

Under the above hypotheses, solvent flow q_v and diffusional macro-molecule flow q_d through micro-vessel wall are coupled and given by the following

phenomenological equations (Katchalsky and Curran, 1965):

$$\begin{aligned} q_v &= -\ell_p(\nabla p - \sigma \nabla \Pi), \\ q_d &= \sigma \ell_p \nabla p - \ell_d \nabla \Pi, \end{aligned} \quad (3.1)$$

where p is hydrostatic pressure and Π is osmotic pressure, which emerges because macro-molecule size is comparable to the size of the apertures in glycocalyx and in endothelial cells. In addition, $\ell_p = k/\mu$ is the ratio between hydraulic permeability of the membrane and solvent viscosity, $\sigma \in [0, 1]$ is membrane reflection coefficient and ℓ_d is diffusional permeability (Michel and Curry, 1999). Equations (3.1) are written for a single macro-molecule. In case of two or more macromolecules the terms involving osmotic pressure should be summed over all the relevant macromolecules. Osmotic pressure depends on the solute (macro-molecule) concentration c , through the following expression (Levick, 2010):

$$\Pi = RTc, \quad (3.2)$$

where R is the gas constant and T is the absolute temperature.

The reflection coefficient σ in equations (3.1) reflects the hindrance exerted by the pore to free movement of macromolecules and approaches zero as the characteristic size of the pore is much larger than the characteristic size of macromolecules. In this situation, which is typical of small molecules, the effect of osmotic pressure tends to zero and diffusion coefficient tends to free diffusion coefficient, which depends only on the characteristics of the molecule and the temperature.

The total flux q_s of macromolecules is given by the sum of convective and diffusive components:

$$q_s = c(q_v + q_d). \quad (3.3)$$

Mass conservation of the flowing solvent and of macromolecules under steady-state conditions leads to the following governing equations:

$$\begin{cases} \nabla \cdot q_v = 0, \\ \nabla \cdot q_s = 0, \end{cases} \quad (3.4)$$

which written in a radial coordinate system assume the following form:

$$\begin{cases} \frac{d}{dr} \left(r \ell_p \frac{dp}{dr} \right) - \frac{d}{dr} \left(r \ell_p \sigma \frac{d\Pi}{dr} \right) = 0, \\ \frac{d}{dr} \left[r \ell_p (\sigma - 1) \frac{\Pi}{RT} \frac{dp}{dr} \right] + \frac{d}{dr} \left[r (\ell_p \sigma - \ell_d) \frac{\Pi}{RT} \frac{d\Pi}{dr} \right] = 0, \end{cases} \quad (3.5)$$

defined in the interval $r \in (r_c, r_o)$ from the lumen side of glycocalyx to the external surface of endothelial cells.

In the present chapter we seek the analytical solution of this system of two non-linear coupled equations subjected to the following boundary conditions (Figure 3.2):

$$p_c = p(r_c), \quad p_o = p(r_o), \quad \Pi_c = \Pi(r_c), \quad \Pi_o = \Pi(r_o), \quad (3.6)$$

where subscripts c and o indicate the internal surface of glycocalyx and the external surface of endothelial cells, respectively.

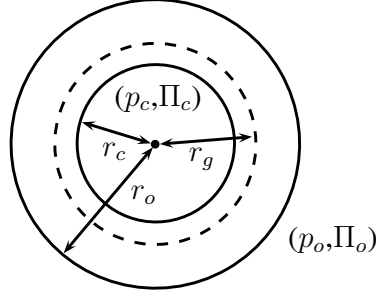


Figure 3.2: Sketch of the domain indicating the relevant geometric elements: the internal radius r_c at luminal side of micro-vessel, the radius of the interface between glycocalyx and endothelial cells, r_g , and the external radius r_o . In addition, p_c and Π_c are hydrostatic and osmotic pressures, respectively, within the lumen, while p_o and Π_o are the same quantities in the external interstitial space.

3.1.3 Dimensionless flow and transport equations

To facilitate the analysis, it is convenient to make the above steady-state flow and transport equations (3.5) dimensionless with respect to the following reference quantities: vessel wall thickness, $\Delta r = r_o - r_c$, for the length; interstitial hydrostatic pressure, $|p_o|$, for both hydrostatic and osmotic pressures; ℓ_p^H for both ℓ_p and ℓ_d , where ℓ_p^H is the weighted harmonic mean for hydraulic conductivity of the two layers composing micro-vessel wall:

$$\ell_p^H = \frac{r_o - r_c}{\frac{r_g - r_c}{\ell_p^G} + \frac{r_o - r_g}{\ell_p^W}}, \quad (3.7)$$

with ℓ_p^G and ℓ_p^W indicating hydraulic conductivity of glycocalyx and endothelial cells layer, respectively. In addition, the dimensionless radius is defined as follows: $r = (r^* - r_c)/\Delta r = r^*/\Delta r - \xi$, where r^* indicates the dimensional radius varying from $r^* = r_c$ to $r^* = r_o$ and $\xi = r_c/\Delta r$. With this definition the dimensionless radius r lies between 0 and 1.

After these preliminary steps, system (3.5) assumes the following dimensionless form (hereafter all the quantities are considered dimensionless, unless otherwise stated):

$$\begin{cases} \frac{d}{dr} \left(\mathcal{F} \frac{dp}{dr} \right) + \frac{d}{dr} \left(\mathcal{G} \frac{d\Pi}{dr} \right) & = 0, \\ \Pi \left[\frac{d}{dr} \left(\mathcal{H} \frac{dp}{dr} \right) + \frac{d}{dr} \left(\mathcal{L} \frac{d\Pi}{dr} \right) \right] + \frac{d\Pi}{dr} \left(\mathcal{H} \frac{dp}{dr} + \mathcal{L} \frac{d\Pi}{dr} \right) & = 0, \end{cases} \quad (3.8)$$

where the auxiliary functions \mathcal{F} , \mathcal{G} , \mathcal{H} and \mathcal{L} are defined as follows:

$$\begin{aligned} \mathcal{F}(r) &= (r + \xi) \ell_p(r), \\ \mathcal{G}(r) &= -(r + \xi) \ell_p(r) \sigma(r), \\ \mathcal{H}(r) &= (r + \xi) \ell_p(r) [\sigma(r) - 1], \\ \mathcal{L}(r) &= (r + \xi) [\ell_p(r) \sigma(r) - \ell_d(r)]. \end{aligned} \quad (3.9)$$

In addition, we consider the following boundary conditions, which are the dimensionless counterpart of equations (3.6):

$$\begin{aligned} p(r=0) &= p_c, & p(r=1) &= p_o, \\ \Pi(r=0) &= \Pi_c, & \Pi(r=1) &= \Pi_o. \end{aligned} \quad (3.10)$$

3.1.4 Discharge and flux reconstruction

Solvent (volume) and solute fluxes are given by the following expressions:

$$\begin{cases} q_v &= -\ell_p \left(\frac{dp}{dr} - \sigma \frac{d\Pi}{dr} \right), \\ q_s &= \Pi \left[\ell_p(\sigma - 1) \frac{dp}{dr} + (\ell_p \sigma - \ell_d) \frac{d\Pi}{dr} \right], \end{cases} \quad (3.11)$$

which are written in the dimensionless form with respect to the quantities introduced in Section 3.1.3. Finally, the total fluxes of solvent and solute crossing the micro-vessel wall are given by:

$$J_v = \int_0^{2\pi} q_v(r) (r + \xi) d\theta = -2\pi(r + \xi) \ell_p \left(\frac{dp}{dr} - \sigma \frac{d\Pi}{dr} \right), \quad (3.12)$$

$$J_s = \int_0^{2\pi} q_s(r) (r + \xi) d\theta = 2\pi(r + \xi) \Pi \left[\ell_p(\sigma - 1) \frac{dp}{dr} + (\ell_p \sigma - \ell_d) \frac{d\Pi}{dr} \right], \quad (3.13)$$

where θ is the angle as depicted in Figure 3.1, while volume and solute fluxes are dimensionless with respect to $\ell_p^H |p_o|$ and $\ell_p^H |p_o|^2 / (RT)$, respectively. Notice that in the latter two expressions all quantities are dimensional.

With the material properties defined through the dimensionless counterpart of equations (1.7), namely

$$\begin{cases} \sigma(r) &= \frac{\sigma_G + \sigma_W}{2} + \frac{\sigma_G - \sigma_W}{2} w(r - r_g), \\ \ell_p(r) &= \frac{\ell_p^G + \ell_p^W}{2} + \frac{\ell_p^G - \ell_p^W}{2} w(r - r_g), \\ \ell_d(r) &= \frac{\ell_d^G + \ell_d^W}{2} + \frac{\ell_d^G - \ell_d^W}{2} w(r - r_g), \end{cases} \quad (3.14)$$

the solutions of hydrostatic and osmotic pressures are differentiable everywhere, while transition between material properties of the two layers is controlled by parameter ε .

3.1.5 Analytical solution of the single- and two-layered model

The two differential equations composing system (3.8) can be integrated with respect to r leading to the following expressions for the fluxes:

$$\begin{cases} k_1 &= (r + \xi) \ell_p \left(\frac{dp}{dr} - \sigma \frac{d\Pi}{dr} \right), \\ k_2 &= (r + \xi) \Pi \left[\ell_p (\sigma - 1) \frac{dp}{dr} + (\ell_p \sigma - \ell_d) \frac{d\Pi}{dr} \right]. \end{cases} \quad (3.15)$$

After some algebraic manipulations, system (3.15) can be written in the following form:

$$\begin{cases} k_1 &= (r + \xi) \ell_p \left(\frac{dp}{dr} - \sigma \frac{d\Pi}{dr} \right), \\ k_2 &= \Pi \left[(\sigma - 1) k_1 + (r + \xi) (\ell_p \sigma^2 - \ell_d) \frac{d\Pi}{dr} \right]. \end{cases} \quad (3.16)$$

The single homogeneous layer solution

The second equation of system (3.16) contains only the osmotic pressure Π as unknown and therefore can be solved analytically with boundary conditions (3.10) for the case of a single equivalent layer, and with additional conditions at the interface between the layers in case of multiple layers.

We consider first the case of a single layer with equivalent membrane properties. In this case the solution of the system (3.16) is:

$$\Pi(r) = \frac{k_2}{k_1} \frac{1}{\sigma - 1} \left[1 + W \left(k_4 (r + \xi) - \frac{(k_1)^2 (\sigma - 1)^2}{k_2 (\ell_p \sigma^2 - \ell_d)} \right) \right], \quad (3.17)$$

for osmotic pressure Π and

$$\begin{aligned} p(r) &= \frac{k_1}{\ell_p} \ln(r + \xi) + k_3 + \sigma \Pi(r) = \\ &= \frac{k_1}{\ell_p} \ln(r + \xi) + k_3 + \frac{k_2}{k_1} \frac{\sigma}{\sigma - 1} \left[1 + W \left(k_4 (r + \xi)^{-\frac{(k_1)^2 (\sigma - 1)^2}{k_2 \ell_p \sigma^2 - \ell_d}} \right) \right], \end{aligned} \quad (3.18)$$

for hydrostatic pressure, when both k_1 and k_2 are non-zero and material properties ℓ_p , ℓ_d and σ are equivalent parameters. In equations (3.17) and (3.18), $W(z)$ is the *Lambert W function* (see e.g. Corless et al., 1996; Barry et al., 2000), also called *omega function* or *product logarithm*, which is the solution of the following algebraic non-linear equation:

$$z = W(z) e^{W(z)}. \quad (3.19)$$

The solutions (3.17) and (3.18) require that four constants k_1 , k_2 , k_3 and k_4 be evaluated by imposing boundary conditions on the hydrostatic and osmotic pressures at the lumen and external surfaces of micro-vessel. This leads to the following explicit expressions for k_1 , k_3 and k_4 :

$$k_1 = \ell_p \frac{(p_c - p_o) - \sigma(\Pi_c - \Pi_o)}{\ln(\xi) - \ln(1 + \xi)}, \quad (3.20)$$

$$k_3 = \frac{(p_o - \sigma \Pi_o) \ln(\xi) - (p_c - \sigma \Pi_c) \ln(1 + \xi)}{\ln(\xi) - \ln(1 + \xi)}, \quad (3.21)$$

$$k_4 = f e^f \xi^\delta, \quad (3.22)$$

where $f = (k_1/k_2)(\sigma - 1)\Pi_c - 1$ and $\delta = k_1^2(\sigma - 1)^2 / [k_2(\ell_p \sigma^2 - \ell_d)]$.

By imposing that the osmotic pressure be equal to Π_c at $r = r_c$ we obtain, after a few manipulations, the following expression in the only unknown k_2 , provided that k_1 is given by equation (3.20):

$$\left[\frac{k_1}{k_2} (\sigma - 1) \Pi_o - 1 \right] e^{\frac{k_1}{k_2} (\sigma - 1) \Pi_o - 1} - f e^f \left(\frac{\xi}{1 + \xi} \right)^{\frac{(k_1)^2 (\sigma - 1)^2}{k_2 \ell_p \sigma^2 - \ell_d}} = 0. \quad (3.23)$$

Equation (3.23) can be solved by using a *Newton-Raphson method* (Hildebrand, 1987) with the following initial guess:

$$k_2 = \frac{\Pi_c + \Pi_o}{2} \frac{\ell_p (\sigma - 1) (p_c - p_o) + (\ell_p \sigma - \ell_d) (\Pi_c - \Pi_o)}{\ln(r_c + \xi) - \ln(r_o + \xi)}, \quad (3.24)$$

which is the exact solution of equation (3.23) in the special case of $k_1 = 0$.

The multiple layer solution

Expressions (3.17) and (3.18) for osmotic and hydrostatic pressures can be applied to all the layers of a multi-layered microvessel, provided that the constants k_3 and k_4 are layer-specific and that properties ℓ_p , ℓ_d and σ are discontinuous across the boundary between adjacent layers. On the other hand, k_1 and k_2 are global quantities since they are equal to volume and solute mass fluxes (divided by $\mp 2\pi$) crossing microvessel wall. Therefore, in addition to the 4 boundary conditions at the inner and outer surfaces, continuity of hydrostatic and osmotic pressures as well as constancy of volumetric and macro-molecule fluxes should be imposed at each interface. This results in a system of $2n + 2$ equations, in the same number of unknown consisting in the n values of both k_3 and k_4 , which are layer-specific quantities in addition to the two global quantities k_1 and k_2 . In particular, for the two-layered model besides the boundary conditions (3.10) the following continuity conditions should be imposed at the interface between the first and second layer at $r = r_g$:

$$p_1(r_g) = p_2(r_g); \quad \Pi_1(r_g) = \Pi_2(r_g), \quad (3.25)$$

where the subscripts “1” and “2” refers to the solution within the first (glycocalyx) and the second (endothelial cells) layer.

The case of a smooth transition of these properties between adjacent layers will be discussed subsequently with the help of numerical solutions.

The imposition of the pressures at the inner surface of glycocalyx equal to the pressures in the blood stream and of the pressures at the outer surface of endothelial cells equal to the pressures in the interstitium leads to the following expressions for k_3^i and k_4^i :

$$k_3^G = (p_c - \sigma_G \Pi_c) - \frac{k_1}{\ell_p^G} \ln(\xi), \quad (3.26)$$

$$k_3^W = (p_o - \sigma_W \Pi_o) - \frac{k_1}{\ell_p^W} \ln(1 + \xi), \quad (3.27)$$

$$k_4^G = f_G e^{f_G \xi^{\delta_G}}, \quad (3.28)$$

$$k_4^W = f_W e^{f_W (1 + \xi)^{\delta_W}}, \quad (3.29)$$

where

$$\begin{aligned} f_G &= \frac{k_1}{k_2} (\sigma_G - 1) \Pi_c - 1, \\ f_W &= \frac{k_1}{k_2} (\sigma_W - 1) \Pi_o - 1, \\ \delta_G &= \frac{(k_1)^2 (\sigma_G - 1)^2}{k_2 \ell_p^G \sigma_G^2 - \ell_d^G}, \\ \delta_W &= \frac{(k_1)^2 (\sigma_W - 1)^2}{k_2 \ell_p^W \sigma_W^2 - \ell_d^W}. \end{aligned} \quad (3.30)$$

By substituting the layer-specific quantities k_3^i and k_4^i into equations (3.25) we obtain the following two equations in the two unknowns k_1 and k_2 :

$$g_1 e^{g_1} - f_G e^{f_G} \left(\frac{\xi}{r_g + \xi} \right)^{\delta_G} = 0, \quad (3.31)$$

$$g_2 e^{g_2} - f_W e^{f_W} \left(\frac{1 + \xi}{r_g + \xi} \right)^{\delta_W} = 0, \quad (3.32)$$

where g_1 and g_2 assume the following expressions

$$g_1 = \frac{k_1 - \sigma_G - 1}{k_2 \sigma_G - \sigma_W} [(p_o - \sigma_W \Pi_o) - (p_c - \sigma_G \Pi_c) + k_1 \beta] - 1, \quad (3.33)$$

$$g_2 = \frac{\sigma_W - 1}{\sigma_G - 1} (1 + g_1) - 1, \quad (3.34)$$

with $\sigma_G \neq \sigma_W$ and

$$\beta = \frac{\ell_p^W \ln(\xi) + (\ell_p^G - \ell_p^W) \ln(r_g + \xi) - \ell_p^G \ln(1 + \xi)}{\ell_p^G \ell_p^W}. \quad (3.35)$$

In case the reflection coefficients are the same in both layers (i.e. $\sigma_G = \sigma_W$), equations (3.31)-(3.32) become

$$f_G e^{f_G} \left(\frac{\xi}{r_g + \xi} \right)^{\delta_G} - f_W e^{f_W} \left(\frac{1 + \xi}{r_g + \xi} \right)^{\delta_W} = 0, \quad (3.36)$$

with

$$k_1 = \frac{\ell_p^G \ell_p^W [(p_c - p_o) - \sigma(\Pi_c - \Pi_o)]}{\ell_p^W \ln(\xi) + (\ell_p^G - \ell_p^W) \ln(r_g + \xi) - \ell_p^G \ln(1 + \xi)}, \quad (3.37)$$

where $\sigma := \sigma_G = \sigma_W$.

Equations (3.31) and (3.32) can be solved by using a Newton-Raphson method with the initial guess for the unknowns k_1 and k_2 obtained by computing volumetric and solute mass fluxes for the case in which interstitial pressures are applied to the external surface of glycocalyx at $r = r_g$. These fluxes can be obtained analytically exactly for k_1 and as a first-order approximation for k_2 , as follows:

$$k_1^{(0)} = \ell_p^G \frac{(p_c - p_o) - \sigma(\Pi_c - \Pi_o)}{\ln(\xi) - \ln(r_g + \xi)}, \quad (3.38)$$

$$k_2^{(0)} = \Pi_o k_1 (\sigma_G - 1). \quad (3.39)$$

3.1.6 Approximate analytical solutions for a single-layered microvessel

The first equation of system (3.8) can be written as a function of net pressure $P(r) = p(r) - \sigma\Pi(r)$ as follows:

$$(r + \xi)\ell_p \frac{dP}{dr} = c_1, \quad (3.40)$$

then the linearised version of the second equation of system (3.16), obtained by decomposing osmotic pressures in a mean value Π_M plus a perturbation $\epsilon(r)$ and neglecting the terms of the second and higher order in the perturbation, assume the following form:

$$(\sigma - 1) c_1 \frac{d\epsilon}{dr} + (\ell_p \sigma^2 - \ell_d) \Pi_M \left[\frac{d\epsilon}{dr} + (r + \xi) \frac{d^2\epsilon}{dr^2} \right] = 0, \quad (3.41)$$

in the unknown function ϵ .

Equations (3.40)-(3.41) with boundary conditions

$$\begin{cases} P(0) = P_c = p_c - \sigma\Pi_c, \\ P(1) = P_o = p_o - \sigma\Pi_o, \\ \epsilon(0) = \Pi_c - \Pi_M = \frac{\Pi_c - \Pi_o}{2}, \\ \epsilon(1) = \Pi_o - \Pi_M = -\frac{\Pi_c - \Pi_o}{2}, \end{cases} \quad (3.42)$$

can be separately solved analytically to obtain:

$$\begin{aligned} P(r) &= c_1 \ln(r + \xi) + c_3, \\ \Pi(r) &= c_2 (r + \xi)^{-\beta} + c_4, \\ p(r) &= P(r) + \sigma\Pi(r) = c_1 \ln(r + \xi) + \sigma c_2 (r + \xi)^{-\beta} + c_3 + \sigma c_4, \end{aligned} \quad (3.43)$$

where the coefficients assume the following expressions:

$$\begin{aligned} c_1 &= \frac{(p_c - p_o) - \sigma(\Pi_c - \Pi_o)}{\ln(\xi) - \ln(1 + \xi)}, \\ c_2 &= \frac{\xi^{-\beta} - (1 + \xi)^{-\beta}}{\Pi_c - \Pi_o}, \\ c_3 &= \frac{[p_o \ln(\xi) - p_c \ln(1 + \xi)] - \sigma[\Pi_o \ln(\xi) - \Pi_c \ln(1 + \xi)]}{\ln(\xi) - \ln(1 + \xi)}, \\ c_4 &= \frac{\Pi_c \xi^\beta - \Pi_o (1 + \xi)^\beta}{\xi^\beta - (1 + \xi)^\beta}, \end{aligned} \quad (3.44)$$

for

$$\beta = \frac{2(\sigma - 1)}{\ell_p \sigma^2 - \ell_d} \frac{(p_c - p_o) - \sigma(\Pi_c - \Pi_o)}{[\ln(\xi) - \ln(1 + \xi)](\Pi_c + \Pi_o)} \neq 0. \quad (3.45)$$

3.1.7 Parameters of two-layered model

Table 3.1 shows typical values of geometrical and physiological characteristics of an intact vessel, as well as the values of osmotic and hydrostatic pressures within the lumen and in the external interstitial space used in the present study.

The analytical solution for the two-layered case presented in Section 3.1.5 has been obtained assuming a discontinuous transition of properties at the interface between glycocalyx and endothelial cells. Smoother transitions are also possible and will be analysed successively, by using a suitable numerical solution.

Thermodynamic considerations on the phenomenological equations (3.1) discussed in Katchalsky and Curran (1965), lead to the following constraint:

$$\text{Pe} < \frac{1}{\sigma^2}, \quad (3.46)$$

where $\text{Pe} = \ell_p/\ell_d$ is a *Péclet number*, which represents the reciprocal strength of advective and diffusive transport processes: when Pe is high advection dominates over diffusion and vice-versa when Pe is small.

Parameter [unit]	Value	Reference
r_c [μm]	5	Charm and Kurland (1974)
r_g [μm]	5.15	Adamson et al. (2004)
r_o [μm]	5.5	Charm and Kurland (1974)
Π_c [mmHg]	25	Levick (1991)
Π_o [mmHg]	12	Levick (1991)
p_c [mmHg]	20	Levick (1991)
p_o [mmHg]	-1	Levick (1991)
α	1.1	
σ_G	0.9	Michel and Phillips (1987)
σ_W	0.1	Hu and Weinbaum (1999)
ℓ_p^G [$\mu\text{m}^2\text{sec}^{-1}\text{mmHg}^{-1}$]	0.601854	Speziale et al. (2008)
ℓ_p^W [$\mu\text{m}^2\text{sec}^{-1}\text{mmHg}^{-1}$]	4.15203	Speziale et al. (2008)
ℓ_d^G [$\mu\text{m}^2\text{sec}^{-1}\text{mmHg}^{-1}$]	0.536252	
ℓ_d^W [$\mu\text{m}^2\text{sec}^{-1}\text{mmHg}^{-1}$]	3.69946	

Table 3.1: Typical values of material properties of a micro-vessel: σ is the reflection coefficient, ℓ_p is the hydraulic conductivity, ℓ_d is the diffusional permeability. The coefficient α depends on a Péclet number and is defined such as to respect condition (3.46). The superscripts G and W indicate glycocalyx and endothelial layers, respectively.

In order to respect the condition (3.46) everywhere within the computa-

tional domain, including the transition zone, we choose ℓ_d as follows:

$$\ell_d(r) := \alpha \left[\max_{r_c < r < r_o} \sigma(r) \right]^2 \ell_p(r), \quad (3.47)$$

where $\alpha > 1$ is a constant, which ensures that condition (3.46) is respected everywhere.

3.2 Numerical approximation

The analytical solutions described in the Section 3.1.5 are valid for a two-layered model with discontinuous properties at the interface between glyco-calyx and endothelial cells. However, the case of smooth transition between the two layers cannot be solved analytically, for which it is necessary to resort to numerical solutions. In this section we describe numerical methods and we assess convergence properties, accuracy and efficiency for the case of a vessel composed of two homogeneous layers with different material properties.

3.2.1 Description of numerical schemes

Among the possible numerical schemes, which can be used to solve the *Boundary Value Problem* (BVP) (3.8)-(3.10), in the present chapter we consider a classical *Finite Difference* (FD) *scheme* and a Runge-Kutta *shooting scheme*. The domain $[0, 1]$ is discretised by a regular mesh $r_i = ih$, for $i = 0 \dots N + 1$, where $h = 1/(N + 1)$ is the mesh spacing. The grid is designed in such a way that the interface point r_g lies between two adjacent grid points. The unknowns are the functions $p(r)$ and $\Pi(r)$, for which we seek approximations $p_i \approx p(r_i)$ and $\Pi_i \approx \Pi(r_i)$.

Following Freeze (1975), the diffusion terms of equations (3.8) are approximated as follows:

$$\frac{d}{dr} \left[\mathcal{K}(r) \frac{df}{dr} \right]_{r=r_i} \approx \frac{1}{h} \left(\frac{\mathcal{K}_i + \mathcal{K}_{i+1}}{2} \frac{f_{i+1} - f_i}{h} - \frac{\mathcal{K}_{i-1} + \mathcal{K}_i}{2} \frac{f_i - f_{i-1}}{h} \right), \quad (3.48)$$

where $\mathcal{K}(r)$ is substituted with functions $\mathcal{F}(r)$, $\mathcal{G}(r)$, $\mathcal{H}(r)$ or $\mathcal{L}(r)$, in the respective diffusion terms in equations (3.8). The application of this numerical scheme (indicated hereafter as *Freeze's scheme*) leads, after imposing the following boundary conditions:

$$p_0 = p_c, \quad p_{N+1} = p_o, \quad \Pi_0 = \Pi_c, \quad \Pi_{N+1} = \Pi_o, \quad (3.49)$$

to a sparse non-linear algebraic system of $2N$ equations in $2N$ unknowns, which can be solved by using a Newton method.

The second strategy makes use of the shooting method, which is based on converting the BVP (3.8)-(3.10) to an *initial value problem* for the following

augmented system in the unknowns $y_1(r) = \Pi(r)$, $y_2(r) = \Pi'(r)$, $y_3(r) = p(r)$, $y_4(r) = p'(r)$:

$$\begin{cases} y_1' = y_2, \\ y_2' = -\frac{1}{\mathcal{F}\mathcal{L} - \mathcal{G}\mathcal{H}} \left[(\mathcal{F}\mathcal{H}' - \mathcal{F}'\mathcal{H}) y_4 + (\mathcal{F}\mathcal{L}' - \mathcal{G}'\mathcal{H}) y_2 + \mathcal{F}(\mathcal{H}y_4 + \mathcal{L}y_2) \frac{y_2}{y_1} \right], \\ y_3' = y_4, \\ y_4' = \frac{1}{\mathcal{F}\mathcal{L} - \mathcal{G}\mathcal{H}} \left[(\mathcal{G}\mathcal{H}' - \mathcal{F}'\mathcal{L}) y_4 + (\mathcal{G}\mathcal{L}' - \mathcal{G}'\mathcal{L}) y_2 + \mathcal{G}(\mathcal{H}y_4 + \mathcal{L}y_2) \frac{y_2}{y_1} \right], \end{cases} \quad (3.50)$$

with the following initial conditions:

$$p(0) = p_c, \quad p'(0) = dp_c, \quad \Pi(0) = \Pi_c, \quad \Pi'(0) = d\Pi_c. \quad (3.51)$$

Initial value problem (3.50)-(3.51) is solved many times by using *Runge-Kutta schemes* from the first (RK1) to the fourth (RK4) orders, until convergence is achieved (Hildebrand, 1987).

The initial conditions are changed according to the boundary conditions at $r = 1$ and the procedure is stopped when the boundary values p_{N+1} and Π_{N+1} converge to p_o and Π_o , respectively. Given the initial slopes $(d\Pi_c^{(k-1)}, dp_c^{(k-1)})$ and $(d\Pi_c^{(k)}, dp_c^{(k)})$, the initial conditions are updated according to the following linear interpolation scheme:

$$\begin{cases} d\Pi_c^{(k+1)} = d\Pi_c^{(k)} + \frac{d\Pi_c^{(k)} - d\Pi_c^{(k-1)}}{\Pi_{N+1}^{(k)} - \Pi_{N+1}^{(k-1)}} (\Pi_o - \Pi_{N+1}^{(k)}), \\ dp_c^{(k+1)} = dp_c^{(k)} + \frac{dp_c^{(k)} - dp_c^{(k-1)}}{p_{N+1}^{(k)} - p_{N+1}^{(k-1)}} (p_o - p_{N+1}^{(k)}), \end{cases} \quad (3.52)$$

until $\|\Pi_o - \Pi_{N+1}^{(k)}, p_o - p_{N+1}^{(k)}\|_2$ is smaller than a given tolerance, where $\Pi_{N+1}^{(k)}$ and $p_{N+1}^{(k)}$ are the numerical solutions at the boundary $r = 1$ obtained by solving the initial value problem with the initial conditions at the stage k .

For the first two stages we used

$$\begin{cases} d\Pi_c^{(0)} = \Pi_o - \Pi_c, & \begin{cases} d\Pi_c^{(1)} = \alpha_1 d\Pi_c^{(0)}, \\ dp_c^{(1)} = \alpha_2 dp_c^{(0)}, \end{cases} \end{cases} \quad (3.53)$$

with $\alpha_1 = 2$ and $\alpha_2 = 0.5$. Next, we assess the two numerical schemes just presented.

3.2.2 Assessment of the computational methods

Grid independence. We consider a sequence of meshes $\{M_k\}$, $k = 0, 1, \dots, K$ such that the mesh size of M_l is reduced by a factor of 2 relative to that of mesh M_{l-1} . The number of mesh points for M_0 is $N_0 = N + 2 \geq 3$, where

N is a positive integer; this is actually the number of internal points in the initial mesh. The mesh M_k has $N_k = 2^k(N_0 - 1) + 1$ points, where $N_0 = 199$. The mesh size for M_k is

$$h_k = \frac{h_0}{2^k} = \frac{1}{N_k - 1} = \frac{1}{2^k(N_0 - 1)}. \quad (3.54)$$

Let us denote by

$$(\Pi, p)_k := (\Pi_0, \dots, \Pi_{N+1}, p_0, \dots, p_{N+1}) \quad (3.55)$$

the solution vector for mesh M_k of N_k points and by

$$\Delta_k := \|(\Pi, p)_k - (\Pi, p)_{k-1}\|_2 \quad (3.56)$$

the difference between the solution vectors $(\Pi, p)_k$ and $(\Pi, p)_{k-1}$ corresponding to meshes M_k and M_{k-1} , computed from their common nodes, using the L_2 -norm normalised by the mesh spacing h_k . Figure 3.3 shows Δ_k for the shooting method with Runge-Kutta from the first (RK1) to the fourth (RK4) orders and for the Freeze's scheme. We remark that the shooting method with RK4, as expected, is faster in achieving grid independence, with a tolerance of 10^{-10} .

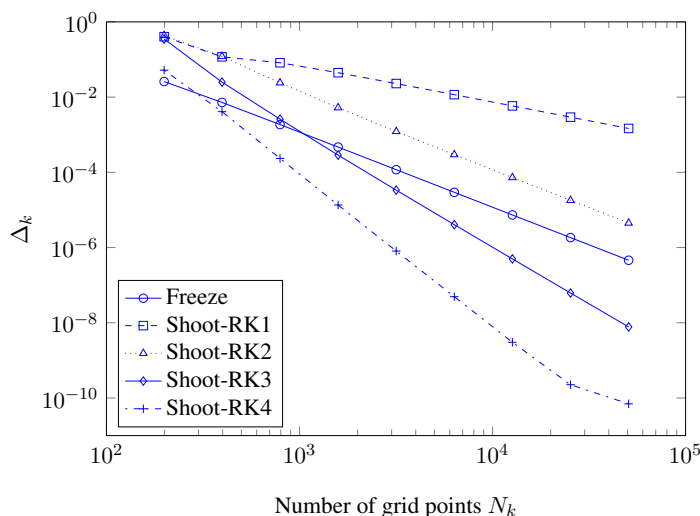


Figure 3.3: L_2 -norm $\Delta_k = \|(\Pi, p)_k - (\Pi, p)_{k-1}\|_2$ as function of grid points, for Freeze's finite difference method and Runge-Kutta shooting methods of orders 1 to 4.

We therefore choose the solution computed with the shooting scheme, with the fourth order Runge-Kutta method, with $N_8 = 50689$ points, as the reference solution $(\hat{\Pi}, \hat{p})$ for the convergence study to be reported next.

Convergence. Here we carry out an empirical convergence rate study using $(\hat{\Pi}, \hat{p})$ as the reference solution, in which numerical solutions were computed for nine meshes. Errors

$$E_k := \|(\Pi, p)_k - (\hat{\Pi}, \hat{p})\|_2 \quad (3.57)$$

were measured with the L_2 -norm, normalised by the mesh spacing h_k ; these are plotted in Figure 3.4.

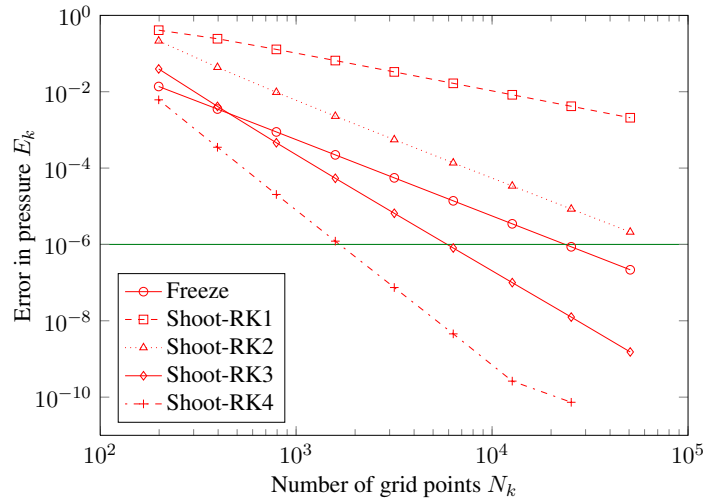


Figure 3.4: Error $E_k = \|(\Pi, p)_k - (\hat{\Pi}, \hat{p})\|_2$ as function of grid points, for Freeze's finite difference method and Runge-Kutta shooting methods of orders 1 to 4.

As expected, the error for all methods decreases as the mesh is refined, but for higher order methods the error decreases faster. For sufficiently fine meshes the error of the higher order methods is smaller than that of the lower order methods. Note that RK2 and Freeze, being both of second order of accuracy, have the same slope, but the latter has a smaller error. In Figure 3.4 we also note that given a fixed error of 10^{-6} (see solid line), this error is attained by Freeze's scheme with a mesh of $N_7 = 25345$ points; for the shooting schemes with RK3 and RK4 this is attained with $N_5 = 6337$ and $N_3 = 1585$ points, respectively. For large errors, for example, larger than 10^{-2} , Freeze's scheme attains that error on a coarser mesh, as compared to some of the other schemes.

Efficiency. By *efficiency* we mean this. Given a fixed error, what is the scheme that attains that error at the lowest computational cost? Figure 3.5 shows error against CPU time, for all five schemes. Obviously, CPU time increases by both refining the mesh and augmenting the order of accuracy of the schemes. In general, however, from an efficiency point of view, it is

more convenient to increase the order of accuracy of a scheme than to refine the mesh, to compute solutions more accurately. For sufficiently large errors, or inaccurate solutions, it is not always clear as to what is best, refine the mesh or increase the accuracy. For example, Freeze's scheme requires a lower computational time than any of the shooting schemes when the chosen error is sufficiently large.

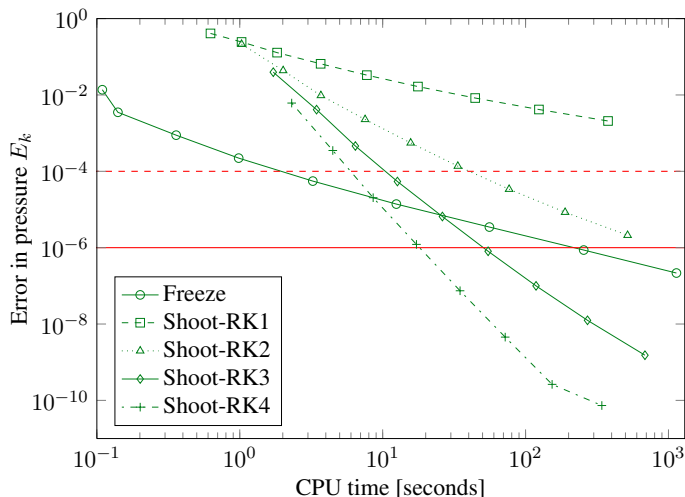


Figure 3.5: Error $E_k = \|(\Pi, p)_k - (\hat{\Pi}, \hat{p})\|_2$ as function of CPU time, for Freeze's finite difference method and Runge-Kutta shooting methods of orders 1 to 4.

For example, for an error of 10^{-4} , horizontal dashed line in Figure 3.5, Freeze's scheme is more efficient than a shooting method. However, for an error of 10^{-6} , a shooting scheme with a high-order Runge-Kutta method is more efficient than Freeze's scheme, see horizontal solid line in Figure 3.5; this error is attained in about 17 seconds by the shooting method with RK4, in around 55 seconds with RK3 and in about 255 seconds by Freeze's method. The fourth-order shooting method is 15 times more efficient than the second-order Freeze's scheme.

Improved shooting scheme. The previously described shooting scheme used linear interpolation (3.52) to find an iterate to approximate the prescribed boundary value at $r = 1$. The implementation simply used the last two iterates to perform the linear interpolation. It is possible to improve this scheme by (i) selecting the last iterate as one of the points and (ii) selecting the other point as the one associated with the smallest error, amongst the two previous iterates. This strategy reduces the number of iterations in the shooting method to about one half, resulting in a reduction of the computing time by about one half. For example, with the new algorithm, an error of 10^{-6}

is attained in about 8.6 seconds by the shooting method with RK4, whereas this time is 27 seconds with RK3. Now the fourth-order shooting method is about 30 times more efficient than the second-order Freeze's scheme.

3.3 Results

3.3.1 Validation of the numerical scheme

In view of its applicability to the case of smooth transition of membrane properties at the interface between glycocalyx and endothelial cells, we compare the numerical solution obtained from Freeze's method with the analytical solution for discontinuous membrane properties discussed in Section 3.1.5. Preliminary simulations showed that a satisfying agreement between numerical and analytical solutions for osmotic and hydrostatic pressures can be obtained with only 25 grid nodes. However, in order to obtain a good agreement also for the fluxes, the number of nodes should be increased significantly. Figure 3.6 shows the following relative differences: $\Delta J_i = |(J_i^{N_k} - J_i)/J_i|$, $i = v, s$, where $J_i^{N_k}$ is volumetric flux (for $i = v$) or solute mass flux (for $i = s$) computed numerically with N_k grid nodes and J_i is the corresponding flux obtained with the analytical solution, i.e. $J_v = -2\pi k_1$ and $J_s = 2\pi k_2$, respectively. The relative differences of the two fluxes decline oscillating around at what appears to be a common power law function of the number of grid nodes (notice the log-log scale used in Figure 3.6). For $N_k = 18433$, the relative difference is smaller than 10^{-4} and 10^{-6} for the volumetric and the solute mass fluxes, respectively. Therefore, in the following, if not explicitly stated, the numerical simulations are performed with Freeze's scheme by using $N_k = 18433$ grid nodes, which ensures good accuracy at a reasonable computational cost.

Figure 3.7 compares hydrostatic and osmotic pressures across micro-vessel wall, obtained by solving numerically equations (3.8) with the analytical solutions (3.17) and (3.18), respectively. The difference between analytical and numerical solutions is negligible with an error equal to $7.12 \cdot 10^{-4}$ and $7.15 \cdot 10^{-4}$ for the osmotic and hydrostatic pressures, respectively.

3.3.2 Comparison between the two- and single-layered models

In most applications the micro-vessel is considered homogeneous, under the assumption that homogeneous equivalent properties can be obtained mimicking the combined effect of glycocalyx and endothelial cells. *Equivalent parameters* can be defined as the parameters that when used into the solutions for a homogeneous medium lead to the same volumetric and solute

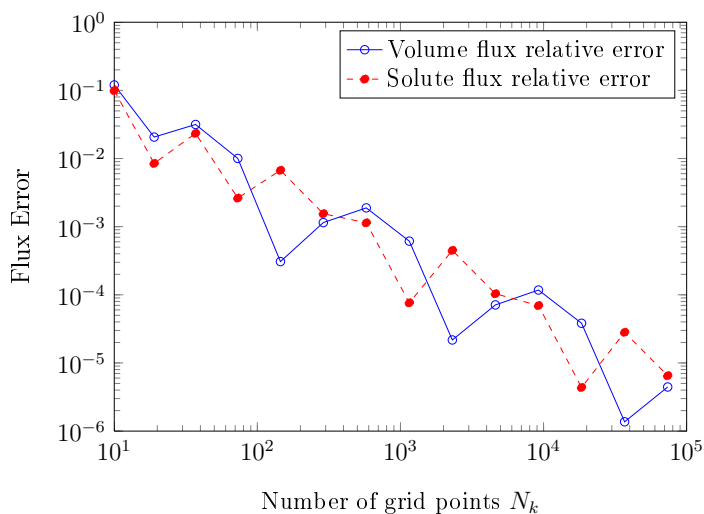


Figure 3.6: Relative differences between numerical and analytical solutions of volumetric and solute mass fluxes, as a function of the number of grid points.

fluxes of the heterogeneous (two-layered) medium. However, given the non-linearity of the governing equations (3.8) equivalent parameters valid for any choice of boundary conditions cannot be defined, since they depend of the structure of the governing equations and the boundary conditions as well (Milton, 2002). Exploring this issue in depth would require a detailed analysis, which is beyond the objectives of the present chapter, we therefore limit ourselves to compute equivalent parameters for boundary conditions and medium properties of the base case reported in Table 3.1.

Equivalent parameters to be used in the analytical solutions for a single homogeneous layer can be obtained by imposing that the fluxes are conserved, i.e. by imposing the following conditions:

$$k_1^H = k_1, \quad k_2^H = k_2, \quad (3.58)$$

where the superscript H indicates that the flux is evaluated with the single-layered model, while k_1 and k_2 are the fluxes of the heterogeneous two-layered model. All the fluxes, that in equations (3.58) are divided by $\mp 2\pi$, are obtained as described in Section 3.1.5 with the parameters and the boundary conditions showed in Table 3.1. Since the equivalent parameters to be defined are three (ℓ_p^{eq} , ℓ_d^{eq} , σ^{eq}), while the conditions imposed by equations (3.58) are two, we set the equivalent reflection coefficient by using the following expression suggested by Sugihara-Seki and Fu (2005):

$$\sigma^{eq} = \frac{\ell_d^G \ell_d^W}{\ell_d^G + \ell_d^W} \left(\frac{\sigma_G}{\ell_d^G} + \frac{\sigma_W}{\ell_d^W} \right), \quad (3.59)$$

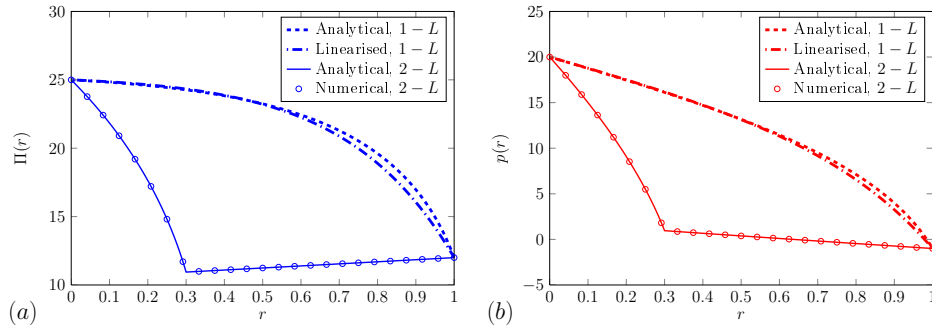


Figure 3.7: Comparison between the numerical solution of osmotic (a) and hydrostatic (b) pressures for the two-layered case, obtained with the Freeze’s scheme by using 18433 grid nodes (Numerical, $2-L$), and the corresponding analytical solutions (Analytical, $2-L$). The single layer analytical solutions (Analytical, $1-L$) are also shown together with the linearised analytical solutions (Linearised, $1-L$) presented in Section 3.1.6. In all cases $\varepsilon^2 = 0$ and for ease of representation the numerical solution is shown only at a few grid points. The properties of the two layers are reported in Table 3.1 together with Dirichlet boundary conditions at the lumen and interstitial sides of micro-vessel wall.

which for the medium properties shown in Table 3.1 assumes the following value: $\sigma^{eq} = 0.7987$. With this value of σ^{eq} the two equations (3.58) can be solved obtaining $\ell_p^{eq} = 0.7795$, $\ell_d^{eq} = 0.5210$, which substituted into equations (3.17) and (3.18) provide the behaviour of the osmotic and hydrostatic pressures, respectively, for the equivalent homogeneous single-layered medium.

The analytical solution of the osmotic pressures is shown in Figure 3.7a. Osmotic pressure declines rapidly across glycocalyx, reaches a minimum at the interface with endothelial cells and then it increases again to the value imposed as boundary condition at the external surface of micro-vessel. This behaviour, and in particular the minimum of osmotic pressure at the external surface of glycocalyx, is in agreement with a recent reinterpretation of Starling’s law proposed independently by Michel (1997) and Weinbaum (1998), which provides an improved interpretation of the classic experiments conducted by Landis (1927); see also Levick and Michel (2010) for a complete review. Dilution in the clefts just outside glycocalyx is an important physiological mechanism, which has been indicated by Michel (1997) and Weinbaum (1998) as the cause preventing reversal steady-state flow (absorption) when capillary hydrostatic pressure was lowered to 10 – 15 cm H₂O (7.35 – 11.03 mmHg) in Landis’ experiment. A similar behaviour is shown in Figure 3.7b for hydrostatic pressure with a strong reduction across glycocalyx followed by a mild reduction across endothelial cells. Hydrostatic

pressure is not differentiable at the interface between the two layers, which is due to the discontinuity in medium properties, but pressure gradient does not reverse across endothelial cells, as for osmotic pressure. The important result shown in Figures 3.7a and 3.7b is that most of the pressures drop between lumen and interstitium occurs in the glycocalyx, confirming the importance of this hydrated gel in controlling flow and solute mass exchange (see e.g. Levick, 2010).

A striking difference can be observed in Figures 3.7a and 3.7b between the single- and two-layered models, with the latter showing a smooth but steep decline of both hydrostatic and osmotic pressures within glycocalyx. This is due to the strong sieving effect that glycocalyx exerts on macromolecules, such that only a very small fraction of them reached the clefts. In the two-layered model this effect is reproduced by using a large reflection coefficient. Notice that, due to the larger aperture of the clefts, macromolecules move with small to negligible hindrance, as soon as they have crossed glycocalyx. In the membrane model adopted in this work the almost free movement of macromolecules in the clefts is represented by adopting a small reflection coefficient ($\sigma = 0.1$). Because of the high selectivity of glycocalyx, concentration of macromolecules is small at the interface between glycocalyx and endothelial cells, resulting in an osmotic pressure smaller than in the interstitium. This feeds back to hydrostatic pressure, which also shows a strong decline within glycocalyx, as discussed above. This behaviour, which is consistent with the observation that flow cannot be reversed by simply reducing hydrostatic pressure in the lumen as discussed by Levick and Mortimer (1999) and Levick and Michel (2010), is not captured by the single-layered model, which instead predicts much higher pressures at the interface between glycocalyx and endothelial cells and a gradual decline of both pressures across micro-vessel wall, with a gradient that increases with the distance to account for the progressive increase of the surface crossed by the flows.

An important consequence of this different behaviour of the pressures is that the single-layered model is unable to capture the effect on volumetric and solute mass fluxes of glycocalyx deterioration, which being located in the lumen side of micro-vessel is more prone to be damaged, than endothelial cells.

Figures 3.8a and 3.8b show the distribution of osmotic and hydrostatic pressures, respectively, across micro-vessel wall for the following three values of the parameter controlling property variations at the interface: $\varepsilon^2 = 0, 10^{-4}, 10^{-3}$. The solution for the discontinuous transition, i.e. for $\varepsilon^2 = 0$ is the analytical solution discussed in Section 3.1.5, while for $\varepsilon^2 > 0$ the solutions are numerical and obtained with Freeze's scheme by using 18433 grid nodes. A smooth, yet sharp, transition in material properties eliminates the discontinuity in the first derivative of the pressures at the interface between the two layers; contemporaneously, pressures within the glycocalyx are

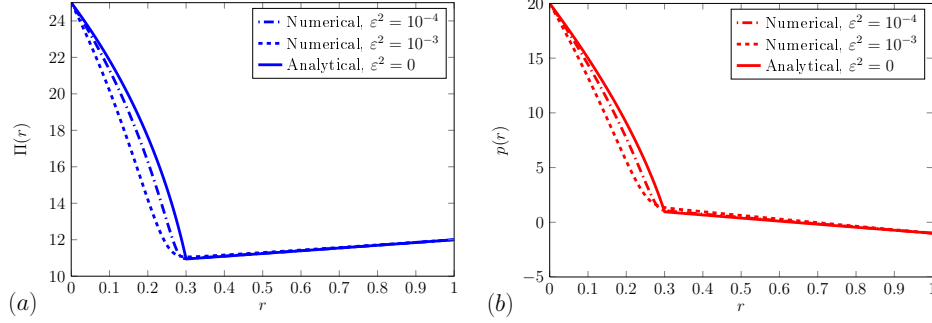


Figure 3.8: Osmotic (a) and hydrostatic (b) pressures across micro-vessel wall for $\varepsilon^2 = 0, 10^{-4}, 10^{-3}$. The case $\varepsilon = 0$ is obtained by means of the analytical solutions, while the cases with $\varepsilon^2 = 10^{-4}, 10^{-3}$ are obtained numerically with Freeze's scheme by using 18433 grid nodes.

steeper and with a smaller curvature than in the discontinuous case. The pressures at the position where the interface is located in the discontinuous case show negligible variations such as the distribution of the pressures within endothelial cells. The progressive increase of the gradients of hydrostatic and osmotic pressures within glycocalyx occurring when ε^2 increases, which is accompanied by the reduction of the reflection coefficient close to the interface, leads to an increase of both volume and solute mass fluxes (see Table 3.2). The relative increase of J_v is negligible (0.2%) for $\varepsilon^2 = 10^{-4}$, but it increases rapidly with ε , reaching 16% for $\varepsilon^2 = 10^{-3}$. J_s is more sensitive to variations of ε^2 , with an increase of 9.9% and 41.8% for $\varepsilon^2 = 10^{-4}$ and 10^{-3} , respectively, with respect to the solute mass flux obtained with a sharp transition ($\varepsilon^2 = 0$) of material properties.

Description	J_v	J_s
Analytical $\varepsilon^2 = 0$	545.586	2802.45
Numerical $\varepsilon^2 = 0$	545.607	2802.46
Numerical $\varepsilon^2 = 10^{-4}$	572.354	3110.18
Numerical $\varepsilon^2 = 10^{-3}$	634.809	3945.78

Table 3.2: Volumetric and solute mass fluxes for the following values of ε^2 , the parameter controlling the smoothness of properties transition between the two layers: $\varepsilon^2 = 0, 10^{-4}, 10^{-3}$.

Figures 3.9a and 3.9b show the effect of changes in blood osmotic pressure (at the lumen side) on the behaviour of osmotic and hydrostatic pressures, respectively. A variation of luminal osmotic pressure, with respect to the reference value of $\Pi_c = 25$ mmHg shown in Table 3.1, causes a variation of the same sign, but smaller, in the osmotic pressure at the interface be-

tween the two layers. An opposite behaviour is observed for the hydrostatic pressure at the interface, which as shown in Figure 3.9b reduces as luminal osmotic pressure increases. Interestingly, the change in the osmotic pressure drop across micro-vessel wall feeds back to hydrostatic pressure distribution through the coupling with the non-linear transport equation.

This effect cannot be reproduced with linearised models decoupling flow and transport processes, such as that presented by Speziale et al. (2008).

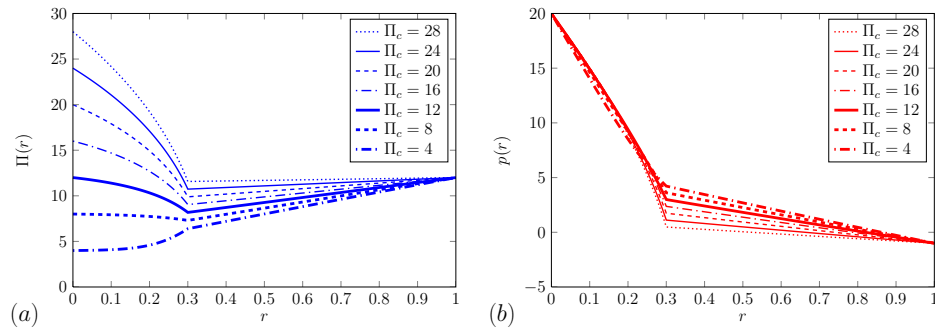


Figure 3.9: Behaviour of osmotic and hydrostatic pressures across micro-vessel wall for several values of the osmotic pressure Π_c in the lumen.

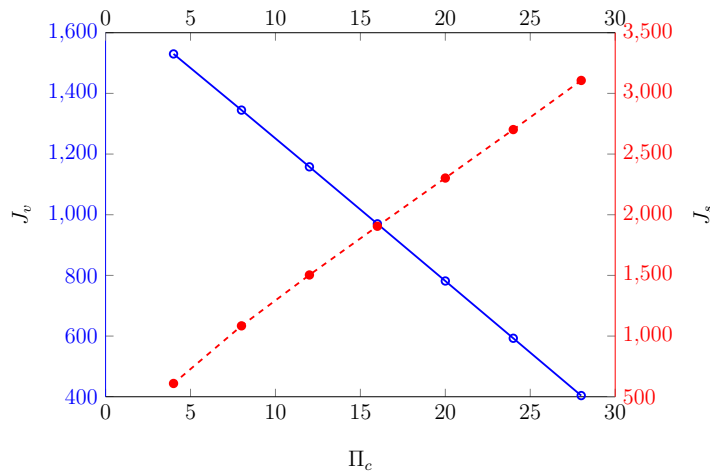


Figure 3.10: Volumetric and solute mass fluxes, relative to the reference case with boundary conditions and material properties as shown in Table 3.1, as a function of blood osmotic pressure Π_c within the lumen.

The impact of osmotic pressure variations in the lumen is shown in Figure 3.10. The most relevant information contained in the figure lies in the opposite behaviour of the two fluxes; an increase of luminal osmotic pressure with respect to the reference case, with all the other quantities remaining

the same, leads to a reduction of volumetric flux and a contemporaneous increase in solute mass flux. The opposite occurs, when Π_c is reduced below the reference case: volumetric flux increases, while solute mass flux reduces, as an effect of the reduction in the osmotic pressure drop across micro-vessel wall.

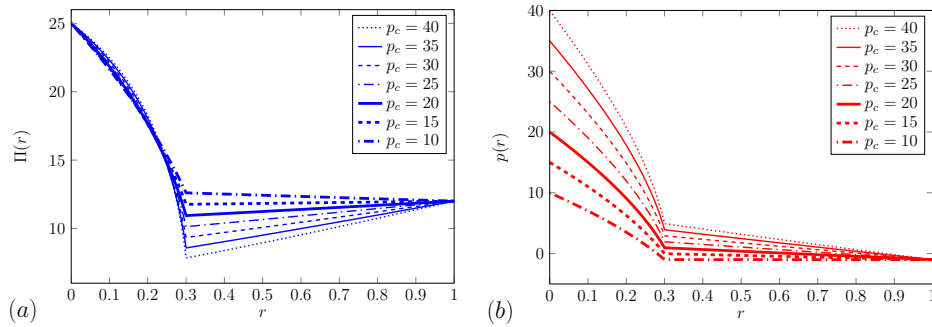


Figure 3.11: Behaviour of osmotic (a) and hydrostatic (b) pressures across micro-vessel wall for several values of blood hydrostatic pressure p_c within the lumen.

Figures 3.11a and 3.11b show the behaviour of osmotic and hydrostatic pressures across micro-vessel wall for several values of blood hydrostatic pressure p_c within the lumen. The reduction of osmotic pressure at the interface between the two layers, with respect to the interstitial value, becomes progressively smaller as the hydrostatic pressure within the lumen reduces, and it vanishes at $p_c \simeq 15$. For smaller values of p_c , osmotic pressure at the interface between the two layers remains higher than external osmotic pressure. At the interface, hydrostatic pressure is higher for higher luminal hydrostatic pressures, but to a lesser extent with respect to the increase in the lumen. This leads to a higher pressure drop for higher luminal hydrostatic pressures. A similar behaviour is shown by osmotic pressure, but with a smaller variations in pressure drop, due to the fact that the osmotic pressure at the lumen does not change.

As shown in Figure 3.12, both fluxes increase with the hydrostatic pressure at the lumen. However, volumetric flux reduces to zero as luminal hydrostatic pressure reduces to 10 mmHg. This result is consistent with the experiments of Landis (1932) showing no volumetric flux inversion at steady state at pressures as low as 20 cm H₂O (14.7 mmHg), which had been considered the basis for revisiting Starling's law (Michel, 1997; Weinbaum, 1998).

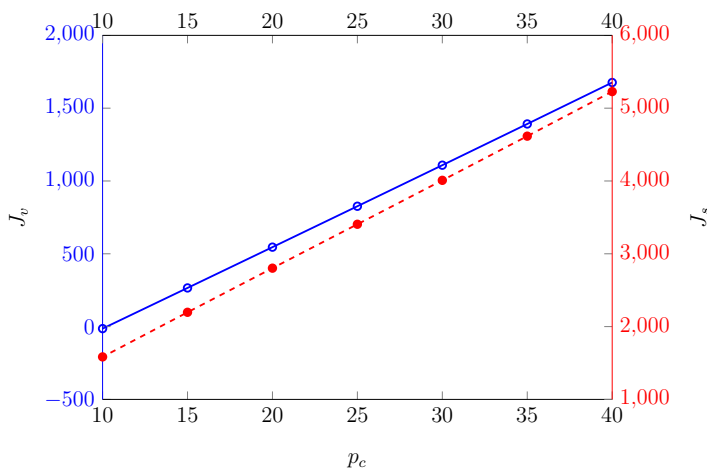


Figure 3.12: Volumetric and solute mass fluxes, with boundary conditions and material properties as shown in Table 3.1, as a function of the blood hydrostatic pressure p_c within the lumen.

3.4 Conclusions

We have presented and discussed a new model of flow and transport of macromolecules (proteins) across the composite wall of a micro-vessel. The micro-vessel has been represented as a two-layered hollow cylinder. The inner layer has represented the glycocalyx, an hydrated membrane exerting a remarkable sieving effect on macromolecules, and the external layer representing endothelial cells, which are folded and connected along clefts spiralling in an irregular manner along longitudinal micro-vessel axis. The clefts are partially closed by tight junctions. We represent this composite medium as two membranes of different thickness and properties. Flow and non-linear transport equations are coupled through osmotic pressure, which is assumed proportional to the concentration of macromolecules in blood plasma. We have shown that, by assuming radial symmetry, this model can be solved analytically for the general case of n -layers. The solution is consistent with the mechanistic revisitation of the classical Starling's law proposed independently by Michel (1997) and Weinbaum (1998). In particular, it well represents the dilution occurring in cleft space at the external surface of glycocalyx, with the corresponding reduction of osmotic pressure to values smaller than in external tissues, which is in line with recent observations (Adamson et al., 2004) and claimed as the main mechanism preventing flow inversion at low hydrostatic pressures. Our model differs from other published models in several aspects. Differently from Speziale et al. (2008), we solve the full system of coupled differential equations for flow and transport without linearising the transport equation in a n -layer setup, which

allows us to handle specialised microvessels. For simplicity, the application was limited to a two-layered microvessel, which is the most common type of microvessel in humans and other mammals. However, the extension to four layers, typical of brain microvessels, can be obtained at the cost of a more complicated structure of the solution, due to the need to impose conservation of hydrostatic and osmotic pressures across three interfaces, while conservation of volumetric and mass fluxes are obtained by imposing that the coefficients k_1 and k_2 are the same in the three layers. The application of the model to an homogenised micro-vessel, representing the combined effect of glycocalyx and endothelial cells with a single layer membrane characterised by somewhat equivalent properties, as suggested by Speziale et al. (2008) for example, has evidenced a strikingly different distribution of the pressures within micro-vessel wall, which are significantly higher than those of the two-layered model, in particular at the interface between the two layers. A better match may be obtained if boundary conditions are applied to the external surface of glycocalyx, thereby neglecting the effect of endothelial cells and the dilution occurring in the cleft at the contact with the external surface of glycocalyx, which has been indicated as an important physiological mechanism controlling volumetric flux (see e.g. Levick and Michel, 2010).

To summarise, our solution of the n -layer model of micro-vessel has a level of complexity comparable to existing homogenised single-layered models (Speziale et al., 2008), but showed to be much more accurate in describing the combined effect of glycocalyx and endothelial cells, including the dilution occurring in the cleft at the contact with the external surface of glycocalyx, on controlling volumetric flow and solute mass transport across micro-vessel wall. Our model is computationally much more effective than micro-scale approaches, such as that proposed by Sugihara-Seki et al. (2008); with a moderate effort it can be implemented into large-scale models representing blood circulation in human body. This is an important feature that full micro-scale models, resorting to sophisticated numerical methods and requiring parallel computing, cannot enjoy. In addition, the better reproduction of hydrostatic pressure across micro-vessel wall, with respect to the homogeneous single-layered model, makes this approach appealing for applications dealing with the mechanical response of the micro-vessel to changes of internal hydrostatic pressure.

Chapter 4

Effects of glycocalyx damage and hypertension on transport processes

The content of this Chapter is taken from Facchini et al. (2013a).

As we have already seen in Chapter 1, capillary wall is composed by a one-cell-thick layer of endothelial cells, internally coated by the surface glycocalyx, currently recognised as crucial for micro-vascular wall homeostasis. Measurements of glycocalyx thickness vary between 150 and 400 nm, although these may be under-estimations due to the dehydrating effect of electron microscopy fixation and processing (Weinbaum et al., 2007). The fibre matrix of glycocalyx is recently described by Squire et al. (2001) as a quasi-periodic 3D fibrous mesh work with a characteristic spacing of 20 nm and with anchoring foci (thought to form an hexagonal array) emanating from the underlying cortical cytoskeleton. See for instance Figure 5 of Arkill et al. (2012), in which the glycocalyx structure is reconstructed using electron tomography.

A pathological loss or agonist-induced thinning of glycocalyx may produce an impaired vascular wall protection throughout the circulatory system (VanTeeffelen et al., 2007). In particular, experimental studies in which the glycocalyx was treated with glycosaminoglycan-degrading enzymes show that enzymatic degradation results in (a) a reduction of anionic dextran exclusion (Henry and Duling, 1999), (b) the formation of perivascular oedema (van den Berg et al., 2003), (c) an impairment of shear stress-dependent *NO* production in arteries and cultured endothelial cells (Florian et al., 2003; Mochizuki et al., 2003), (d) an increase in hydraulic conductivity (Adamson, 1990), in protein permeability (Huxley and Williams, 2000), in albumin glomerular clearance (Jeansson and Haraldsson, 2003) and in adhesion of platelets and leukocytes in venules (Constantinescu et al., 2003).

Moreover, degradation and/or loss of glycocalyx have been shown during exposure to atherogenic/cardiovascular risk factors, including inflammatory and atherogenic stimuli, ischemia/reperfusion and oxidized low-density lipoprotein infusion (VanTeeffelen et al., 2007).

Patients with type 1 diabetes mellitus and microalbuminuria were demonstrated to be more susceptible to glycocalyx degradation compared to their normalbuminuric counterparts (Nieuwdorp et al., 2006). Glycocalyx disruption occurs also in clinical conditions such as chronic renal failure, cerebrovascular disease and sepsis (Martens et al., 2013; Nieuwdorp et al., 2007; Vlahu et al., 2012; Marechal et al., 2008; Donati et al., 2013) and on high-fat high-cholesterol diet (van den Berg et al., 2006). Moreover, this loss of systemic glycocalyx volume, leading to fluid leakage outside microvessels, correlates to a reduction in anatomic capillary diameter and/or functional capillary density (VanTeeffelen et al., 2007; Constantinescu et al., 2011).

Glycocalyx degeneration, induced by reactive oxygen species exposure, is shown to lead to endothelial dysfunction, with the possible onset of *microalbuminuria* or *proteinuria* (i.e. the presence of an excess of albumin or other serum proteins, respectively, in the urine) in clinical disease (Singh et al., 2007, 2013).

Finally, shear stress appears to contribute both to the incorporation of the glycosaminoglycan hyaluronan into the glycocalyx, thus affecting sulfated glycosaminoglycan distribution, and to the shedding of hyaluronan (for instance, during reperfusion after ischemia), thus permitting leukocyte adherence to vessel wall (VanTeeffelen et al., 2007). Shear stress seems to be mediated by *NO* production (Mochizuki et al., 2003) and *G* proteins (Mulivor and Lipowsky, 2004).

On the other hand, *hypertension* is a chronic medical condition in which arterial blood pressure is high, forcing the heart to work harder than normal to pump blood. Systolic blood pressure higher than 115 mmHg is responsible for 62% of cerebrovascular disease (including stroke, myocardial infarction, heart failure, aneurysms of the arteries, coronary heart disease and peripheral arterial disease) and 49% of ischemic heart disease. Also the concordance of hypertension and diabetes is pernicious; moreover, loss of renal function (as for chronic kidney disease) is proportional to blood pressure level. Hypertension plays a role in trans-vascular exchange, increasing both fluid filtration and protein extravasation. This leads in most severe cases to leakages as in the cases of extra-vascular oedema and hemorrhages, observed for instance in hypertensive retinopathy and hypertensive optic neuropathy (Chobanian et al., 2003).

A series of *1D* (e.g. Curry and Michel, 1980; Tsay and Weinbaum, 1991; Weinbaum et al., 1992) and *3D* (e.g. Bundgaard, 1984; Ward et al., 1988; Tsay and Weinbaum, 1991; Weinbaum et al., 1992; Fu et al., 1994) mathematical models has been developed since 1950s, showing that permeabilities to water and hydrophilic solutes in microvessels of different tissues can be ac-

counted for by inter-endothelial cleft pathways with surface glycocalyx layer and junction strands with discontinuous leakages (see the reviews of Michel and Curry, 1999; Sugihara-Seki and Fu, 2005).

Squire et al. (2001) even proposed a quasi-periodic $3D$ ultra-structural model of the endothelial surface layer, which was subsequently used in Weinbaum et al. (2003) to study in detail the flexural rigidity of the core proteins comprising the bush-like matrix and the adhesive molecular interactions between proteins in the endothelial membrane and circulating cellular components.

In order to incorporate charge effects on microvessel permeability, the model developed in Fu et al. (1994) was extended in Fu et al. (2003) by including a negatively charged glycocalyx layer at the entrance of inter-endothelial cleft and considering electrostatic and steric exclusions on charged solutes, at the interfaces of the glycocalyx layer between the vessel lumen, between the endothelial cleft and within the glycocalyx layer. Nevertheless, in the following we neglect the charge-sieving effect of glycocalyx, only considering its size-filtering capacity.

The effects of glycocalyx thinning and of a change in its morphology are also described in the work of Speziale and Sivaloganathan (2009), in which the glycocalyx enters into the mathematical model simply as in the boundary conditions.

The specific objective of the present chapter is to carry out a theoretical study of filtration and solute transport processes with the steady-state mathematical model described in Chapter 3, varying glycocalyx morphology and its physical properties, as much as blood pressure.

Our model differs from existing studies in the way the main anatomical microvessel structure is described, thereby allowing to explicitly compute the distribution of hydrostatic and osmotic pressure *inside* the vessel wall, without lumping glycocalyx layer into an algebraic relation. This results in a more precise and reasonable reconstruction of plasma filtration and solute leakage, also in the interface region between glycocalyx and endothelium.

In the present chapter we are considering a typical extra-cranial capillary, composed by only two layers: the glycocalyx and the endothelium.

4.1 The mathematical model

Assuming radial symmetry, we model steady-state plasma filtration and solute transport across blood vessel wall through the coupled non-linear ordinary differential equations presented in Chapter 3, written in cylindrical

coordinates (r, θ, z) and in dimensionless form as

$$\begin{cases} \frac{d}{dr} \left[(r + \xi) \ell_p \left(\frac{dp}{dr} - \sigma \frac{d\Pi}{dr} \right) \right] = 0, \\ \frac{d}{dr} \left[(r + \xi) \Pi \left(A \frac{dp}{dr} + B \frac{d\Pi}{dr} \right) \right] = 0, \end{cases} \quad (4.1)$$

in the hydrostatic $p = p(r)$ and the osmotic $\Pi = \Pi(r)$ pressures, for the dimensionless distance $r \in (0, 1)$ from vessel axis. The dimensionless quantities are defined as follows

$$\begin{aligned} p &= \frac{p^*}{p_R}, & \Pi &= \frac{\Pi^*}{p_R}, & \xi &= \frac{r_c}{r_o - r_c}, & r &= \frac{r^* - r_c}{r_o - r_c}, \\ \ell_p &= \frac{\ell_p^*}{\ell_p^H}, & \ell_d &= \frac{\ell_d^*}{\ell_p^H}, & A &= \frac{\ell_p^*(\sigma - 1)}{\ell_p^H}, & B &= \frac{\ell_p^*\sigma - \ell_d^*}{\ell_p^H}, \end{aligned} \quad (4.2)$$

where superscripts * denote dimensional quantities, r_o is the external radius of vessel wall and r_c is the internal radius of vessel wall identified with the internal surface of glycocalyx. Furthermore, ℓ_p^H is the harmonic mean for the dimensional hydraulic conductivity ℓ_p^* among the layers, weighted by each layer thickness, which for two layers is given by

$$\ell_p^H = \frac{r_o - r_c}{\frac{r_g - r_c}{\ell_p^G} + \frac{r_o - r_g}{\ell_p^W}}, \quad (4.3)$$

where ℓ_p^G refers to the glycocalyx layer (r_c, r_g) and ℓ_p^W to the endothelial cells composing the proper vessel wall (r_g, r_o) . σ is the membrane reflection coefficient and ℓ_d is the diffusional permeability. We choose as reference pressure p_R the magnitude of the external hydrostatic pressure $|p_o^*|$.

We solve system (4.1) in the hydrostatic $p = p(r)$ and the osmotic pressure $\Pi = \Pi(r)$, using the finite difference scheme proposed by Freeze (1975), and we recover the dimensionless volume $J_v = J_v(r)$ and solute $J_s = J_s(r)$ fluxes through

$$J_v = -2\pi(r + \xi) \ell_p \left(\frac{dp}{dr} - \sigma \frac{d\Pi}{dr} \right), \quad (4.4)$$

$$J_s = 2\pi(r + \xi) \Pi \left[\ell_p(\sigma - 1) \frac{dp}{dr} + (\ell_p\sigma - \ell_d) \frac{d\Pi}{dr} \right]. \quad (4.5)$$

Even if system (4.1) requires that both fluxes are constant in r , there is a small variation due to numerical approximations. We thus consider the flux as the mean of the spatial values in the previous expressions.

4.2 Relations between the physiological parameters

If we model the glycocalyx as a system of N cylindrical pores (per unit area of surface membrane) of mean radius r_p , we have the following relations

(Levick and Michel, 2010)

$$\sigma = (1 - \varphi)^2, \quad \text{with} \quad \varphi = \left(1 - \frac{r_s}{r_p}\right)^2, \quad (4.6)$$

$$\ell_p = \frac{N\pi r_p^4}{8\mu}, \quad (4.7)$$

$$\ell_d = \frac{N\pi r_p^2 D \varphi}{\Pi_M} f_p\left(\frac{r_s}{r_p}\right), \quad (4.8)$$

where $\sigma \in [0, 1]$ is the reflection coefficient, φ is the solute partition coefficient (that reduces diffusion in a narrow cylindrical pore, due to steric exclusion), r_s is the solute radius, ℓ_p is the hydraulic conductivity, μ is the kinematic fluid viscosity within the pores, ℓ_d is the diffusional permeability, D is the diffusion coefficient of the solute in aqueous solution and Π_M is a mean osmotic pressure (here assumed as the arithmetic mean of the boundary values of the osmotic pressures), f_p is an empirical function, used to take into account the restricted diffusion due to the increased hydrodynamic drag (Renkin, 1954):

$$f_p(x) = 1 - 2.104x + 2.09x^3 - 0.95x^5. \quad (4.9)$$

Note that all the previous quantities are dimensional.

Thermodynamic considerations of irreversible thermodynamics (Katchalsky and Curran, 1965) state that

$$\ell_d > \sigma^2 \ell_p, \quad (4.10)$$

we thus assume that the diffusional permeability is given by $\ell_d = \alpha \sigma^2 \ell_p$, where $\alpha > 1$ is a constant related to a Péclet number $\text{Pe} = \ell_p/\ell_d$ through $\alpha = 1/(\sigma^2 \text{Pe})$.

Manipulating the previous algebraic equations, we can express the diffusional permeability in terms of the reflection coefficient and the hydraulic conductivity as

$$\ell_d = \frac{8\mu D}{r_p^2 \Pi_M} \ell_p (1 - \sqrt{\sigma}) f_p\left(1 - \sqrt{1 - \sqrt{\sigma}}\right), \quad (4.11)$$

where the radius and the number of the pores can be estimated through the following

$$r_p = \frac{r_s}{1 - \sqrt{1 - \sqrt{\sigma_G}}}, \quad (4.12)$$

$$N = \frac{8\mu \ell_p^G}{\pi r_p^4}, \quad (4.13)$$

where reasonable values of σ_G and ℓ_p^G for the glycocalyx layer are reported for instance in Speziale et al. (2008). Note that the obtained mean pore radius

has dimension $r_p = 4.65$ nm, comparable the 4 – 5 nm half-distances of the periodic glycocalyx surface structure determined from electron micrographs (Squire et al., 2001) and the 5.7 nm pore exclusion size limiting glycocalyx permeation by dextrans (Vink and Duling, 2000).

The effective diffusion coefficient D can be estimated from the free diffusion coefficient D_{free} as $D = \theta_p D_{free}$, where the coefficient $\theta_p > 1$, defined as

$$\theta_p = \frac{\alpha \sigma^2 \Pi_M r_p^2}{8\mu D_{free}(1 - \sqrt{\sigma}) f_p(1 - \sqrt{1 - \sqrt{\sigma}})}, \quad (4.14)$$

simulates the increase of diffusivity due to the fact that solute molecules in a small-bore channel diffuse more easily and move more randomly than in an open space, owing to the wall friction producing different velocities over the cross-section of the pore, as described by Taylor (1953). Note that the effective diffusivity coefficients reported in the work of Taylor (1953) are 3 to 4 order of magnitude larger compared to the diffusion coefficient, whereas here the value of θ_p is about 33, possibly because of the micro scale processes. By defining θ_p as in equation (4.14), we automatically have that condition (4.10) is satisfied.

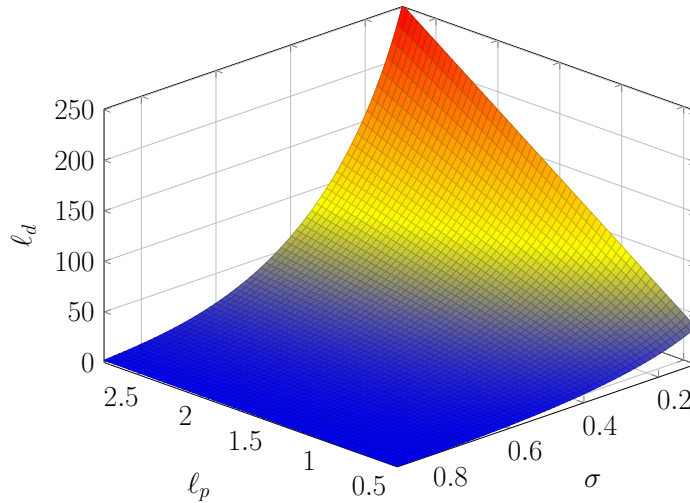


Figure 4.1: Diffusional permeability ℓ_d versus ℓ_p and σ . Here the physiological parameters ℓ_p and ℓ_d are dimensionless with respect to the weighted harmonic mean ℓ_p^H for the hydraulic conductivity.

Since the function f_p is positive (in a reasonable domain), we have that $\ell_d > 0$ and an increase in the hydraulic conductivity ℓ_p produces a linear increase in ℓ_d , as depicted in Figure 4.1. Equation (4.11) also states that a decrease in the reflection coefficient σ produces an increase in the diffusional

permeability ℓ_d (for a reasonable range of σ , see Figure 4.1), as we expect from the augmented mobility of the solute molecules.

4.2.1 Physiological parameters across the wall

In order to have smooth solutions, we consider a smooth transition between the two layers composing the vessel wall as in Chapter 3:

$$\begin{cases} \sigma(r) &= \frac{\sigma_G + \sigma_W}{2} - \frac{\sigma_G - \sigma_W}{2} \frac{r - r_g}{\sqrt{\varepsilon^2 + (r - r_g)^2}}, \\ \ell_p(r) &= \frac{\ell_p^G + \ell_p^W}{2} - \frac{\ell_p^G - \ell_p^W}{2} \frac{r - r_g}{\sqrt{\varepsilon^2 + (r - r_g)^2}}, \end{cases} \quad (4.15)$$

where sub-scripts G and W indicate the reflection coefficient of glycocalyx and endothelial cells, respectively, and r_g denotes the interface point between glycocalyx and endothelium. We control the transition between material properties of the two layers through the smoothing parameter ε . The larger it is the smoother the transitions are. Here, $\varepsilon^2 = 10^{-5}$, thus the transition is assumed smooth, even if quite sharp.

Table 4.1 shows typical values of geometrical and physiological features of an intact capillary, as well as the values of the osmotic and hydrostatic pressures within the lumen and in the external interstitial space. Also the physical and hydrodynamical properties of the solute (here albumin), as well as kinematic fluid viscosity within the pores, are reported.

4.3 Simulation of glycocalyx shedding

We have already mentioned that degradation and/or loss of glycocalyx have been shown during exposure to atherogenic/cardiovascular risk factors, including inflammatory and atherogenic stimuli, ischemia/reperfusion and oxidized low-density lipoprotein infusion (VanTeeffelen et al., 2007); furthermore, patients with type 1 diabetes mellitus and microalbuminuria are more susceptible to glycocalyx degradation (Nieuwdorp et al., 2006). Apart from pathological conditions, glycocalyx thickness can change also because of increased shear stress (as at atherosclerosis-prone sites) and in response to agonists such as adenosine, which may increase wall conductivity up to 40% (VanTeeffelen et al., 2005).

In this section we simulate glycocalyx deterioration, possibly due to physiological glycocalyx fibre rearrangement and/or to enzymatic digestion.

4.3.1 How to simulate glycocalyx modulation?

In Nieuwdorp et al. (2006), glycocalyx thickness in sub-lingual capillaries is estimated from the difference between capillary red blood cell column width during baseline (functionally perfused capillary diameter) and after passage

Parameter [unit]	Value	Reference
r_c [μm]	5	Charm and Kurland (1974)
r_g [μm]	5.15	Adamson et al. (2004)
r_o [μm]	5.5	Charm and Kurland (1974)
Π_c [mmHg]	25	Levick (1991)
Π_o [mmHg]	12	Levick (1991)
p_c [mmHg]	20	Levick (1991)
p_o [mmHg]	-1	Levick (1991)
σ_G	0.9	Speziale et al. (2008)
σ_W	0.1	Speziale et al. (2008)
ℓ_p^G [$\mu\text{m}^2\text{sec}^{-1}\text{mmHg}^{-1}$]	0.601854	Speziale et al. (2008)
ℓ_p^W [$\mu\text{m}^2\text{sec}^{-1}\text{mmHg}^{-1}$]	4.15203	Speziale et al. (2008)
μ [mmHg sec]	$5.2504 \cdot 10^{-6}$	Li et al. (2010)
r_s [μm^{-3}]	$3.6 \cdot 10^{-3}$	Levick and Michel (2010)
D_{free} [$\mu\text{m}^2 \text{sec}^{-1}$]	60	Stevens et al. (2007)
α	1.001	

Table 4.1: Typical values of material properties of a capillary: σ is the reflection coefficient and ℓ_p is the hydraulic conductivity. The typical values of capillary blood hydrostatic and osmotic pressures (p_c and Π_c) are reported against typical values of interstitial pressures p_o and Π_o . The superscripts G and W refer to glycocalyx and endothelial layers, respectively. μ is kinematic water viscosity, r_s is the mean molecular radius of human serum albumin and D_{free} is its free diffusion coefficient. The coefficient $\alpha > 1$ depends on a Péclet number and is defined such as to satisfy condition (4.10).

of a leukocyte (anatomic capillary diameter) and a decrease of about 45% is found in healthy subject glycocalyx thickness, compared to patients with type 1 diabetes mellitus. An electron microscopic study of mouse carotid arteries (van den Berg et al., 2006) shows a thinning of endothelial glycocalyx layer of about 75% at an atherosclerosis-prone site compared to glycocalyx thickness at a low-atherogenic-risk site (VanTeeffelen et al., 2007)

Moreover, Adamson (1990) observed that treatment of frog mesenteric capillaries with the glycocalyx-degrading enzyme pronase produces an approximately 2.5-fold increase in post-pronase hydraulic conductivity compared to the initial control value, accompanied by no significative changes in the morphology of inter-cellular clefts, but large alterations in luminal glycocalyx structure, due to its partial digestion (see also Figure 1 in van den Berg et al., 2003). This suggests a correlation between the changes in physiologically measured hydraulic conductivity and morphologically demonstrated alterations in glycocalyx structure. Moreover, the 2.5-fold increase in capillary permeability (which reaches nearly a 20-fold increase in particular vessels)

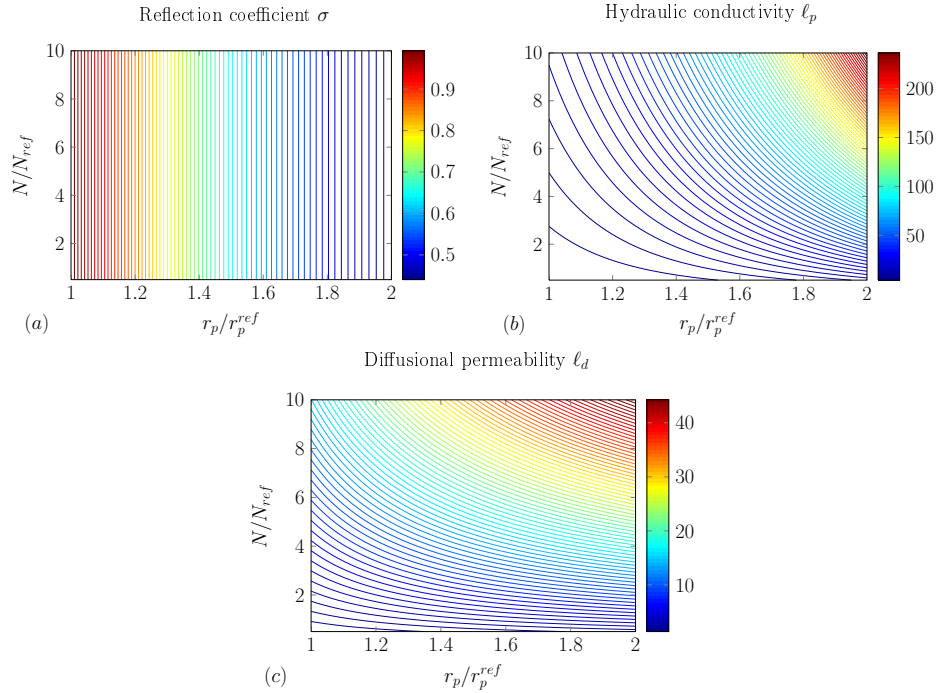


Figure 4.2: Contour lines of physiological parameters σ , ℓ_p and ℓ_d (divided by the reference value obtained for an integer vessel wall) varying with respect to pore radius r_p and the number N of pores in glycocalyx layer (divided by the corresponding values of an integer glycocalyx).

implies that at least 60% of the hydraulic resistance to plasma flow across microvessel walls is associated with endothelial glycocalyx.

Looking again at equation 4.7, we may conclude that an increment in glycocalyx hydraulic conductivity is due either to a raise in the number of pores or to an increase in their radius or by augmenting both of them (see Figure 3 in Adamson, 1990).

We can not neglect the relations described in Section 4.2 between the physiological parameters, thus we model the alteration of endothelial surface glycocalyx properties directly changing the number N of glycocalyx pores and their radii r_p , since both of them influence also the other parameters in the following way. A change in N determines a variation of both ℓ_p and ℓ_d , but does not alter σ since the latter is only related to the ratio of solute and pore size (see Figure 4.2a). On the contrary, a change in r_p produces a change in σ , ℓ_p and ℓ_d .

In Figure 4.2, the variation of the physiological parameters σ , ℓ_p and ℓ_d due to a change in the number N and radius r_p of pores in the glycocalyx layer is depicted. Note that all the quantities are reported with respect to the reference values reported in Table 4.1, obtained considering a typical

vessel wall with an integer glycocalyx.

We thus model the deterioration of endothelial glycocalyx by three means: (i) decreasing its thickness ℓ_G , (ii) increasing the number N of its pores and (iii) augmenting their radii r_p .

4.3.2 Fluxes in the case of glycocalyx damage

In Figure 4.3, we depict volume and solute fluxes divided by the reference fluxes obtained with typical values of an integer vessel wall reported in Table 4.1 versus the previously described normalised quantities ℓ_G , N and r_p . Glycocalyx thinning and an increase in pore number and/or radius result in an augmentation of plasma filtration and/or solute extravasation, as expected.

Note the 6 to 7-fold increase of volume flux in the case in which mean pore radius r_p increases, whereas the variation is halved in the case in which r_p is fixed, see Figure 4.3c. The influence of r_p on physiological parameters vary among them, see in particular Figure 4.2a in which doubling r_p , σ decreases by one half. This suggests a pivotal role of σ in volume flux, being more sensitive to variations of r_p compared to changes of the other parameters.

A role of glycocalyx degradation is recognised in sepsis with the onset of acute lung injury in most severe cases (Schmidt et al., 2012). In acute lung injury and acute respiratory distress syndrome, pulmonary oedema was observed, correlated to glycocalyx deterioration (Yang and Schmidt, 2013). To the best of our knowledge, myocardial tissue oedema, and in general extravascular oedema, are measured through the change in pericapillary space (van den Berg et al., 2003), without reporting the precise values of plasma and solute fluxes. An increase in pericapillary space by about 65% is thus measured during myocardial tissue oedema, demonstrating fluid and protein extravasation (van den Berg et al., 2003).

The behaviour of solute flux is analogous, except that a change in glycocalyx thickness and/or pore number quadruples the flux (see Figure 4.3d), whereas a change in r_p (and thus in σ) decouples this effect. These results agree with experimental results, where a significant increase in macromolecular flux across microvessel wall is described both after exposure to H_2O_2 (Singh et al., 2013) and after treatment with heparan-sulfate-degrading enzymes (Singh et al., 2007). Unfortunately, since pore radius and the number of the pores are not estimated from histological analysis, a fair comparison is not achievable. Depending of the enzymes used, a 1.4 to 3-fold increase in the trans-vascular albumin flux after enzyme-treatment compared to the initial macro-molecular flux occurs, thus confirming our predictions.

Looking at Figure 4.3, we may also observe that both fluxes do not change much varying ℓ_G compared to their stronger dependence on r_p (a)-(b). Their behaviour also depends on pore number: for small N , both fluxes are more sensitive to a change in N than to a variation of glycocalyx thickness (c)-(d),

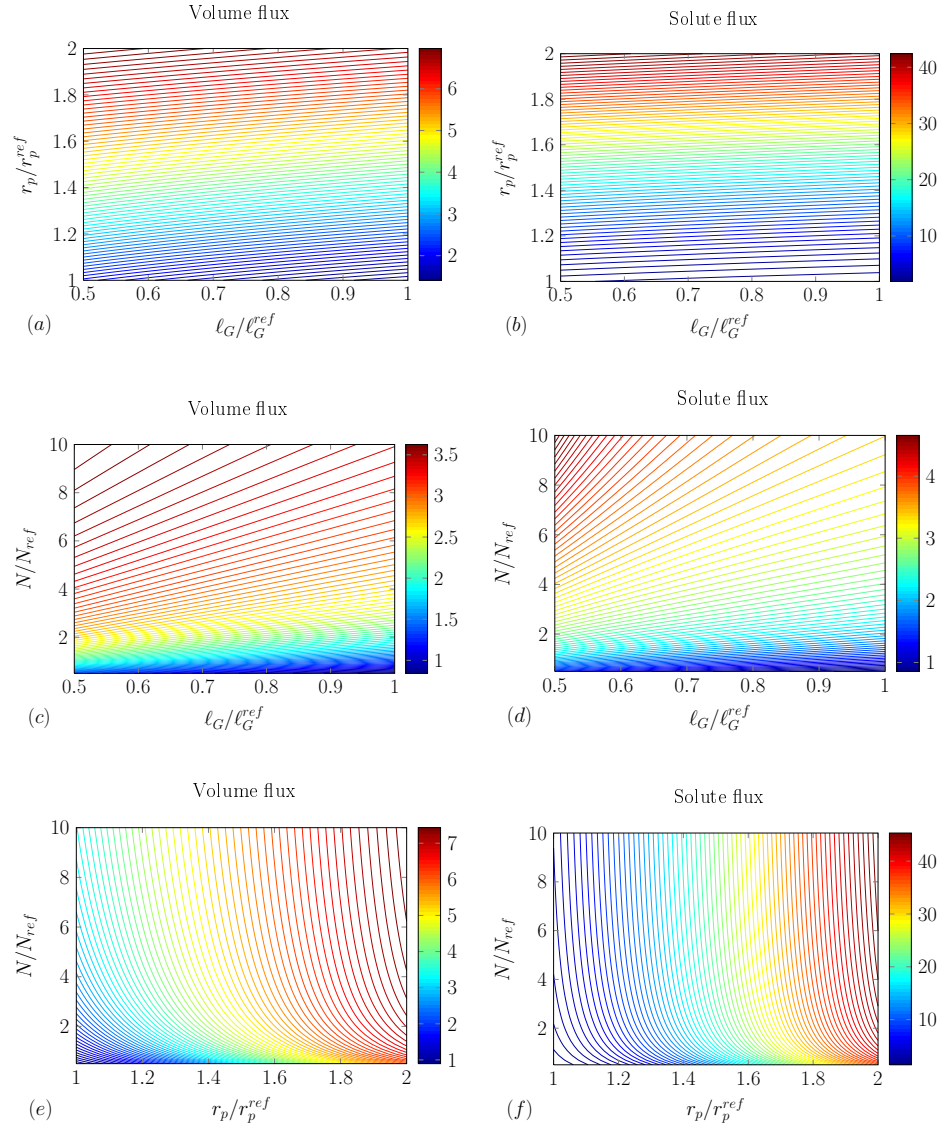


Figure 4.3: Contour lines of volume and solute fluxes (divided by reference fluxes) as functions of glycoalyx thickness ℓ_G , pore radius r_p and number of pores N (divided by the corresponding values of an integer glycoalyx).

wheres for higher values of N , they become more dependent on r_p (e)-(f).

4.4 Pressure influence on glycocalyx degeneration

In this section we study the impact on mean volume flux and mean solute flux of an increase in hydrostatic blood pressure, as in pre- and post-stenotic blood vessels.

In Figure 4.4, we plot volume and solute fluxes (divided by reference fluxes) versus the previous quantities (ℓ_G/ℓ_G^{ref} , N/N_{ref} and r_p/r_p^{ref}) and blood hydrostatic pressure p_c (divided by its normal value in a microvessel of a normotensive control), as reported in Table 4.1. Local hypertension results in an augmentation of plasma filtration and/or solute leakage, worsened by glycocalyx shedding, as expected.

In the brain, even the slight increase in pressure may produce serious consequences, as observed in the experiments of Mayhan and Heistad (1986), where an increase in cerebral venous pressure either due to phenylephrine-induced hypertension or to superior venae cavae occlusion is shown to lead to the disruption of rat cerebral capillaries.

In hypertensive retinopathy, the retinal vasculature may be sufficiently injured to cause occlusion or leakage, thus causing extra-vascular oedema and intraretinal hemorrhages in most severe cases. Also hypertensive optic neuropathy, accompanied to severe hypertension, correlates to flame hemorrhages and optic disc oedema (Chobanian et al., 2003).

Diabetes is often associated to glycocalyx degradation (Nieuwdorp et al., 2006) and is recently hypothesised to accelerate transvascular transport of both albumin and lipoproteins by 25% and 28%, respectively (Jensen et al., 2005), possibly explaining its association with proteinuria and a highly increased risk of atherosclerosis development. Moreover, this increased transvascular solute transport is accelerated in presence of systolic hypertension or albuminuria, where solute flux of albumin and low-density lipoprotein raises by 29% and 44%, respectively, compared to healthy controls.

This agrees with our predictions of a loosening in vascular solute barrier in the case of glycocalyx degradation, as for diabetic patients, even worsened in presence of hypertension.

We now look in detail at Figure 4.4. Halving glycocalyx thickness ℓ_G , both fluxes quintuple, showing a strong dependence on blood pressure p_c (a)-(b). Analogously, decoupling pore number N produces a decoupling even in both fluxes. Also in this case we may observe that this phenomenon is more strongly linked to blood pressure than to pore number, at least for large values of N (e)-(f). What is surprising is the different effect of a variation in r_p on plasma and solute fluxes, compared to the previous cases: a 14-fold increase in plasma flux and even an 80-fold rise in solute flux. Moreover, a strong dependence of both fluxes on both blood pressure and pore radius

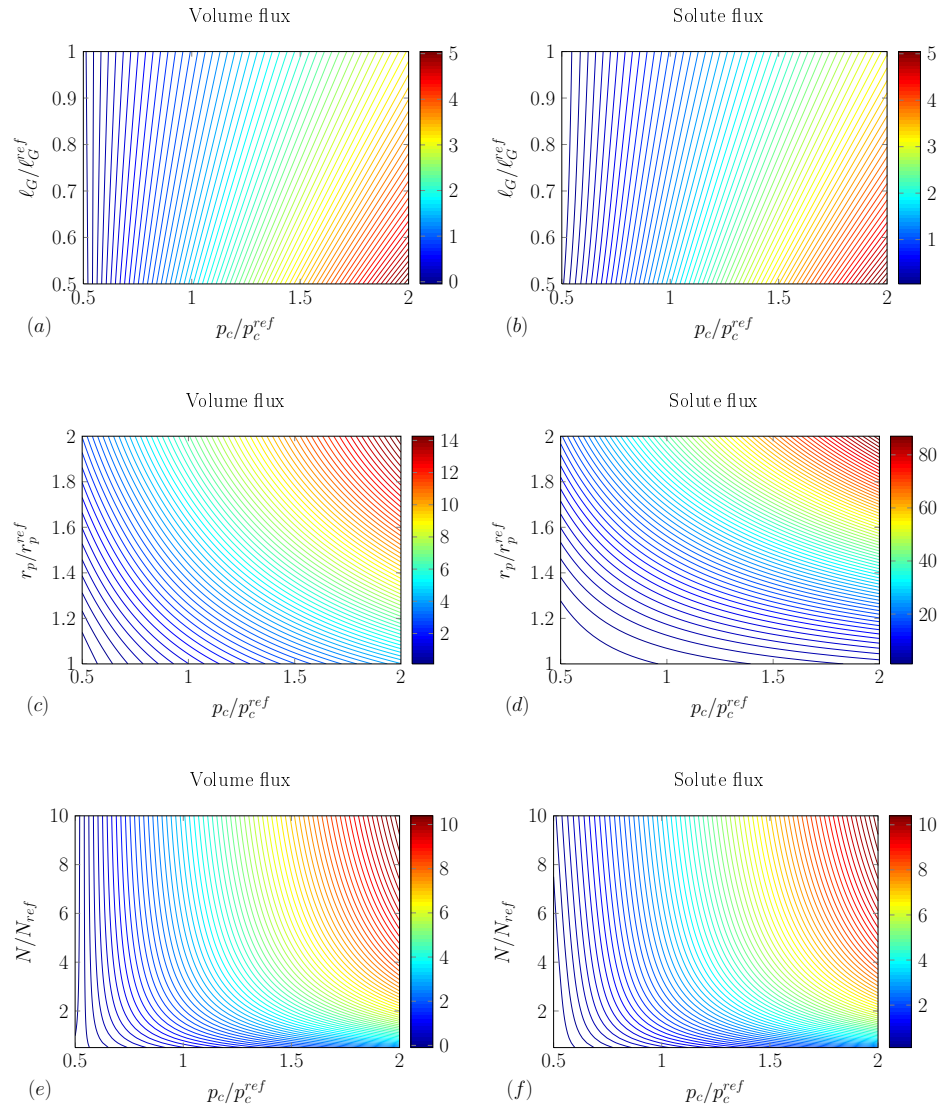


Figure 4.4: Contour lines of volume and solute fluxes (divided by reference fluxes) as functions of hydrostatic blood pressure p_c (normalised by its typical value in a microvessel of a normotensive control) and morphological and/or physical parameters ℓ_G , r_p and N (normalised by the corresponding values of an integer glycocalyx).

(and thus σ) is shown (c)-(d).

We compare our results to the experimental results of Valenzuela-Rendon and Manning (1990b,a), where trans-capillary flux of fluid and proteins in conscious dogs is incremented both during volume-loading hypertension and during angiotensin II-induced hypertension.

In their first experiment, where hypertension (with an increase in mean arterial pressure of 24%) is induced by volume-loading (Valenzuela-Rendon and Manning, 1990b), fluid flux increases 165%, whereas protein flux (apparently dominated by convection) increases only 57%. Analogously, during angiotensin II-induced hypertension experiment (Valenzuela-Rendon and Manning, 1990a), trans-capillary flux increases 45% and protein flux increases 24% (induced by an increase in mean arterial pressure of 45%).

Note that a change in mean arterial pressure is not directly correlated to capillary pressure, since the latter is also affected by nervous control, venous pressure, vascular resistance, gravity and distance along the capillary axis (Levick, 2010), being thus quite difficult to be estimated. Nevertheless, in both experiments of Valenzuela-Rendon and Manning (1990b,a), hypertension produces an increase in both volume and solute fluxes, as qualitatively reproduced by our model.

Note that here we are completely neglecting the role of lymphatic system, which drains away accumulated ultrafiltrate, demonstrated by the increase in its lymph flow by 2 to 3 times in thoracic duct (Valenzuela-Rendon and Manning, 1990b). Indeed, a well-known safety factor against oedema lies in the increment of lymph flow until it exceeds trans-capillary flow, thus limiting fluid accumulation in the surrounding tissues (Levick, 2010). To model this highly dynamic process, a mathematical description of tissue morphology and transport properties is needed, together with a reasonable modelling of the time-dependent pressure changes in lymphatic capillaries. This is outside the aim of the present work, but Chapter 5 will be directed toward a transient mathematical model of trans-vascular plasma filtration and solute transport.

4.5 Conclusions

We have applied our one-dimensional multi-layered steady-state mathematical model to simulate glycocalyx degeneration, due to its thinning and/or to lose of its transport properties.

The reconstructed plasma and solute fluxes across vessel walls show an higher impact of the mean pore radius representing glycocalyx mesh work compared to the other parameters (glycocalyx thickness and its pore number), suggesting a significative influence of glycocalyx reflection coefficient, only related to the ratio of the solute to the pore radii, into transport processes.

With our model, we have been also able to quantify the effects of hypertension on both fluxes, even in presence of glycocalyx deterioration, in agreement with experimental results reported in literature, where both oedema and hemorrhage are observed.

Due to the simplicity and the efficiency of our one-dimensional model, these simulations provide results in line with physiological studies and can possibly be a useful tool in the prediction of long-term effects of glycocalyx deterioration and/or hypertension.

To take into account also the dynamic changes in lymph flow and tissue properties, a time-dependent mathematical model of trans-vascular phenomena is needed. Chapter 5 has the objective of modelling the transient nature of biological transport processes.

Chapter 5

A time-dependent model

The time-dependent model presented in this Chapter is taken from Facchini et al. (2013d).

As already mentioned in the Introduction, to avoid the accumulation of plasma ultrafiltrate in the interstitium and to preserve volume homeostasis, it is now accepted that interstitial fluid, after filtrating through microvessel walls and having substantially reduced its protein content, drains into the lymphatic system, which in turn connects to the venous part of the circulatory system (e.g. Levick, 2010; Silverthorn, 2009).

This new view is confirmed by three considerations. The first one is related to the measurements of fluid filtration with respect to venous capillary pressure both immediately after an abrupt pressure raise/reduction (transient case) and several minutes after the change (steady state-case), showing that absorption occurs only in the transient case, since after some time filtration is restored (see Figure 3 in Levick and Michel, 2010). Also the direct measurement of all four *Starling's forces* (namely capillary blood pressure p_c , plasma colloid osmotic pressure Π_c , interstitial fluid pressure p_o and extravascular colloid osmotic pressure Π_o) in the same tissue and species proves that a constant state of filtration is present in almost all tissues, under normal conditions (see Figure 11.12 in Levick, 2010). Some exceptions of the sum-of-forces evidence are reported for example in Levick and Michel (2010), where the special case of water absorption from gut lumen is described. The last experimental and theoretical proof of absorption in steady state lies in the fact that Π_o is inversely related to filtration rate J_v thanks to the so-called *protein wash-down* effect. As a matter of fact, extravascular protein concentration is given by the ratio of the rate of solute influx to filtration rate, but the speed at which plasma is transferred across vascular membrane is higher compared to the protein transfer rate, since the small pores present on vessel wall slow down or even block blood proteins, meanwhile allowing fluid to pass freely through them. Thus, interstitial protein concentration

(and also osmotic pressure) changes inversely with capillary filtration rate, because the rate of solute influx is almost constant, if compared to the rate of plasma influx due to different pathways across which protein and plasma are transported (Levick, 2010).

Starling (1896), already in 1896, observed that fluid movement across vessel wall is driven by four main forces, the already mentioned Starling's forces, given by the differences of hydrostatic and osmotic pressures measured inside blood vessel and in the interstitium immediately outside. Almost all the measurements and the discussions were based on the experiments of Landis (1927) which are generally regarded as a confirmation of Starling's hypothesis. This was in fact quite misleading, since he blocked a capillary with a glass rod while keeping a constant hydrostatic pressure inside the microvessel through a micropipette inserted inside it and neglecting the dynamic nature of the process. Another important contribution was done by Pappenheimer and Soto-Rivera (1948), who estimated a mean hydrostatic pressure in capillaries knowing the pressure in arterial and venous end of a capillary bed and the ratio of pre- to post-capillary resistance (Levick, 2010). Around 70 years were needed to correct Starling's law taking into account the sieving effect of glycocalyx. This was done by Michel (1997) and Weinbaum (1998), who considered the differences between pressures measured in the lumen and just below glycocalyx as driving forces of filtration and solute transport in spite of the pressure differences between lumen and interstitium.

What was, unfortunately, neglected for many years was the dynamic component of the external pressures. It is a well-known fact that hydrostatic luminal pressure decreases along a capillary, thus reducing also filtration rate. It is also now established that, under normal conditions, a well-perfused capillary is in a state of filtration along its entire length, but it can absorb fluid transiently when blood pressure p_c falls (for instance during *hypovolemia*, a pathological decrease of blood volume).

Another important effect of the change in the external pressures lies in the decay in absorption, followed by a restoration of a state of (dynamic) equilibrium in which slight filtration occurs. In fact, plasma protein concentration below glycocalyx (and thus external osmotic pressure Π_o) increases as interstitial fluid is absorbed into the lumen, while interstitial pressure p_o decreases as fluid is removed from the interstitium, lowering the pressure exerted outside vessel wall (Levick, 2010; Levick and Michel, 2010).

We build up a time-dependent one-dimensional multi-layered mathematical model, where filtration and solute transport are strongly coupled and it is no longer possible to solve independently flow equation in the hydrostatic pressure and then plugging the solution into transport equation. After validating our model, we test it simulating an hemorrhage with associated abrupt blood pressure decrease, by considering the two different views: the traditional one, now disproved, with constant values of external hydrostatic and osmotic pressures, and the new one in which the transient absorption

due to the lowering of internal pressure raises extra-vascular osmotic pressure and reduces interstitial pressure.

The behaviour of external pressures is reconstructed qualitatively from Figure 3.B of Levick and Michel (2010), assuming an initial phase with constant values, followed by the decrease in hydrostatic internal pressure, determining an exponential change in both external pressures (augmentation of osmotic pressure and reduction of hydrostatic pressure) until new constant values are reached. The change of volume and solute fluxes in time is studied in both cases, paying attention to pressure distribution inside vessel wall.

The simulation of an hemorrhage with our model also depends on the physical features describing vessel wall anatomy: whether we consider a wall consisting of the endothelium internally coated by glycocalyx or if we assume the vessel wall as homogeneous with mean characteristics of the two layers composing it. In the second case, we can no longer distinguish glycocalyx from endothelium or junctions, thus neglecting the cleft exit microgradients below the glycocalyx, as described by Levick (2010).

The specific objective of the present chapter is thus to carry out a theoretical study of filtration and solute transport processes with a time-dependent mathematical model. We investigate what happens considering constant external pressures, thus neglecting plasma/interstitial fluid balance (Levick, 2010). Moreover, we consider an homogeneous vessel wall, thus lessening the sieving role of glycocalyx layer (VanTeeffelen et al., 2007).

5.1 The mathematical model

5.1.1 Statement of the problem

A series of *1D* and *3D* mathematical models was developed since 1950s (e.g. Michel and Curry, 1999; Sugihara-Seki and Fu, 2005, and references therein), showing that permeability to water and hydrophilic (water-loving) solutes in microvessels of different tissues can be accounted for by inter-endothelial cleft pathways and junction strands with discontinuous leakages (see Figure 5.1) with a surface fibre layer (the glycocalyx), as depicted in Figure 5.2.

Thus, we idealise a single microvessel wall by assuming it as composed by two rigid concentric circular hollow cylinders with homogeneous properties: the internal ones representing surface glycocalyx and the outer one standing for the endothelial cells with the junctions between them, as depicted in Figure 5.3.

Even if glycocalyx is a negatively-charged membrane (Levick, 2010) and some efforts have been done in the modelling of charged molecule transport (e.g. Fu et al., 2003) and of active transport (e.g. Patlak et al., 1963), here we are only interested in passive transport of a single non-electrolyte under isothermal conditions (Katchalsky and Curran, 1965). The solute considered in the present chapter is *albumin*, which “accounts for half the plasma

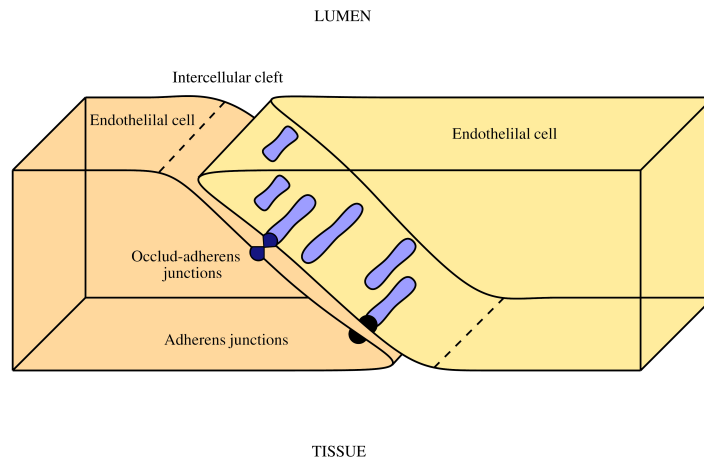


Figure 5.1: Illustration of an inter-cellular cleft between endothelial cells in a typical microvessel, with some protein complexes either providing anchorage and cell stability (adherens junctions) or forming an almost impermeable barrier to fluid and macromolecules (tight/occludens junctions).

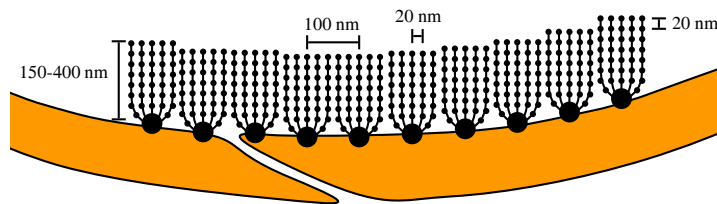


Figure 5.2: Illustration of glycocalyx in a typical microvessel, with the range of dimensions of the most relevant anatomical elements (transverse view).

protein mass and generates about two-thirds of the colloid osmotic pressure” (Levick, 2010). Note that the osmotic pressure exerted by albumin is highly influenced by its negative charge (which accounts for about one-third of its osmotic pressure) and cannot thus be correctly predicted by van’t Hoff’s law, which is for ideal solutes (Levick, 2010). Nevertheless, we assume that transvascular exchange processes are entirely passive and that the solute considered is ideal and neutral.

We also consider the flow as completely radial, taking into account a reasonable assumptions of vessel radial symmetry and thus focusing on the dynamics in every cross-section of the cylinder (Speziale et al., 2008).

The presence of the central core of red blood cells in the lumen and a cell-depleted wall layer, possibly due to glycocalyx reducing the effective cross-sectional area available for plasma and red cell motion, in the neighbourhood of the vessel wall justifies the assumption of a Newtonian fluid crossing vessel

wall (Sugihara-Seki and Fu, 2005).

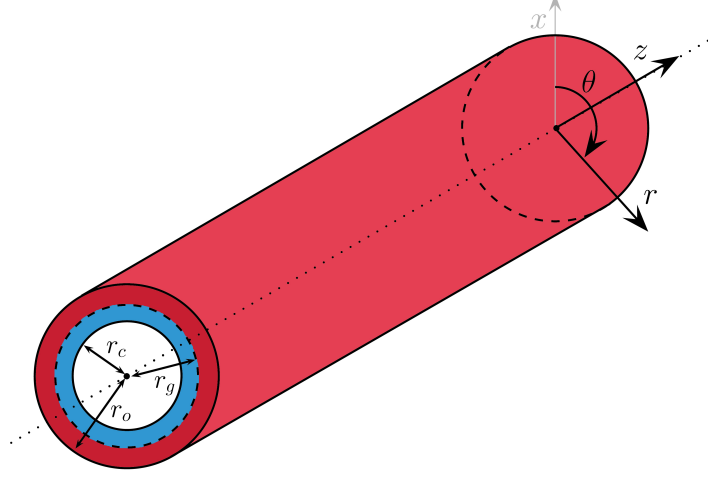


Figure 5.3: Sketch of our static mathematical domain: an infinitely-long hollow circular cylinder composed by two homogeneous uniform porous membranes representing glycocalyx for $r \in (r_c, r_g)$ and endothelial cells for $r \in (r_g, r_o)$.

5.1.2 Governing equations in dimensionless form

Under the above hypothesis, the volume specific discharge $q_v = q_v(x, y, z, t)$ and the total solute specific discharge $q_s = q_s(x, y, z, t)$ are related to hydrostatic pressure $p = p(x, y, z, t)$, osmotic pressure $\Pi = \Pi(x, y, z, t)$ and protein concentration $c = c(x, y, z, t)$ through the following expressions reported in Chapter 3

$$\begin{cases} q_v &= -\ell_p (\nabla p - \sigma \nabla \Pi), \\ q_s &= c [\ell_p (\sigma - 1) \nabla p + (\ell_p \sigma - \ell_d) \nabla \Pi], \end{cases} \quad (5.1)$$

where ℓ_p is the hydraulic conductivity, σ is the membrane reflection coefficient and ℓ_d is the diffusional permeability.

In order to correlate the osmotic pressure and the protein concentration, we assume the *van't Hoff law* (Levick, 2010) stating that

$$\Pi = RTc, \quad (5.2)$$

where R is the gas constant and T is the absolute temperature, even being aware that there are better functions expressing the relationship between protein osmotic pressure Π and their concentration c , as the Landis and Pappenheimer (1963) cubic empirical equation

$$\Pi = 2.1 c + 0.16 c^2 + 0.009 c^3, \quad (5.3)$$

which takes into account the non-ideality of the solution (Katz, 1985). Nevertheless, we consider the ideality assumption for protein, in order to have simpler equations.

Mass conservation of blood plasma and of the solute leads to the following governing equations

$$\begin{cases} \frac{S_S}{\rho g} \frac{\partial p}{\partial t} &= -\nabla \cdot q_v, \\ \frac{1}{RT} \frac{\partial \Pi}{\partial t} &= -\nabla \cdot q_s, \end{cases} \quad (5.4)$$

where ρ is the fluid (here blood plasma) density, g is the standard gravitational acceleration and S_S is the *specific storage* measuring the amount of plasma that a portion of vessel wall releases from storage, per unit mass or volume of wall, per unit change in hydraulic head, while remaining fully saturated. The specific storage is given by the following expression

$$S_S = \gamma_w(\beta_m + n\beta_w), \quad (5.5)$$

where $\gamma_w = \rho g$ is plasma specific weight, β_w is water compressibility, β_m and n are blood vessel wall compressibility and porosity, respectively.

Thus system (5.4) simplifies into

$$\begin{cases} (\beta_m + n\beta_w) \frac{\partial p}{\partial t} &= -\nabla \cdot [-\ell_p (\nabla p - \sigma \nabla \Pi)], \\ \frac{\partial \Pi}{\partial t} &= -\nabla \cdot \{\Pi [\ell_p (\sigma - 1) \nabla p + (\ell_p \sigma - \ell_d) \nabla \Pi]\}, \end{cases} \quad (5.6)$$

which, written in cylindrical coordinates (r, θ, z) , as depicted in Figure 5.3, and assuming radial symmetry, takes the following dimensionless form

$$\begin{cases} \alpha \frac{\partial p}{\partial t} &= \frac{1}{r + \xi} \frac{\partial}{\partial r} \left[(r + \xi) \ell_p \left(\frac{\partial p}{\partial r} - \sigma \frac{\partial \Pi}{\partial r} \right) \right], \\ \frac{\partial \Pi}{\partial t} &= \frac{1}{r + \xi} \frac{\partial}{\partial r} \left[-(r + \xi) \Pi \left(A \frac{\partial p}{\partial r} + B \frac{\partial \Pi}{\partial r} \right) \right], \end{cases} \quad (5.7)$$

for $r \in (0, 1)$ and $t > 0$, where $\alpha = (\beta_m + n\beta_w)p_R$, p_R is a reference pressure and the dimensionless quantities are defined as follows

$$\begin{aligned} p &= \frac{p^*}{p_R}, & \Pi &= \frac{\Pi^*}{p_R}, & \xi &= \frac{r_c}{r_o - r_c}, & r &= \frac{r^* - r_c}{r_o - r_c}, & t &= \frac{t^*}{t_R}, \\ \ell_p &= \frac{\ell_p^*}{\ell_p^H}, & \ell_d &= \frac{\ell_d^*}{\ell_p^H}, & A &= \frac{\ell_p^* (\sigma - 1)}{\ell_p^H}, & B &= \frac{\ell_p^* \sigma - \ell_d^*}{\ell_p^H}, \end{aligned} \quad (5.8)$$

where superscripts * denote dimensional quantities, r_o is the external radius of vessel wall and r_c is the internal radius of vessel wall identified with the internal surface of glycocalyx. Furthermore, ℓ_p^H is the harmonic mean for the

dimensional hydraulic conductivity ℓ_p^* among the layers, weighted by each layer thickness, which for two layers is given by

$$\ell_p^H = \frac{r_o - r_c}{\frac{r_g - r_c}{\ell_p^G} + \frac{r_o - r_g}{\ell_p^W}}, \quad (5.9)$$

where ℓ_p^G refers to the glycocalyx layer (r_c, r_g) and ℓ_p^W to the endothelial cells composing the proper vessel wall (r_g, r_o). The reference time is given by $t_R = (\Delta r)^2 / (\ell_p^H p_R)$ and we choose as reference pressure $p_R = |p_o^0|$, where p_o^0 is the (dimensional) initial external hydrostatic pressure.

5.1.3 Flux reconstruction

Since we are interested in the dimensionless fluxes, we reconstruct them after solving system (5.7) in the unknown pressure functions. At each time t , the fluxes are given by the mean spatial values of the following expressions

$$J_v(t) = \int_0^{2\pi} q_v(r, t) (r + \xi) d\theta = -2\pi(r + \xi) \ell_p \left(\frac{\partial p}{\partial r} - \sigma \frac{\partial \Pi}{\partial r} \right), \quad (5.10)$$

$$J_s(t) = \int_0^{2\pi} q_s(r, t) (r + \xi) d\theta = 2\pi(r + \xi) \Pi \left[\ell_p(\sigma - 1) \frac{\partial p}{\partial r} + (\ell_p \sigma - \ell_d) \frac{\partial \Pi}{\partial r} \right], \quad (5.11)$$

where θ is the angle as depicted in Figure 5.3, while volume and solute fluxes are dimensionless with respect to $\ell_p^H |p_o|$ and $\ell_p^H |p_o|^2 / (RT)$ (dimensional quantities), respectively.

5.1.4 Physiological parameters

In order to have a smooth initial condition, we consider the model of smooth transition between the two layers composing vessel wall as in Chapter 3:

$$\sigma(r) = \frac{\sigma_G + \sigma_W}{2} - \frac{\sigma_G - \sigma_W}{2} \frac{r - r_g}{\sqrt{\varepsilon^2 + (r - r_g)^2}}, \quad (5.12)$$

where both sub-scripts G and W indicate the reflection coefficient of glycocalyx and the endothelial cells, respectively. The distribution of $\ell_p(r)$ and $\ell_d(r)$ are totally analogous. With this function we control the smoothness of the physiological properties varying at the interface between the two layers. A discontinuous transition occurs for $\varepsilon = 0$ and it becomes progressively smoother for $\varepsilon > 0$ to simulate possible gradual transitions (Sugihara-Seki and Fu, 2005). Here, the transition between the material properties of the two layers is represented by assuming $\varepsilon^2 = 10^{-4}$, unless otherwise stated.

Table 5.1 shows typical values of geometrical and physiological features of an intact capillary, as well as the values of osmotic and hydrostatic pressures

within the lumen and in the external interstitial space, at the initial (with superscript 0) and exit times (with superscript T). Also the compressibilities of the fluid and of the wall, as well as medium porosity, are reported.

Parameter [unit]	Value	Reference
r_c [μm]	5	Charm and Kurland (1974)
r_g [μm]	5.15	Adamson et al. (2004)
r_o [μm]	5.5	Charm and Kurland (1974)
Π_c^0 [mmHg]	25	Levick and Michel (2010)
Π_o^0 [mmHg]	8	Levick and Michel (2010)
p_c^0 [mmHg]	22	Levick and Michel (2010)
p_o^0 [mmHg]	-1.3	Levick and Michel (2010)
Π_o^T [mmHg]	15	Levick and Michel (2010)
p_c^T [mmHg]	7.36	Levick and Michel (2010)
p_o^T [mmHg]	-3.6	Levick and Michel (2010)
σ_G	0.9	Michel and Phillips (1987)
σ_W	0.1	Hu and Weinbaum (1999)
ℓ_p^G [$\mu\text{m}^2\text{sec}^{-1}\text{mmHg}^{-1}$]	0.601854	Speziale et al. (2008)
ℓ_p^W [$\mu\text{m}^2\text{sec}^{-1}\text{mmHg}^{-1}$]	4.15203	Speziale et al. (2008)
ℓ_d^G [$\mu\text{m}^2\text{sec}^{-1}\text{mmHg}^{-1}$]	0.536252	Facchini et al. (2013b)
ℓ_d^W [$\mu\text{m}^2\text{sec}^{-1}\text{mmHg}^{-1}$]	3.69946	Facchini et al. (2013b)
β_w [mmHg $^{-1}$]	$5.45 \cdot 10^{-8}$	Urick (1947)
β_m [mmHg $^{-1}$]	$9.21 \cdot 10^{-6}$	Carew et al. (1968)
n	0.5	Robinson (1988)

Table 5.1: Typical values of material properties of a capillary: σ is the reflection coefficient, ℓ_p is the hydraulic conductivity, ℓ_d is the diffusional permeability. Superscripts G and W refer to glycocalyx and endothelial layers, respectively. As described in Section 5.3.1, boundary conditions change following equations (5.34)-(5.36)-(5.37) with initial (at $t = 0$) and final (at $t = T$) values denoted with superscripts 0 and T , respectively. The coefficient β_w refers to the compressibility of horse blood plasma, while β_m is the maximum value of blood vessel wall compressibility measured in dog descending thoracic aorta. The porosity n was measured in an arterial graft prosthesis.

5.1.5 Linearised problem

The second equation of the non-linear system of PDEs (5.7) can be linearised by assuming that osmotic pressure is a small perturbation $\epsilon(r, t)$ around a reference value Π_R (here the arithmetic mean of the initial boundary values of the osmotic pressure) and neglecting the products of the terms involving

$\epsilon(r, t)$ and its derivatives, thus obtaining

$$\begin{cases} \alpha \frac{\partial p}{\partial t} = \frac{1}{r + \xi} \frac{\partial}{\partial r} \left[(r + \xi) \ell_p \left(\frac{\partial p}{\partial r} - \sigma \frac{\partial \epsilon}{\partial r} \right) \right], \\ \frac{\partial \epsilon}{\partial t} = \frac{1}{r + \xi} \frac{\partial}{\partial r} \left[-(r + \xi) \Pi_R \left(A \frac{\partial p}{\partial r} + B \frac{\partial \epsilon}{\partial r} \right) \right], \end{cases} \quad (5.13)$$

for $r \in (0, 1)$ and $t > 0$, in the unknowns functions $p = p(r, t)$ and $\epsilon = \epsilon(r, t) = \Pi(r, t) - \Pi_R$, where $A = \ell_p(\sigma - 1)$ and $B = \ell_p\sigma - \ell_d$.

Linear system (5.13) should be solved with the following initial/boundary conditions

$$\begin{cases} p(r, 0) = p^0(r), \\ \epsilon(r, 0) = \Pi^0(r) - \Pi_R, \\ p(0, t) = p_c(t), \\ p(1, t) = p_o(t), \\ \epsilon(0, t) = \Pi_c(t) - \Pi_R, \\ \epsilon(1, t) = \Pi_o(t) - \Pi_R. \end{cases} \quad (5.14)$$

Note that the steady-state solutions of this problem are different from the ones of the general problem.

Steady-state single-layered solutions

In the case of constant physiological parameters ℓ_p , σ , A and B (single-layered model), we have the following exact analytical solution for the pressures:

$$p(r) = \frac{(p_c - p_o) \ln(r + \xi) + p_o \ln(\xi) - p_c \ln(1 + \xi)}{\ln(\xi) - \ln(1 + \xi)}, \quad (5.15)$$

$$\Pi(r) = \frac{(\Pi_c - \Pi_o) \ln(r + \xi) + \Pi_o \ln(\xi) - \Pi_c \ln(1 + \xi)}{\ln(\xi) - \ln(1 + \xi)}, \quad (5.16)$$

with fluxes equal to

$$J_v = -2\pi k_1 = -2\pi \frac{\ell_p [(p_c - p_o) - \sigma(\Pi_c - \Pi_o)]}{\ln(\xi) - \ln(1 + \xi)}, \quad (5.17)$$

$$J_s = 2\pi k_2 = 2\pi \frac{\ell_p(\sigma - 1)(p_c - p_o) + (\ell_p\sigma - \ell_d)(\Pi_c - \Pi_o)}{\ln(\xi) - \ln(1 + \xi)}, \quad (5.18)$$

since

$$k_1 = \frac{\ell_p [(p_c - p_o) - \sigma(\Pi_c - \Pi_o)]}{\ln(\xi) - \ln(1 + \xi)}, \quad (5.19)$$

$$k_2 = \frac{\ell_p(\sigma - 1)(p_c - p_o) + (\ell_p\sigma - \ell_d)(\Pi_c - \Pi_o)}{\ln(\xi) - \ln(1 + \xi)}. \quad (5.20)$$

Steady-state two-layered solutions

Following the same procedure described in Chapter 3, we assume that both the physiological parameters (ℓ_p , σ , A and B) and the integration constants (k_1 , k_2 , k_3 and k_4) are layer-specific, denoting with the sub- or super-script G the values in the first (Glycocalyx) layer and with W the values in the second (endothelium composing the vessel Wall) layer.

The steady-state problem obtained from linearised system (5.13) in the two-layered model has the following exact analytical solution for the pressures:

$$p_i(r) = \left[\sigma_i \frac{k_2 - k_1(\sigma_i - 1)}{\ell_p^i \sigma_i^2 - \ell_d^i} + \frac{k_1}{\ell_p^i} \right] \ln(r + \xi) + k_3^i + \sigma_i k_4^i, \quad (5.21)$$

$$\Pi_i(r) = \Pi_R + \frac{k_2 - k_1(\sigma_i - 1)}{\ell_p^i \sigma_i^2 - \ell_d^i} \ln(r + \xi) + k_4^i, \quad (5.22)$$

for each layer $i \in \{G, W\}$, with integration constants

$$\begin{aligned} k_1 &= \frac{\ell_p^G \ell_p^W C_W \eta_G [\ln(r_g + \xi) - \ln(\xi)] - C_G \eta_W [\ln(r_g + \xi) - \ln(1 + \xi)]}{\phi \delta - \psi}, \\ k_2 &= \frac{\ell_p^W C_W \gamma_G [\ln(r_g + \xi) - \ln(\xi)] - \ell_p^G C_G \gamma_W [\ln(r_g + \xi) - \ln(1 + \xi)]}{\phi \delta - \psi}, \\ k_3^G &= p_c - \sigma_G (\Pi_c - \Pi_R) - \frac{k_1}{\ell_p^G} \ln(\xi), \\ k_3^W &= p_o - \sigma_W (\Pi_o - \Pi_R) - \frac{k_1}{\ell_p^W} \ln(1 + \xi), \\ k_4^G &= \Pi_c - \Pi_R - \frac{k_2 - k_1(\sigma_G - 1)}{\ell_p^G \sigma_G^2 - \ell_d^G} \ln(\xi), \\ k_4^W &= \Pi_o - \Pi_R - \frac{k_2 - k_1(\sigma_W - 1)}{\ell_p^W \sigma_W^2 - \ell_d^W} \ln(1 + \xi), \end{aligned} \quad (5.23)$$

with parameters

$$\begin{aligned} C_i &= \ell_p^i \sigma_i^2 - \ell_d^i, \\ \eta_G &= (p_c - p_o) - \sigma_G (\Pi_c - \Pi_o), \\ \eta_W &= (p_c - p_o) - \sigma_W (\Pi_c - \Pi_o), \\ \gamma_G &= \ell_p^G (\sigma_G - 1) (p_c - p_o) + (\ell_p^G \sigma_G - \ell_d^G) (\Pi_c - \Pi_o), \\ \gamma_W &= \ell_p^W (\sigma_W - 1) (p_c - p_o) + (\ell_p^W \sigma_W - \ell_d^W) (\Pi_c - \Pi_o), \\ \delta &= \ell_p^W \ln(\xi) + (\ell_p^G - \ell_p^W) \ln(r_g + \xi) - \ell_p^G \ln(1 + \xi), \\ \phi &= -C_W \ln(\xi) - (C_G - C_W) \ln(r_g + \xi) + C_G \ln(1 + \xi), \\ \psi &= \ell_p^G \ell_p^W (\sigma_G - \sigma_W)^2 [\ln(r_g + \xi) - \ln(\xi)] [\ln(r_g + \xi) - \ln(1 + \xi)], \end{aligned} \quad (5.24)$$

and fluxes equal to

$$\begin{aligned} J_v &= -2\pi \ell_p^G \ell_p^W \frac{C_W \eta_G [\ln(r_g + \xi) - \ln(\xi)] - C_G \eta_W [\ln(r_g + \xi) - \ln(1 + \xi)]}{\phi \delta - \psi}, \\ J_s &= 2\pi \frac{\ell_p^W C_W \gamma_G [\ln(r_g + \xi) - \ln(\xi)] - \ell_p^G C_G \gamma_W [\ln(r_g + \xi) - \ln(1 + \xi)]}{\phi \delta - \psi}. \end{aligned} \quad (5.25)$$

5.1.6 Numerical methods

We rewrite the non-linear system of PDEs (5.7) as

$$\begin{cases} \alpha \frac{\partial p}{\partial t} = \frac{1}{r + \xi} \left[\frac{\partial}{\partial r} \left(\mathcal{F} \frac{\partial p}{\partial r} \right) + \frac{\partial}{\partial r} \left(\mathcal{G} \frac{\partial \Pi}{\partial r} \right) \right], \\ \frac{\partial \Pi}{\partial t} = \frac{1}{r + \xi} \left[\frac{\partial}{\partial r} \left(\mathcal{H} \Pi \frac{\partial p}{\partial r} \right) + \frac{\partial}{\partial r} \left(\mathcal{L} \Pi \frac{\partial \Pi}{\partial r} \right) \right], \end{cases} \quad (5.26)$$

for $r \in (0, 1)$ and $t > 0$, in the unknown functions $p = p(r, t)$ and $\Pi = \Pi(r, t)$, where the auxiliary functions are defined as

$$\begin{aligned} \mathcal{F}(r) &= +(r + \xi) \ell_p(r), \\ \mathcal{G}(r) &= -(r + \xi) \ell_p(r) \sigma(r), \\ \mathcal{H}(r) &= -(r + \xi) \ell_p(r) [\sigma(r) - 1], \\ \mathcal{L}(r) &= -(r + \xi) [\ell_p(r) \sigma(r) - \ell_d(r)]. \end{aligned} \quad (5.27)$$

We apply the implicit *Crank-Nicolson finite difference scheme* proposed in Freeze (1975), which leads to the following non-linear algebraic system

$$\begin{aligned} & -(\mathcal{F}_{i-1} + \mathcal{F}_i) p_{i-1}^{n+1} + \left(\mathcal{F}_{i-1} + 2\mathcal{F}_i + \mathcal{F}_{i+1} + \alpha \frac{4(\Delta x)^2}{\Delta t} (r_i + \xi) \right) p_i^{n+1} + \\ & \quad -(\mathcal{F}_i + \mathcal{F}_{i+1}) p_{i+1}^{n+1} - (\mathcal{G}_{i-1} + \mathcal{G}_i) \Pi_{i-1}^{n+1} + \\ & \quad + (\mathcal{G}_{i-1} + 2\mathcal{G}_i + \mathcal{G}_{i+1}) \Pi_i^{n+1} - (\mathcal{G}_i + \mathcal{G}_{i+1}) \Pi_{i+1}^{n+1} = S_1^{(i,n)}, \\ 2\Pi_i^{n+1} & \left[\frac{4(\Delta x)^2}{\Delta t} (r_i + \xi) - (\mathcal{H}_{i-1} + \mathcal{H}_i) p_{i-1}^{n+1} + (\mathcal{H}_{i-1} + 2\mathcal{H}_i + \mathcal{H}_{i+1}) p_i^{n+1} + \right. \\ & \quad \left. - (\mathcal{H}_i + \mathcal{H}_{i+1}) p_{i+1}^{n+1} - (\mathcal{L}_{i-1} + \mathcal{L}_i) \Pi_{i-1}^{n+1} + \right. \\ & \quad \left. + (\mathcal{L}_{i-1} + 2\mathcal{L}_i + \mathcal{L}_{i+1}) \Pi_i^{n+1} - (\mathcal{L}_i + \mathcal{L}_{i+1}) \Pi_{i+1}^{n+1} \right] + \\ & \quad - (\Pi_{i+1}^{n+1} - \Pi_{i-1}^{n+1}) [\mathcal{H}_i (p_{i+1}^{n+1} - p_{i-1}^{n+1}) + \mathcal{L}_i (\Pi_{i+1}^{n+1} - \Pi_{i-1}^{n+1})] = S_2^{(i,n)}, \end{aligned} \quad (5.28)$$

to be solved using a Newton's method, where the source terms are defined as follows

$$\begin{aligned} S_1^{(i,n)} &:= \alpha \frac{4(\Delta x)^2}{\Delta t} (r_i + \xi) p_i^n + [(\mathcal{F}_i + \mathcal{F}_{i+1}) (p_{i+1}^n - p_i^n) - (\mathcal{F}_{i-1} + \mathcal{F}_i) (p_i^n - p_{i-1}^n) + \\ & \quad + (\mathcal{G}_i + \mathcal{G}_{i+1}) (\Pi_{i+1}^n - \Pi_i^n) - (\mathcal{G}_{i-1} + \mathcal{G}_i) (\Pi_i^n - \Pi_{i-1}^n)], \\ S_2^{(i,n)} &:= \frac{8(\Delta x)^2}{\Delta t} (r_i + \xi) \Pi_i^n + \{(\Pi_{i+1}^n - \Pi_{i-1}^n) [\mathcal{H}_i (p_{i+1}^n - p_{i-1}^n) + \mathcal{L}_i (\Pi_{i+1}^n - \Pi_{i-1}^n)] + \\ & \quad + 2\Pi_i^n [(\mathcal{H}_i + \mathcal{H}_{i+1}) (p_{i+1}^n - p_i^n) - (\mathcal{H}_{i-1} + \mathcal{H}_i) (p_i^n - p_{i-1}^n) + \\ & \quad + (\mathcal{L}_i + \mathcal{L}_{i+1}) (\Pi_{i+1}^n - \Pi_i^n) - (\mathcal{L}_{i-1} + \mathcal{L}_i) (\Pi_i^n - \Pi_{i-1}^n)]\}. \end{aligned} \quad (5.29)$$

Note that Δx denotes the mesh spacing of the spatial grid $\{r_i\}_{i=0}^{N+1}$ and Δt denotes the time step between two adjacent temporal grid points

$\{t^n\}_{n=0}^{M+1}$, while hydrostatic and the osmotic pressures are approximated by $p_i^n \approx p(r_i, t^n)$ and $\Pi_i^n \approx \Pi(r_i, t^n)$, respectively. The auxiliary functions assume the following values: $\mathcal{F}_i = \mathcal{F}(r_i)$, $\mathcal{G}_i = \mathcal{G}(r_i)$, $\mathcal{H}_i = \mathcal{H}(r_i)$ and $\mathcal{L}_i = \mathcal{L}(r_i)$.

In order to solve system (5.7), we need to prescribe an exit time $T > 0$, so that all boundary conditions are defined for $t \in [0, T]$, and to compute the initial conditions. We also take care that r_g lies between two spatial grid points, without being one of them.

For each time step, we need many mesh points to have an accurate reconstruction of the fluxes, as already noted in Chapter 3.

5.2 Validation of the model

In this section, we validate our time-dependent full model, first by choosing arbitrary initial conditions, constant boundary conditions and looking at the convergence of both pressures to the steady-state analytical solutions reported in Chapter 3. Then, we check the transient nature of our mathematical model by modifying the BVP introducing source terms, in order to have an exact analytical solution of the transient modified problem to compare it with the numerical solutions at given times.

5.2.1 Steady state

We start from the study of the convergence of the numerical solutions to the steady-state pressures of the two-layered problem with discontinuous physiological parameters (namely $\varepsilon = 0$) reported in Chapter 3.

As initial conditions for this convergence study, we choose a linear distribution of both pressures with constant boundary conditions, equal to the initial values reported in Table 5.1.

At first, there are no significant changes in the osmotic pressure, while hydrostatic pressure varies continuously (see the solutions at time $t = 1.02 \cdot 10^{-6}$ in Figure 5.4), until it reaches a halt at around $t = 1.02 \cdot 10^{-4}$ (see Figure 5.5). At this point, osmotic pressure starts to gradually decrease in proximity of the interface, wedging, while hydrostatic pressure slowly changes in a coupled way (see the solutions at time $t = 1.02 \cdot 10^{-2}$), until both pressures gradually approach the steady-state solutions (see the solutions at time $t = 1.02 \cdot 10^{-1}$, namely 13 milliseconds after the initial time, in Figure 5.4).

In Figure 5.5, the L_2 -norm of the difference between the transient numerical solution and the steady-state analytical solution of both osmotic and the hydrostatic pressure are depicted with respect to time t . The convergence is quick at the beginning (until around $t = 10^{-4}$), but then it gradually slows down (note that the scale is logarithmic).

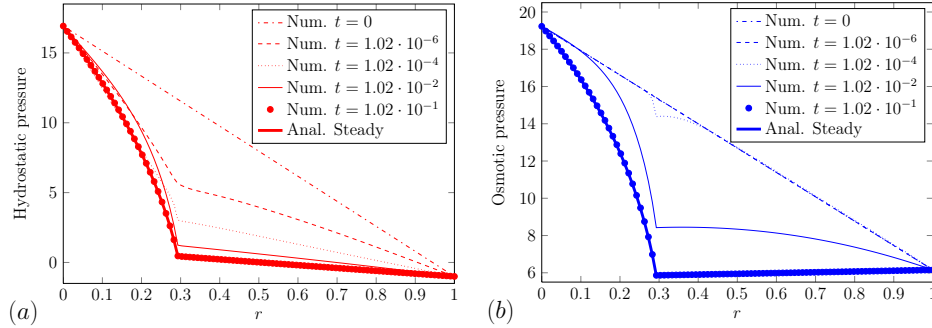


Figure 5.4: Hydrostatic (a) and osmotic (b) pressures for the two-layered model at given times $t \in \{0, 1.02 \cdot 10^{-6}, 1.02 \cdot 10^{-4}, 1.02 \cdot 10^{-2}, 1.02 \cdot 10^{-1}\}$, obtained numerically with a spatial grid of 100 points, $\Delta t = 10^{-6} \cdot (\Delta x)^2$, $\varepsilon = 0$ and tolerance equal to 10^{-9} (thin curves/marks), and compared to the analytical steady-state solutions (thick curves) described in Chapter 3.

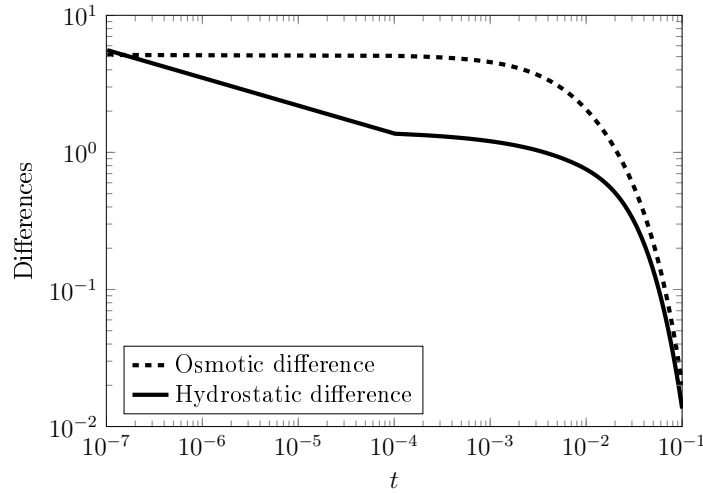


Figure 5.5: L_2 -norm of the difference between the transient numerical solution (obtained numerically with a spatial grid of 100 points, $\Delta t = 10^{-6} \cdot (\Delta x)^2$ and $\varepsilon = 0$) and the steady-state analytical solution for the two-layered model of both osmotic (dashed curve) and hydrostatic pressure (solid curve).

5.2.2 Time-dependent model

To study the transient nature of our mathematical model solved with the numerical scheme described in Section 5.1.6, we modify system (5.7) by assuming given pressure distributions $\hat{p}(r, t)$ and $\hat{\Pi}(r, t)$ and plugging them into it to obtain a source term vanishing only if the pressure distributions we have chosen are the exact solutions of the original problem (5.7). The modified problem can be stated as

$$\begin{cases} \alpha \frac{\partial \hat{p}}{\partial t} - \frac{1}{r + \xi} \frac{\partial}{\partial r} \left[(r + \xi) \ell_p \left(\frac{\partial \hat{p}}{\partial r} - \sigma \frac{\partial \hat{\Pi}}{\partial r} \right) \right] & = \hat{S}_1(r, t), \\ \frac{\partial \hat{\Pi}}{\partial t} + \frac{1}{r + \xi} \frac{\partial}{\partial r} \left[(r + \xi) \hat{\Pi} \left(A \frac{\partial \hat{p}}{\partial r} + B \frac{\partial \hat{\Pi}}{\partial r} \right) \right] & = \hat{S}_2(r, t). \end{cases} \quad (5.30)$$

By assuming the following distributions for the pressures

$$\begin{cases} \hat{p}(r, t) & = \sin(2\pi t) + \sin(2\pi r), \\ \hat{\Pi}(r, t) & = \sin(2\pi t) + \sin(2\pi r) + 5, \end{cases} \quad (5.31)$$

we can validate our problem, by choosing the initial/boundary conditions equal to equations (5.31) at the boundaries of the domain $[0, 10] \times [0, T)$, since they are the exact solutions of the modified system (5.30).

Note that the only change in the numerical implementation lies in the right-hand sides of the discretised equations (5.28), which become now equal to $S_1^{(i,n)} + 4(\Delta x)^2(r_i + \xi)\hat{S}_1(r_i, t^{n+1})$ and $S_2^{(i,n)} + 8(\Delta x)^2(r_i + \xi)\hat{S}_2(r_i, t^{n+1})$, respectively, where $S_1^{(i,n)}$ and $S_2^{(i,n)}$ are the source terms (5.29) of the previous discretised equations (5.28).

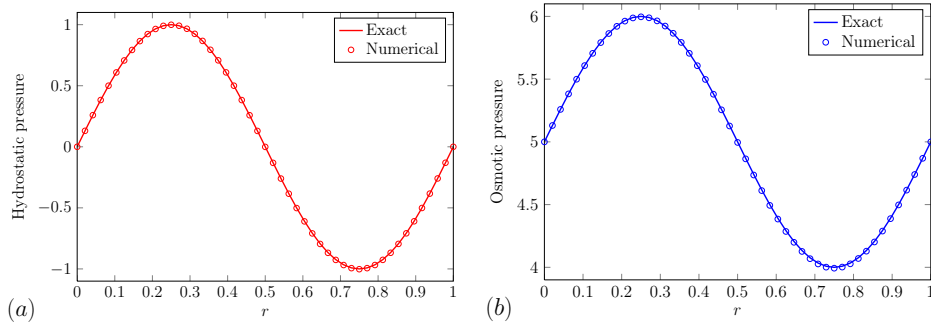


Figure 5.6: Hydrostatic (a) and osmotic (b) pressures of the modified problem for the two-layered model after one period ($t = 1$), obtained numerically with a spatial grid of 49 points, $\Delta t = (\Delta x)^2 = 4.3403 \cdot 10^{-4}$ and $\varepsilon = 10^{-2}$ (circles), and compared to exact solutions (solid curves).

Since equations (5.31) are periodic in t with period equal to 1, we evaluate the accuracy of Crank-Nicholson method by comparing the exact solutions

(solid curves) and the numerical solutions (circles) after one period, as depicted in Figure 5.6.

Mesh	Δx	Δt	L_∞ -error	L_1 -error	L_2 -error
7	0.166667	0.0277778	0.437544	0.284086	0.276584
13	0.0833333	0.00694444	0.116974	0.0636364	0.0682671
25	0.0416667	0.00173611	0.0299723	0.0175038	0.0178583
49	0.0208333	0.000434028	0.00734658	0.00463064	0.00446781
97	0.0104167	0.000108507	0.0018257	0.00118912	0.00112179

Table 5.2: L_p -norm errors of the numerical solutions obtained with different meshes at time $t = 1$, for the two-layered model and $\varepsilon = 10^{-2}$.

The behaviour of the error, computed as the L_p -norm of the difference between exact and numerical solutions at $t = 1$, for different meshes is reported in Table 5.2.

Mesh	Δx	Δt	L_∞ -order	L_1 -order	L_2 -order
13	0.0833333	0.00694444	1.90324	2.1584	2.01846
25	0.0416667	0.00173611	1.96448	1.86218	1.9346
49	0.0208333	0.000434028	2.02849	1.91838	1.99895
97	0.0104167	0.000108507	2.00862	1.96132	1.99377

Table 5.3: Empirical orders of accuracy computed from the different L_p -norm errors reported in Table 5.2 at time $t = 1$ for the two-layered model and $\varepsilon = 10^{-2}$.

Note that empirical orders of accuracy reported in Table 5.3 approach the theoretical order of accuracy of Crank-Nicholson method, which is second order. This happens even if we take $\Delta t = k(\Delta x)^2$ with k larger than 1, but smaller than $k = 1000$. Indeed, in the latter case the method is no longer convergent to the analytical solution.

5.3 An application: study of an hemorrhage

In this section we report the results of our simulations, starting from the comparison between the transient change in external pressures and the misleading assumption of constant extra-vascular pressures.

5.3.1 Initial/boundary conditions in dimensionless form

To solve numerically the *partial differential equation* (PDE) system (5.7) in the unknown functions $p = p(r, t)$ and $\Pi = \Pi(r, t)$, we prescribe the following

initial conditions

$$\begin{cases} p(r, 0) &= p^0(r), \\ \Pi(r, 0) &= \Pi^0(r), \end{cases} \quad (5.32)$$

where $p^0(r)$ and $\Pi^0(r)$ are the steady-state solutions of the *ordinary differential equation* (ODE) system obtained from system (5.7) by imposing zero time derivative of the pressures

$$\begin{cases} 0 &= \frac{d}{dr} \left[(r + \xi) \ell_p \left(\frac{dp}{dr} - \sigma \frac{d\Pi}{dr} \right) \right], \\ 0 &= \frac{d}{dr} \left[-(r + \xi) \Pi \left(A \frac{dp}{dr} + B \frac{d\Pi}{dr} \right) \right], \end{cases} \quad (5.33)$$

with boundary conditions given by (p_c^0, Π_c^0) and (p_o^0, Π_o^0) as in Table 5.1.

Moreover, in order to reach a steady situation after the alteration of the initial pressure and in order to have an accurate description of the changes in the fluxes with respect to the time, we impose an exit time of $T = 10$ (around 1.3 sec) and a fixed time step equal to $\Delta t = (\Delta x)^2$ (about 128 milliseconds), small if compared to the time scale.

Our aim is to simulate the experiment described in Levick and Michel (2010), so we abruptly (at a time $\hat{t} = 0.5T$) decrease the internal hydrostatic pressure from an initial value p_c^0 to a final value p_c^T , keeping the internal osmotic pressure constantly equal to Π_c^0 :

$$\begin{cases} p(r_c, t) &= p_c(t) &= p_c^0 + (p_c^T - p_c^0)H(t - \hat{t}), \\ \Pi(r_c, t) &= \Pi_c(t) &= \Pi_c^0, \end{cases} \quad (5.34)$$

where $H(x)$ is the *Heaviside step function* (see e.g. Kawamoto et al., 2011) defined as

$$H(x) = \begin{cases} 0, & x < 0, \\ 1/2, & x = 0, \\ 1, & x > 0. \end{cases} \quad (5.35)$$

Then we assume two different types of external boundary conditions, as depicted in Figure 5.7: the first one with constant values of the external pressures, namely

$$\begin{cases} p(r_o, t) &= p_o(t) &= p_o^0, \\ \Pi(r_o, t) &= \Pi_o(t) &= \Pi_o^0, \end{cases} \quad (5.36)$$

and the second one with the following physiological change in the external pressures, recovered qualitatively from Figure 3 in Levick and Michel (2010):

$$\begin{cases} p(r_o, t) &= p_o(t) &= p_o^0 - (p_o^T - p_o^0)H(t - \hat{t}) \left[e^{-\beta(t-\hat{t})} - 1 \right], \\ \Pi(r_o, t) &= \Pi_o(t) &= \Pi_o^0 - (\Pi_o^T - \Pi_o^0)H(t - \hat{t}) \left[e^{-\beta(t-\hat{t})} - 1 \right], \end{cases} \quad (5.37)$$

where

$$\beta = \frac{1}{\hat{t} - \tau} \text{W} \left(\frac{\hat{t} - \tau}{\Pi_o^T - \Pi_o^0} 10^{-1} \right) \quad (5.38)$$

controls the speed necessary to reach at time $\tau = 0.7T$ ($> \hat{t}$) “almost” constant external pressures¹, if the abrupt drop in the internal hydrostatic pressure occurs at $\hat{t} = 0.5T$. $\text{W}(x)$ is the *Lambert W function* (see e.g. Corless et al., 1996; Barry et al., 2000), also called *omega function* or *product logarithm*, which is the inverse function of $z \rightarrow z e^z$.

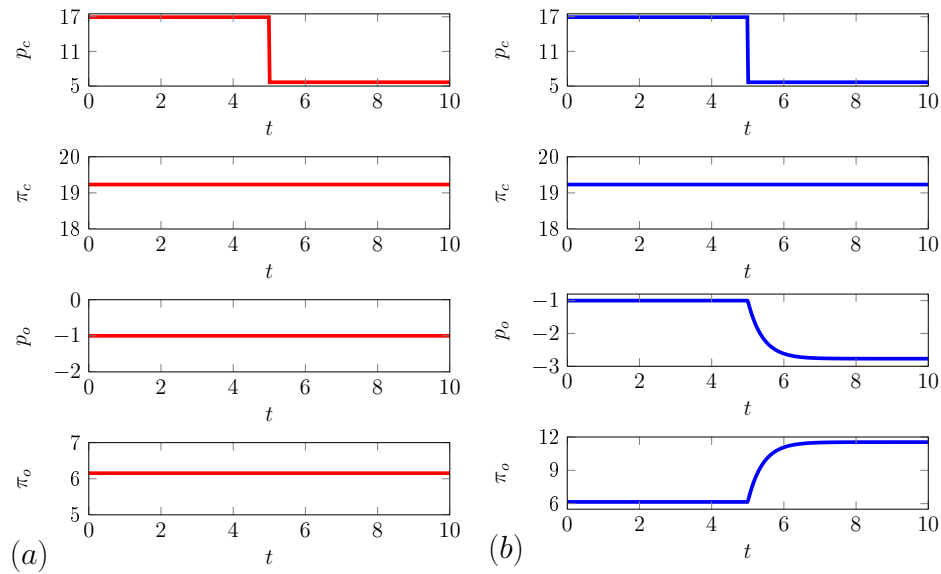


Figure 5.7: Behaviour of the boundary conditions, both for constant external pressures (a) as described in equations (5.34)-(5.37) and for pressures varying with time (b) and following equations (5.34)-(5.36).

5.3.2 How to model external pressures

We first consider a vessel wall composed by two homogeneous layers, with parameters varying gradually between them (namely $\varepsilon^2 = 10^{-4}$), to study the consequences on fluxes of the choice of constant external boundary conditions as in equations (5.36) or if we vary them following equations (5.37).

For $t \leq \hat{t}$, since external boundary conditions are the same both cases, there are no differences in the fluxes (see Figure 5.8), after choosing to solve

¹ In the sense that we impose that at $t = \tau$ the derivative of the external pressure function is “almost” zero, namely equal to a given tolerance (here the value prescribed was 10^{-1}).

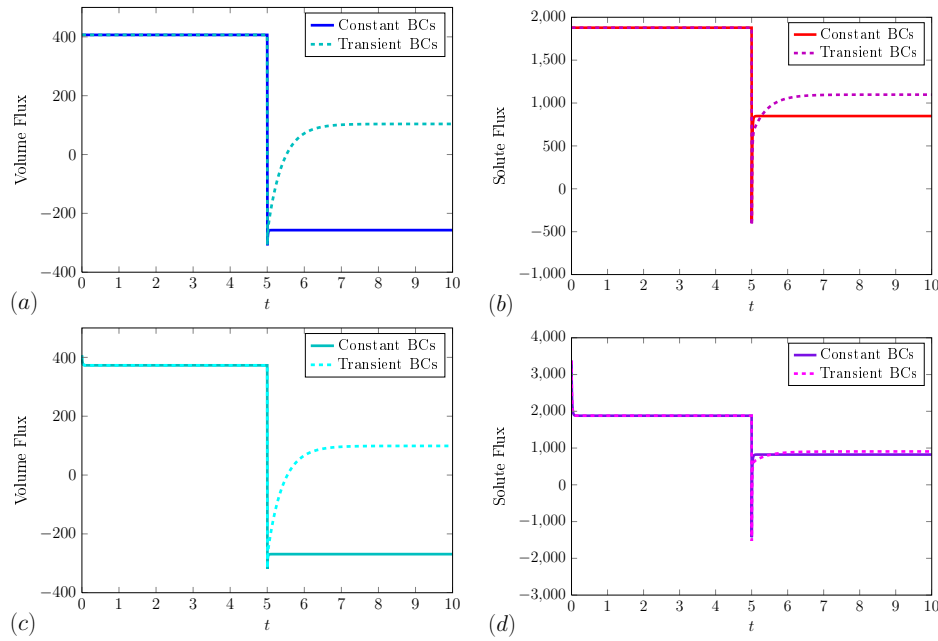


Figure 5.8: Behaviour of the mean volume (a)-(c) and solute (b)-(d) fluxes, reconstructed from both the complete non-linear system (a)-(b) and from the linearised problem described in Section 5.1.5 (c)-(d). The numerical solutions for the pressures were computed using a spatial grid of 100 points and $\Delta t = (\Delta x)^2$. The external pressures are assumed either constant as in equations (5.36) (solid curves) or varying with time following equations (5.37) (dashed curves).

either the complete problem or the linearised problem obtained from it as described in Section 5.1.5.

Note that the linearised problem has a steady-state solution different from that of the full problem, thus it takes some time ($\sim 0.02T$, namely around 26 milliseconds) to reach its own steady-state solution. In Section 5.1.5 are reported the steady-state solutions of the linearised problem both in the case of a single homogeneous layer, with equivalent parameters as described in Chapter 3, and in the case of a vessel wall composed by two layers with physical features varying discontinuously and taken from Table 5.1.

In Table 5.4 are reported the values of volume and solute fluxes, at some given times: (a) for $t = 0$, (b) immediately before the drop in luminal hydrostatic pressure, namely at $t = \hat{t}^-$, (c) immediately after p_c is reduced, namely at $t = \hat{t}^+$ and (d) at the exit time $t = T$.

The minimum is attained for $t = \hat{t}^+$ and is usually lower for the linearised problem compared to the full problem. At the exit time, solute flux is always

positive, even if considering constant external pressures it is lower (848.252 for the complete problem and 822.554 for the linearised problem) compared to external pressures varying following equations (5.37), where solute flux is equal to $J_s(T) = 1097.77$ for the complete problem and $J_s(T) = 907.579$ for the linearised problem. But we see the most relevant effects on the fluxes of the choice of external boundary conditions for $t > 0.5T$, namely after the abrupt drop in luminal hydrostatic pressure. As a matter of fact, over time the two fluxes do not increase with the same speed, neither they reach the same stationary value, as depicted in Figure 5.8. The latter is due to the fact that the final external boundary conditions are different, (p_o^T, Π_o^T) for transient BCs and (p_o^0, Π_o^0) in the constant case.

Mean volume flux

Layers	BCs	Problem	$t = 0$	$t = \hat{t}^-$	$t = \hat{t}^+$	$t = T$
2	Constant	Complete	406.57	406.57	-308.541	-257.008
2	Constant	Linearised	406.57	372.929	-318.758	-268.854
2	Transient	Complete	406.57	406.57	-306.794	103.93
2	Transient	Linearised	406.57	372.929	-316.765	98.995
1	Transient	Complete	406.57	406.57	-204.885	124.323
1	Transient	Linearised	406.57	406.57	-204.885	124.323

Mean solute flux

Layers	BCs	Problem	$t = 0$	$t = \hat{t}^-$	$t = \hat{t}^+$	$t = T$
2	Constant	Complete	1878.38	1878.38	-370.162	848.252
2	Constant	Linearised	3379.94	1880.08	-1426.91	822.554
2	Transient	Complete	1878.38	1878.38	-426.027	1097.77
2	Transient	Linearised	3379.94	1880.08	-1524.36	907.579
1	Transient	Complete	1878.72	1878.72	-2.79111	849.76
1	Transient	Linearised	1673.73	1670.06	107.945	689.012

Table 5.4: Mean volume and solute fluxes for certain times, both for the complete non-linear system and for the linearised problem described in Section 5.1.5. The numerical solutions for the pressures were computed using a spatial grid of 100 points and $\Delta t = (\Delta x)^2$. The external pressures are assumed either constant as in equations (5.36) or varying with time (transient BCs) following equations (5.37). The values of the fluxes are reported both for the two-layered model and for the single-layered model with equivalent dimensionless parameters equal to $\sigma^{eq} = 0.7987$, $\ell_p^{eq} = 0.8247$ and $\ell_d^{eq} = 0.5838$, following the procedure described in Chapter 3.

The main difference between the two approaches in the assumptions for the external pressure behaviour appears looking at the volume flux (see Table 5.4); as a matter of fact, for constant external pressure, after the drop in internal hydrostatic pressure which causing a decrease in volume flux taking negative values, the flux remains negative, being equal to $J_v(T) = -257.008$ and $J_v(T) = -268.854$ for the complete and linearised problem, respectively. The situation is different for external pressures varying in a physiological way, that is following equations (5.37). Indeed, after a transient decrease in volume flux immediately after internal hydrostatic pressure drop (where the flux becomes negative), the flux returns being positive, assuming at the exit time $t = T$ (positive) values, $J_v(T) = 103.93$ and $J_v(T) = 98.995$ for the complete and linearised problem, respectively. This confirms the description in Levick and Michel (2010) of a transient absorption, followed by a condition of steady filtration.

The linearised problem has a very similar behaviour to the full problem, but, in general, the flows assume lower values than those of the complete problem, except in the transition phases (at the beginning and immediately after the drop in internal hydrostatic pressure).

5.3.3 Comparison between the single- and two-layered models

We now consider transient external pressures varying following equations (5.37) and compare the single- and two-layered models.

As described in Chapter 3, the single-layered model is a simplification in which vessel wall is assumed as composed by an homogeneous material, with mean physical properties. They are obtained taking the mean of the reflection coefficient described in Sugihara-Seki and Fu (2005) and than imposing that at the initial time both volume and solute fluxes are the same either if reconstructed numerically (J_v^0 and J_s^0) using the two-layered model with discontinuous parameters (namely for $\varepsilon = 0$) or if computed using equivalent values of ℓ_p and ℓ_d (taken constant in the whole domain). The values used in the computations are the following:

$$\begin{aligned}
 \sigma_{eq} &= \frac{\ell_p^G \ell_p^W}{\ell_p^G + \ell_p^W} \left(\frac{\sigma_G}{\ell_d^G} + \frac{\sigma_W}{\ell_d^W} \right), \\
 \ell_p^{eq} &= -\frac{J_v^0}{2\pi} \frac{\ln(\xi) - \ln(1 + \xi)}{(p_c - p_o) - \sigma_{eq}(\Pi_c - \Pi_o)}, \\
 \ell_d^{eq} &= \ell_p^{eq} \sigma_{eq}^2 - \frac{1}{2\pi} \frac{(J_v^0)^2 (\sigma_{eq} - 1)^2 [\ln(\xi) - \ln(1 + \xi)]}{J_v^0 (\sigma_{eq} - 1) (\Pi_c - \Pi_o) - J_s^0 \ln \left(\frac{J_v^0 (\sigma_{eq} - 1) \Pi_c + J_s^0}{J_v^0 (\sigma_{eq} - 1) \Pi_o + J_s^0} \right)},
 \end{aligned} \tag{5.39}$$

where (p_c, Π_c) and (p_o, Π_o) are the initial values of the pressures at $r = 0$ and $r = 1$, respectively.

In Figure 5.9 the comparison of both fluxes between the single- (1L) and two-layered (2L) model are depicted. We may note that the fluxes obtained using the single-layered model are usually higher if compared to the ones obtained from the two-layered model, except from the initial solute flux of the linearised problem, which is far away from its steady-state value (see Table 5.4).

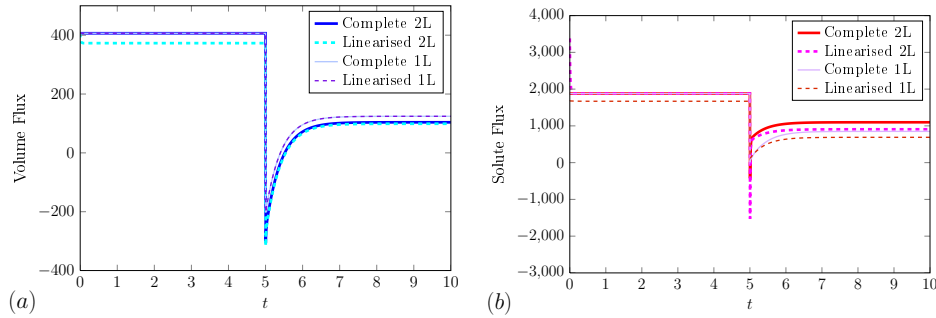


Figure 5.9: Comparison of the mean volume (a) and solute (b) fluxes, reconstructed from the full non-linear system (solid curves) and from the linearised problem described in Section 5.1.5 (dashed curves), for external pressures varying following equations (5.37). The numerical solutions for the pressures were computed using a spatial grid of 100 points and $\Delta t = (\Delta x)^2$. The fluxes obtained considering the two-layered model are depicted with thick curves, while the ones of the single-layered model are depicted with thin curves. The equivalent dimensionless parameters are assumed equal to $\sigma^{eq} = 0.7987$, $\ell_p^{eq} = 0.8247$ and $\ell_d^{eq} = 0.5838$.

Another important difference lies in the solute flux behaviour during the transition phase, in which slight ($J_s = -426.027$) or significant ($J_s = -1524.36$) absorption occurs in the two-layered model, depending on the problem considered (full or linearised, respectively). On the other hand, in the single-layered model extravasation happens for the linearised problem ($J_s = 107.945$), even if the internal hydrostatic pressures is dramatically reduced; while really slight absorption occurs for the full problem ($J_s = -2.79111$).

In Figures 5.10 and 5.11, the numerical solutions of the full PDE system (5.7) for the two- and single-layered model are depicted.

We may see that the behaviour of both hydrostatic and osmotic pressure is quite different in the two models. In particular, the decrease of both hydrostatic and osmotic pressures from the inner part of the domain to the outer part is more pronounced in the glycocalyx layer of the two-layered model. Moreover, even if the range of the pressures are totally similar in the

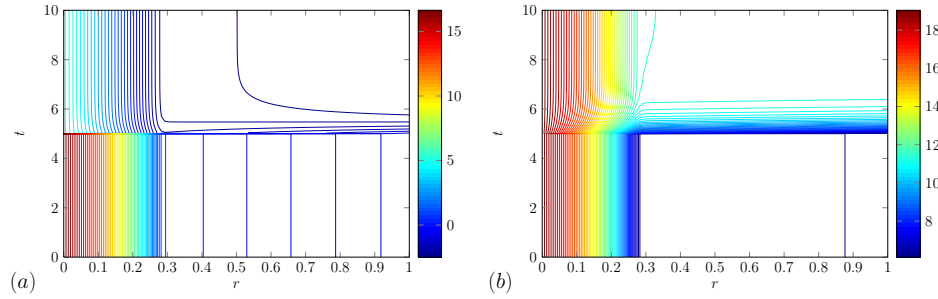


Figure 5.10: Hydrostatic (a) and osmotic (b) pressures obtained numerically with a spatial grid of 100 points and $\Delta t = (\Delta x)^2$ for the two-layered model, for external pressures varying following equations (5.37).

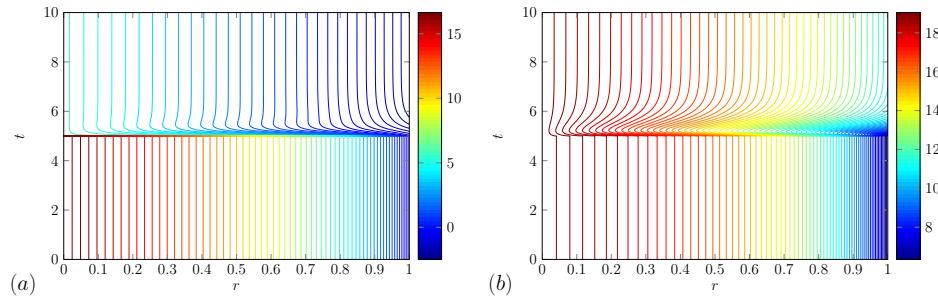


Figure 5.11: Hydrostatic (a) and osmotic (b) pressures obtained numerically with a spatial grid of 100 points and $\Delta t = (\Delta x)^2$ for the single-layered model, for external pressures varying following equations (5.37). The equivalent dimensionless parameters are assumed equal to $\sigma^{eq} = 0.7987$, $\ell_p^{eq} = 0.8247$ and $\ell_d^{eq} = 0.5838$.

two models, the dilution at the interface r_g , typical of the two-layered model, is absent in the single-layered model. Osmotic pressure at the interface between glycocalyx and endothelial layers can be significantly different from the extra-vascular osmotic pressure Π_o , being around 70 – 90% of Π_o under normal conditions of capillary pressure and filtration rate (Levick, 2010). The reason behind this phenomenon lies in the sieving effect of glycocalyx. Indeed, blood plasma passes through it, but proteins are blocked, demonstrated by the tremendous decrease of osmotic pressure in the glycocalyx layer, accompanied by a slight reduction in hydrostatic pressure in the same region (see Figures 5.10). Due to the high velocity of the fluid in the first region and the solute slow motion (due to diffusion) in the endothelial region (look at the small difference in the osmotic pressure between the interface r_g and the interstitial osmotic pressure Π_o at the initial time $t = 0$), plasma proteins are pushed outward and the current prevents them from going back by diffusion, thus creating a zone in which their concentration (and thus its

osmotic pressure) is lower.

A surprising finding is that dilution at the interface is not present in the full problem at the exit time, where osmotic pressure decreases monotonically. On the contrary, at the exit time, the linearised problem shows an osmotic pressure at the interface equal to 11.46, slightly lower than its value at $r = 1$, which is 11.54 (not shown here).

5.4 Conclusions

We have presented a one-dimensional multi-layered mathematical model, with filtration and transport differential equations strongly coupled and the solute flow being non-linear.

With our model, we have been able to provide a theoretical basis to confirm that a sudden drop in luminal hydrostatic pressure, as during hemorrhage, produces an initial transient absorption of interstitial fluid, followed by a gradual increase in both volume and solute flux until both of them assume positive values; this translates into steady filtration and solute extravasation under normal conditions of internal pressures.

This is a qualitative confirm of what stated in Levick and Michel (2010), also describing what happens in the transient phase, both in terms of pressure distribution in vessel wall and in terms of volume and solute fluxes across it.

We have also implemented a simplified model in which the PDE system is linear, giving reasonable steady fluxes, even if the description of the physical phenomenon in the transient phase is not so accurate. We have also compared this two-layered model with a single-layered model with equivalent parameters, noting that the results are significantly different from each other, even showing solute extravasation also in the transient phase of the single-layered model.

Chapter 6

Conclusions and further work

This dissertation focused on micro-filtration across microvessel wall in both stationary and transient conditions and considering the impact of blood pressure anomalies and damages of the cells composing the microvessel wall. Possible applications are in studying the origin of degenerative diseases and in drug delivery. For the purpose of mathematical modelling, the microvessel wall is idealised as a multi-layered membrane with material properties homogeneous within the single layer, but changing across the layers to represent the compartments with different specialisations. The application of the mass conservation principle for both solvent and solute under isothermal non-equilibrium thermodynamic conditions leads to a system of two differential conditions equations; the first is linear and represents mass conservation of the solvent, the second is non-linear and represents the conservation of the solute (macromolecule). The two equations are coupled through the osmotic pressure. This model is solved, numerically and when possible analytically, assuming radial symmetry, which is a reasonable assumption given the negligible compliance of microvessels.

Chapter 1 provides an overview of micro-vascular exchange system physiology, including the main anatomic features of blood microvessels. The assumptions adopted in the development of the mathematical model are justified on the basis of physiological properties. The permeability coefficients used to model the vessel wall have been defined and their distribution across vessel wall has been described.

A first simplified analysis is presented in Chapter 2, by neglecting the coupling of flow and transport equations. Despite this rather extreme simplification, the model reasonably describes filtration and macro-molecules transport across vessel wall, in the particular case of high pressures (as for arterial vessels or for pathological conditions of venous hypertension). This preliminary model has been used to explore the effects of hydrostatic pressure increase on fluid filtration and on the time needed for a single solute molecule to cross vessel wall. Indeed, this simplification permits to solve steady-state

flow and transport equations separately and to analyse the travel time of macro-molecules across the vessel wall, showing an increase of both plasma filtration and travel time with the hydrostatic blood pressure, which are in agreement with existing physiological studies.

Chapter 3, while still being a steady model, is a coupled model which allows for low pressures, by taking into account the modern view where flow absorption cannot occur in steady-state conditions unless luminal hydrostatic pressure drops below physiologically plausible values. This revised view describes a venous system continuously in a condition of slight filtration, which can absorb interstitial fluid and solute only transiently or in pathological conditions. This is contrary to common belief, where arterial vessels would be in a state of constant filtration of oxygen and nutrients, while venous vessels would continuously absorb carbon dioxide and waste products. Now, this reabsorption role of venous vessels has been recently disproven in favour of lymphatic system drainage and filtration both in arterial and in venous circulatory system, under physiological conditions. This new view of filtration among all blood vessels under physiological conditions, apart from being in qualitative agreement with experimental observations, is strengthened by the important and often neglected role of osmotic pressure induced by the colloidal plasma proteins, which strongly couples flow and transport equations one to each other. Despite the complexity of this ODE system describing transport processes, a mathematical analysis has been carried out obtaining analytical solutions for the hydrostatic and osmotic pressures in steady state under the assumption that the membrane properties are piece-wise constant, in agreement with experimental observations.

Microvessel wall description plays an important role in the mathematical model. Indeed, homogenising microvessel wall into a single-layered homogeneous membrane with equivalent properties leads to an unrealistic distribution of pressure across microvessel wall, not consistent with observations. Microvessel wall is a composite medium with the internal glycocalyx layer exerting a remarkable sieving effect on macromolecules, with respect to the external layer composed by the endothelial cells; we have represented its physiological structure through the superimposition of two homogeneous axially-symmetric membranes with different properties: the inner membrane representing the glycocalyx and the outer membrane standing for the surrounding endothelial cells. In the case of a composite vessel wall, comprising two membranes with discontinuous physical properties (and thus physiological parameters), the analytical solution of the coupled flow and transport equations, with the latter being non linear, has been reported. Also the case of smooth transition has been explored by using a suitable numerical scheme and the results of our model have been compared with others taken from the literature. A striking difference has been shown between the single- and two-layered models, with the first predicting much higher pressures at the interface between glycocalyx and endothelial cells and a gradual decline of

both pressures across microvessel wall, with a gradient increasing with the distance to account for the progressive increase of the surface crossed by the flows. On the other hand, the two-layered model has shown a smooth but steep decline of both hydrostatic and osmotic pressures within glycocalyx, due to the strong sieving effect that the glycocalyx exerts on macromolecules (modelled by using a reflection coefficient close to 1), such that only a very small fraction of them reaches the clefts. Then, due to the larger aperture of the clefts, macromolecules have been shown to move with small to negligible hindrance (represented by adopting a small reflection coefficient), as soon as they have crossed the glycocalyx. In particular, osmotic pressure has shown to decline rapidly across glycocalyx, reaching a minimum at the interface with endothelial cells and then increasing again to the value imposed as boundary condition at the external surface of microvessel. This dilution in the clefts just outside glycocalyx, which homogeneous single-layered models are unable to reproduce, is an important physiological mechanism, which has been indicated by Michel (1997) and Weinbaum (1998) as the cause preventing reversal steady-state flow (absorption) when capillary hydrostatic pressure was lowered to 10 – 15 cm H₂O (7.35 – 11.03 mmHg) in Landis' experiment (Landis, 1927). Concentration of macromolecules was small at the interface between glycocalyx and endothelial cells, resulting in an osmotic pressure smaller than in the interstitium, due to the high selectivity of glycocalyx. This feeds back to hydrostatic pressure, which also shows a strong decline within glycocalyx, followed by a mild reduction across endothelial cells. Hydrostatic pressure was not differentiable at the interface between the two layers, due to the discontinuity in material properties, but pressure gradient does not reverse across endothelial cells, as for osmotic pressure. Our two-layered model has resulted in proving that most of the pressures drop between lumen and interstitium occurs in the glycocalyx, confirming the importance of this hydrated gel in controlling flow and solute mass exchange (see e.g. Levick, 2010).

The results of our simulations have been discussed, emphasising the combined effect of glycocalyx and endothelial cells on controlling volumetric flow and solute mass transport across microvessel wall, which the single-layered model is unable to capture. The alterations of volumetric flux and solute mass flux, in case of a significant reduction of luminal hydrostatic pressure, have been in qualitative agreement with observed variations during detailed experiments reported in the literature. If the strong coupling between flow and transport equations is neglected, serious mistakes in quantification of volume and solute flows exiting microvessels may occur.

In Chapter 4 we have extensively applied the steady-state model presented in Chapter 3 to investigate the effects on exchange of fluid and macromolecules across a typical microvessel wall, both in the case of glycocalyx deterioration, either due to enzymatic digestion or to agonist recruitment, and in hypertensive zones such as pre- and post-stenotic blood vessels. Since

the fibre matrix of surface glycocalyx layer is located in the lumen side of microvessel, it has been recognised as crucial for micro-vascular wall homeostasis and has been shown to be more prone to be damaged than endothelial cells. Indeed, degradation and/or loss of glycocalyx have been shown at high shear-stress zones (such as at atherosclerosis-prone sites), during exposure to inflammatory stimuli, atherogenic/cardiovascular risk factors and in response to agonists such as adenosine. The effects of glycocalyx deterioration, either due to enzymatic digestion or to agonist recruitment, on plasma filtration and solute extravasation has been explored, by carefully justifying how to model the change in the physiological parameters describing glycocalyx structure and functions. Particular attentions has been devoted to correctly describe the relations among the transport parameters both in physiological and pathological conditions. What emerged has been that a seriously damaged glycocalyx produces an augmentation of flux of both solvent and solute, thus losing its role of transport barrier and macro-molecular sieve, as observed in the experiments of van den Berg et al. (2003). Analogously, the effects of capillary pressure increase, as in the case of hypertension, on both fluxes have been investigated, showing an augmentation of both volume and solute fluxes, in agreement with experimental results (Valenzuela-Rendon and Manning, 1990b,a). A physiological or pathological increment of blood pressure, as pre- and post-stenotic blood vessels, has been considered and studied also in concomitance with glycocalyx damage. The concurrence of glycocalyx degradation and hypertension has been shown to further raise plasma and solute fluxes, leading in most severe cases to oedema and hemorrhage, as in the case of diabetes.

Blood pressure continuously changes during time due to heart beat, nervous control and baro-reflexes, and is known to decrease along capillaries, thus reducing filtration rate. Under normal conditions, a well-perfused capillary is in a state of filtration along its entire length, but it can absorb fluid transiently when pressure falls (for instance, during hemorrhage and other forms of hypovolemia). A transient change in external pressures occurs, leading to decay in absorption and to restoration of a steady state of slight filtration. In fact, sub-glycocalyx plasma protein concentration increases as interstitial fluid is absorbed from a position between the glycocalyx and the endothelium, while interstitial pressure decreases as fluid is removed from interstitium, lowering the pressure exerted outside vessel wall. Two different sets of external pressures have been considered to investigate the effects of a sudden capillary pressure drop on transport processes: the first set of constant external pressures, while the other considering the change in interstitial pressure due to transient absorption of plasma and proteins. To take into account also the dynamic changes in trans-vascular flow in the case of transient pressures (as during hemorrhage), a time-dependent mathematical model of trans-vascular phenomena was needed. Thus, the time-dependent mathematical model of Chapter 5 has been developed to study this inter-

esting subject. The governing equations have been again obtained applying the mass conservation principle for both solvent and solute under isothermal non-equilibrium thermodynamic hypothesis. We have solved them using a finite-difference Crank-Nicolson numerical scheme, validating our model first through a test in which, imposing constant boundary conditions, the steady-state analytical solutions is reached in a finite time and then testing also the time-dependent nature of the model. With our time-dependent model, a theoretical basis has been provided to confirm that a sudden drop in luminal hydrostatic pressure, as during hemorrhage, produces an initial transient absorption of interstitial fluid, followed by a gradual increase in both volume and solute fluxes until both of them assume positive values; this translates into steady filtration and solute leakage under normal conditions of internal pressures, as described by Levick and Michel (2010). Thanks to this mathematical model, it has also been possible to describe quantitatively what happens in the transient phase, both in terms of pressure distribution across vessel wall and in terms of trans-vascular fluxes. Due to the simplicity, and thus efficiency of our model, all the simulations presented in this dissertation have been rather fast and have been providing results in line with physiological studies. Furthermore, the simulation tool may be useful for practical applications in physiological and medical studies, by evaluating the possible consequences of pathological conditions.

Among the potential further developments of the proposed model is a reformulation of the original time-dependent parabolic system through a relaxation parameter $\epsilon \ll 1$. We thus obtain an hyperbolic system eventually with a stiff source term, which provides the original parabolic equations in the limit as $\epsilon \rightarrow 0$. The advantage of this hyperbolised approach lies in the implementation of high-order, finite volume schemes with little effort, resulting in an increase of the efficiency of the numerical method used, since in general from an efficiency point of view, given a small target error, it is more convenient to increase the order of accuracy of a scheme than to refine the mesh to compute solutions more accurately. Another natural development of the proposed trans-vascular model is its coupling to haemodynamics, since plasma filtration and solute transport are closely linked to local blood flow dynamics. As a matter of fact, it has been observed that vessel occlusion, resulting in anomalous blood flow and hypertension, is associated with the tendency to oedema formation and perivascular accumulation of material (see for instance Mayhan and Heistad, 1985, 1986; Singh and Zamboni, 2009). The aim of trans-vascular transport studies is to determine the influence of disturbed flow patterns first on luminal pressure and then on the local concentration of substances both in the lumen and in the vessel wall. Another fundamental issue lies in the development of a model that includes more than two layers, necessary to accurately describe plasma and solute transport across cerebral vessel walls (composing the blood-brain barrier), which are characterised by three additive external layers: the pericytes,

the basement membrane and the astrocyte feet (Hawkins and Davis, 2005). This would result in a better understanding of neuro-degenerative conditions which seem to be connected to vascular and/or transport anomalies, such as Parkinson's disease, Alzheimer's disease and multiple sclerosis (Hawkins and Davis, 2005; Li et al., 2010). Drug delivery in the treatment of diseases could also be explored and potentially optimised by extending the current models. All these are very controversial issues in which accurate mathematical modelling may provide a starting point in new medical research fields.

List of quantities and their dimension

Symbol	Dimension	Quantity name
p	$ML^{-1}T^{-2}$	hydrostatic pressure
Π	$ML^{-1}T^{-2}$	osmotic pressure
c	NL^{-3}	macro-molecular molar solute concentration
q_v	LT^{-1}	specific volume discharge
q_s	$NL^{-2}T^{-1}$	specific solute discharge through the capillary wall
J_v	L^2T^{-1}	volume flux per unit length of vessel
J_s	$NT^{-1}L^{-1}$	solute flux per unit length of vessel
ℓ_p	TL^3M^{-1}	hydraulic conductivity of a membrane
ℓ_d	TL^3M^{-1}	diffusional permeability of a membrane
σ	1	reflection coefficient
φ	1	partition coefficient
ρ	ML^{-3}	density of the fluid
g	LT^{-2}	gravitational acceleration
S_s	L^{-1}	(volumetric) specific storage
R	$ML^2N^{-1}\Theta^{-1}T^{-2}$	gas constant
T	Θ	absolute temperature
D_{free}	L^2T^{-1}	free diffusion coefficient
L_p	TL^2M^{-1}	hydraulic conductivity of the capillary wall
P_d	LT^{-1}	diffusional permeability to a particular solute
Δr	L	capillary wall thickness
ℓ_G	L	glycocalyx thickness
r_c	L	capillary radius
r_g	L	radius of the interface between glycocalyx and endothelium
r_o	L	external radius of the vessel wall
p_c	$ML^{-1}T^{-2}$	capillary hydrostatic pressure
p_o	$ML^{-1}T^{-2}$	interstitial hydrostatic pressure
Π_c	$ML^{-1}T^{-2}$	capillary osmotic pressure
Π_o	$ML^{-1}T^{-2}$	interstitial osmotic pressure
σ_G	1	glycocalyx reflection coefficient
σ_W	1	endothelial cells reflection coefficient
ℓ_p^G	TL^3M^{-1}	glycocalyx hydraulic conductivity
ℓ_p^W	TL^3M^{-1}	endothelial cells hydraulic conductivity
ℓ_d^G	TL^3M^{-1}	glycocalyx diffusional permeability
ℓ_d^W	TL^3M^{-1}	endothelial cells diffusional permeability

Table 1: Notation and dimensions of the quantities. L is the length, T is the time, M is the mass, Θ is the temperature and N is the number of moles.

Bibliography

- Adamson, R., 1990. Permeability of frog mesenteric capillaries after partial pronase digestion of the endothelial glycocalyx. *The Journal of Physiology* 428, 1–13. [cited at p. 47, 54, 55]
- Adamson, R., Lenz, J., Zhang, X., Adamson, G., Weinbaum, S., Curry, F., 2004. Oncotic pressures opposing filtration across non-fenestrated rat microvessels. *Journal of Physiology* 557 (3), 889–907. [cited at p. xxii, xxiii, 21, 31, 44, 54, 70]
- Ai, L., Vafai, K., 2006. A coupling model for macromolecule transport in a stenosed arterial wall. *International Journal of Heat and Mass Transfer* 49 (9–10), 1568–1591. [cited at p. xxiii]
- Arkill, K., Neal, C., Mantell, J., Michel, C., Qvortrup, K., Rostgaard, J., Bates, D., Knupp, C., Squire, J., 2012. 3D reconstruction of the glycocalyx structure in mammalian capillaries using electron tomography. *Microcirculation* 19, 343–351. [cited at p. 2, 47]
- Barry, D., Parlange, J., Li, L., Prommer, H., Cunningham, C., Stagnitti, F., 2000. Analytical approximations for real values of the Lambert W-function. *Mathematics and Computers in Simulation* 53, 95–103. [cited at p. 27, 79]
- Bennett, H., 1963. Morphological aspects of extracellular polysaccharides. *Journal of Histochemistry & Cytochemistry* 11, 14–23. [cited at p. 3]
- Boron, W., Boulpaep, E., 2005. *Medical Physiology*. Saunders Elsevier, Philadelphia. [cited at p. xv, 18]
- Bundgaard, M., 1984. The three-dimensional organization of tight junctions in a capillary endothelium revealed by serial-section electron microscopy. *Journal of Ultrastructure Research* 88 (1), 1–17. [cited at p. 48]
- Carew, T., Vaishnav, R., Patel, D., 1968. Compressibility of the arterial wall. *Circulation Research* 23 (1), 61–68. [cited at p. 70]
- Charm, S., Kurland, G., 1974. *Blood Flow and Microcirculation*. Wiley, New York. [cited at p. 31, 54, 70]

- Chobanian, A., Bakris, G., Black, H., Cushman, W., Green, L., Izzo, J., Jones, D., Materson, B., Oparil, S., Wright, J., Roccella, E., the National High Blood Pressure Education Program Coordinating Committee, 2003. Seventh report of the Joint National Committee on prevention, detection, evaluation, and treatment of high blood pressure. *Hypertension* 42 (6), 1206–1252. [cited at p. 48, 58]
- Constantinescu, A., Spaan, J., Arkenbout, E., Vink, H., VanTeeffelen, J., 2011. Degradation of the endothelial glycocalyx is associated with chylomicron leakage in mouse cremaster muscle microcirculation. *Thrombosis and Haemostasis* 105, 790–801. [cited at p. 48]
- Constantinescu, A., Vink, H., Spaan, J., 2003. Endothelial cell glycocalyx modulates immobilization of leukocytes at the endothelial surface. *Arteriosclerosis, Thrombosis, and Vascular Biology* 23, 1541–1547. [cited at p. 47]
- Corless, R., Gonnet, G., Hare, D., Jeffrey, D., Knuth, D., 1996. On the Lambert W function. *Advances in Computational Mathematics* 5, 329–359. [cited at p. 27, 79]
- Curry, F., Michel, C., 1980. A fiber matrix model of capillary permeability. *Microvascular Research* 20 (1), 96–99. [cited at p. 48]
- Donati, A., Damiani, E., Domizi, R., Romano, R., Adrario, E., Pelaia, P., Ince, C., Singer, M., 2013. Alteration of the sublingual microvascular glycocalyx in critically ill patients. *Microvascular Research* S0026-2862 (13), 00149–0. [cited at p. 48]
- Facchini, L., Bellin, A., Toro, E., 2013a. Modelling the combined effects on plasma filtration and solute exchange of glycocalyx deterioration and/or hypertension, in preparation. [cited at p. 47]
- Facchini, L., Bellin, A., Toro, E., July 2013b. A new model of filtration and macromolecules transport across capillary walls, submitted to *Journal of Mathematical Biology*.
URL <http://arxiv.org/abs/1308.1271> [cited at p. 21, 70]
- Facchini, L., Bellin, A., Toro, E., 2013c. A simple model of filtration and macromolecule transport through microvascular walls. In: Vázquez-Cendón, M., Hidalgo, A., García-Navarro, P., Cea, L. (Eds.), *Numerical Methods for Hyperbolic Equations: Theory and Applications*. An international conference to honour Professor E.F. Toro. Vol. 23. CRC Press, Taylor-Francis Group, Santiago de Compostela, pp. 339–346, ISBN 978-0-415-62150-2, arxiv:1308.1328.
URL <http://arxiv.org/abs/1308.1328> [cited at p. 9]

- Facchini, L., Bellin, A., Toro, E., 2013d. A time-dependent mathematical model of filtration and solute exchange. application to the study of hemorrhage, in preparation. [cited at p. 63]
- Florian, J., Kosky, J., Ainslie, K., Pang, Z., Dull, R., Tarbell, J., 2003. Heparan sulfate proteoglycan is a mechanosensor on endothelial cells. *Circulation Research* 93, e136–e142. [cited at p. 47]
- Formaggia, L., Quarteroni, A., Veneziani, A., 2009. *Cardiovascular Mathematics*. Springer, Milan. [cited at p. xxii]
- Freeze, R., 1975. A stochastic-conceptual analysis of one-dimensional groundwater flow in nonuniform homogeneous media. *Water Resources Research* 11 (5), 725–741. [cited at p. 32, 50, 73]
- Fu, B., Chen, B., Chen, W., 2003. An electrodiffusion model for effects of surface glycocalyx layer on microvessel permeability. *American Journal of Physiology - Heart and Circulatory Physiology* 284 (4), H1240–H1250. [cited at p. 49, 65]
- Fu, B., Weinbaum, S., Tsay, R., Curry, F., 1994. A junction-orifice-fiber entrance layer model for capillary permeability: Application to frog mesenteric capillaries. *Journal of Biomechanical Engineering* 116, 502–513. [cited at p. 21, 48, 49]
- Haacke, E., Cheng, N., House, M., Liu, Q., Neelavalli, J., Ogg, R., Khan, A., Ayaz, M., Kirsch, W., Obenaus, A., 2005. Imaging iron stores in the brain using magnetic resonance imaging. *Magnetic Resonance Imaging* 23 (1), 1–25. [cited at p. 4]
- Hawkins, B., Davis, T., 2005. The blood-brain barrier/neurovascular unit in health and disease. *Pharmacological Reviews* 57 (2), 173–185. [cited at p. 3, 4, 92]
- Henry, C., Duling, B., 1999. Permeation of the luminal capillary glycocalyx is determined by hyaluronan. *American Journal of Physiology* 277, H508–H514. [cited at p. 47]
- Hildebrand, F., 1987. *Introduction to Numerical Analysis*. Dover Publications. [cited at p. 27, 33]
- Hu, X., Adamson, R., Liu, B., Curry, F., Weinbaum, S., 2000. Starling forces that oppose filtration after tissue oncotic pressure is increased. *American Journal of Physiology - Heart and Circulatory Physiology* 279 (4), H1724–H1736. [cited at p. xxiii, 21]
- Hu, X., Weinbaum, S., 1999. A new view of Starling’s hypothesis at the microstructural level. *Microvascular Research* 58, 281–304. [cited at p. 31, 70]

- Huxley, V., Williams, D., 2000. Role of a glycocalyx on coronary arteriole permeability to proteins: Evidence from enzyme treatments. *American Journal of Physiology - Heart and Circulatory Physiology* 278, H1177–H1185. [cited at p. 47]
- Intaglietta, M., Johnson, P., Winslow, R., 1996. Microvascular and tissue oxygen distribution. *Cardiovascular Research* 32, 632–643. [cited at p. 22]
- Jeansson, M., Haraldsson, B., 2003. Glomerular size and charge selectivity in the mouse after exposure to glucosaminoglycan-degrading enzymes. *Journal of the American Society of Nephrology* 14, 1756–1765. [cited at p. 47]
- Jensen, J., Feldt-Rasmussen, B., Borch-Johnsen, K., Jensen, K., Nordestgaard, B., 2005. Increased transvascular lipoprotein transport in diabetes: Association with albuminuria and systolic hypertension. *The Journal of Clinical Endocrinology and Metabolism* 90 (8), 4441–4445. [cited at p. 58]
- Katchalsky, A., Curran, P., 1965. *Non-equilibrium Thermodynamics in Biophysics*. Harvard Univ. Press. [cited at p. 22, 23, 31, 51, 65]
- Katz, M., 1985. New formulation of water and macromolecular flux which corrects for non-ideality: Theory and derivation, predictions, and experimental results. *Journal of Theoretical Biology* 112 (2), 369–401. [cited at p. 68]
- Kawamoto, A., Matsumori, T., Yamasaki, S., Nomura, T., Kondoh, T., S., N., 2011. Heaviside projection based topology optimization by a PDE-filtered scalar function. *Structural and Multidisciplinary Optimization* 44 (1), 19–24. [cited at p. 78]
- Kedem, O., Katchalsky, A., 1958. Thermodynamic analysis of the permeability of biological membranes to non-electrolytes. *Biochimica et Biophysica Acta* 27 (2), 229–246. [cited at p. xxii]
- Khakpour, M., Vafai, K., 2008a. Analysis of transport phenomena within PEM fuel cells – An analytical solution. *International Journal of Heat and Mass Transfer* 51, 3712–3723. [cited at p. xxiii]
- Khakpour, M., Vafai, K., 2008b. A comprehensive analytical solution of macromolecular transport within an artery. *International Journal of Heat and Mass Transfer* 51, 2905–2913. [cited at p. xxiii]
- Khakpour, M., Vafai, K., 2008c. Critical assessment of arterial transport models. *International Journal of Heat and Mass Transfer* 51, 807–822. [cited at p. xxiii]
- Khakpour, M., Vafai, K., 2008d. Effects of gender-related geometrical characteristics of aorta-iliac bifurcation on hemodynamics and macromolecule

- concentration distribution. *International Journal of Heat and Mass Transfer* 51, 5542–5551. [cited at p. xxiii]
- Landis, E., 1927. Micro-injection studies of capillary permeability. II. The relation between capillary pressure and the rate at which fluid passes through the walls of single capillaries. *American Journal of Physiology* 82 (2), 217–238. [cited at p. 39, 64, 89]
- Landis, E., 1932. Factors controlling the movement of fluid through the human capillary wall. *Yale Journal of Biology and Medicine* 5 (3), 201–225. [cited at p. 10, 19, 21, 43]
- Landis, E., Pappenheimer, J., 1963. Exchange of substances through the capillary walls. In: Hamilton, W., Dow, P. (Eds.), *Handbook of physiology. A critical, comprehensive presentation of physiological knowledge and concepts. Circulation. Vol. 2.* Washington DC, American Physiological Society, Ch. 29, pp. 961–1034. [cited at p. 67]
- Levick, J., 1991. Capillary filtration-absorption balance reconsidered in light of dynamic extravascular factors. *Experimental Physiology* 76, 825–857. [cited at p. 31, 54]
- Levick, J., 2010. *An Introduction To Cardiovascular Physiology.* CRC Press. [cited at p. xxi, xxii, xxiii, 1, 2, 3, 7, 10, 18, 21, 22, 23, 40, 60, 63, 64, 65, 66, 67, 84, 89]
- Levick, J., Michel, C., 2010. Microvascular fluid exchange and the revised Starling principle. *Cardiovascular Research* 87 (2), 198–210. [cited at p. xxiii, xxv, 10, 39, 40, 45, 51, 54, 63, 64, 65, 70, 78, 82, 85, 91]
- Levick, J., Mortimer, P., 1999. Fluid ‘balance’ between microcirculation and interstitium in skin and other tissues: Revision of the classical filtration-reabsorption scheme. In: Messmer, K. (Ed.), *Microcirculation in chronic venous insufficiency. Progress in Applied Microcirculation. Vol. 23.* Karger S., pp. 42–62. [cited at p. 40]
- Li, G., Yuan, W., Fu, B., 2010. A model for the blood-brain barrier permeability to water and small solutes. *Journal of Biomechanics* 43 (11), 2133–2140. [cited at p. 4, 54, 92]
- Marechal, X., Favory, R., Joulin, O., Montaigne, D., Hassoun, S., Decoster, B., Zerimech, F., Neviere, R., 2008. Endothelial glycocalyx damage during endotoxemia coincides with microcirculatory dysfunction and vascular oxidative stress. *Shock* 29 (5), 572–576. [cited at p. 48]
- Martens, R., Vink, H., van Oostenbrugge, R., Staals, J., 2013. Sublingual microvascular glycocalyx dimensions in lacunar stroke patients. *Cerebrovascular Diseases* 35 (5), 451–454. [cited at p. 48]

- Mayhan, W., Heistad, D., 1985. Permeability of blood-brain barrier to various sized molecules. *American Journal of Physiology - Heart and Circulatory Physiology* 248, H712–H718. [cited at p. 91]
- Mayhan, W., Heistad, D., 1986. Role of veins and cerebral venous pressure in disruption of the blood-brain barrier. *Circulation Research* 59, 216–220. [cited at p. 58, 91]
- Michel, C., 1980. Filtration coefficients and osmotic reflexion coefficients of the walls of single frog mesenteric capillaries. *Journal of Physiology* 309, 341–355. [cited at p. 17]
- Michel, C., 1996. Transport of macromolecules through microvascular walls. *Cardiovascular Research* 32 (4), 644–653. [cited at p. 1]
- Michel, C., 1997. Starling: The formulation of his hypothesis of microvascular fluid exchange and its significance after 100 years. *Experimental Physiology* 82 (1), 1–30. [cited at p. xxiv, 21, 39, 43, 44, 64, 89]
- Michel, C., Curry, F., 1999. Microvascular permeability. *Physiological Reviews* 79 (3), 703–761. [cited at p. 5, 17, 23, 49, 65]
- Michel, C., Phillips, M., 1987. Steady-state fluid filtration at different capillary pressures in perfused frog mesenteric capillaries. *Journal of Physiology* 388, 421–435. [cited at p. 31, 70]
- Milton, G., 2002. *Theories of Composites*. Cambridge University Press, Cambridge. [cited at p. 38]
- Mochizuki, S., Vink, H., Hiramatsu, O., Kajita, T., Shigeto, F., Spaan, J., Kajiya, F., 2003. Role of hyaluronic acid glycosaminoglycans in shear-induced endothelium-derived nitric oxide release. *American Journal of Physiology - Heart and Circulatory Physiology* 285, H722–H726. [cited at p. 47, 48]
- Mulivor, A., Lipowsky, H., 2004. Inflammation- and ischemia-induced shedding of venular glycocalyx. *American Journal of Physiology - Heart and Circulatory Physiology* 286 (5), H1672–H1680. [cited at p. 48]
- Nieuwdorp, M., Holleman, F., de Groot, E., Vink, H., Gort, J., Kontush, A., Chapman, M., Hutten, B., Brouwer, C., Hoekstra, J., Kastelein, J., Stroes, E., 2007. Perturbation of hyaluronan metabolism predisposes patients with type 1 diabetes mellitus to atherosclerosis. *Diabetologia* 50 (6), 1288–1293. [cited at p. 48]
- Nieuwdorp, M., Mooij, H., Kroon, J., Atasever, B., Spaan, J., Ince, C., Holleman, F., Diamant, M., Heine, R., Hoekstra, J., Kastelein, J., Stroes,

- E., Vink, H., 2006. Endothelial glycocalyx damage coincides with microalbuminuria in type 1 diabetes. *Diabetes* 55 (4), 1127–1132. [cited at p. 48, 53, 58]
- Pappenheimer, J., Soto-Rivera, A., 1948. Effective osmotic pressure of the plasma proteins and other quantities associated with the capillary circulation in the hindlimbs of cats and dogs. *American Journal of Physiology* 152 (3), 471–491. [cited at p. 64]
- Patlak, C., Goldstein, D., Hoffman, J., 1963. The flow of solute and solvent across a two-membrane system. *Journal of Theoretical Biology* 5 (3), 426–442. [cited at p. 65]
- Prosi, M., Zunino, P., Perktold, K., Quarteroni, A., 2005. Mathematical and numerical models for transfer of low-density lipoproteins through the arterial walls: A new methodology for the model set up with applications to the study of disturbed luminal flow. *Journal of Biomechanics* 38, 903–917. [cited at p. xxij]
- Renkin, E., 1954. Filtration, diffusion, and molecular sieving through porous cellulose membranes. *The Journal of General Physiology* 38 (2), 225–243. [cited at p. 51]
- Robinson, T., 03 1988. Arterial graft prosthesis.
URL http://www.patentlens.net/patentlens/patent/US_4731073/en/ [cited at p. 17, 70]
- Schmidt, E., Yang, Y., Janssen, W., Gandjeva, A., Perez, M., Barthel, L., Zemans, R., Bowman, J., Koyanagi, D., Yunt, Z., Smith, L., Cheng, S., Overdier, K., Thompson, K., Geraci, M., Douglas, I., Pearse, D., Tudor, R., 2012. The pulmonary endothelial glycocalyx regulates neutrophil adhesion and lung injury during experimental sepsis. *Nature Medicine* 18 (8), 1217–1223. [cited at p. 56]
- Silverthorn, D., 2009. *Human Physiology: An Integrated Approach*. Pearson Education, Inc. [cited at p. xxi, 17, 63]
- Singh, A., Ramnath, R., Foster, R., Wylie, E., Fridèn, V., Dasgupta, I., Haraldsson, B., Welsh, G., Mathieson, P., Satchell, S., 2013. Reactive oxygen species modulate the barrier function of the human glomerular endothelial glycocalyx. *PLoS One* 8 (2), e55852. [cited at p. 48, 56]
- Singh, A., Satchell, S., Neal, C., McKenzie, E., Tooke, J., Mathieson, P., 2007. Glomerular endothelial glycocalyx constitutes a barrier to protein permeability. *Journal of the American Society of Nephrology* 18 (11), 2885–2893. [cited at p. 48, 56]

- Singh, A., Zamboni, P., 2009. Anomalous venous blood flow and iron deposition in multiple sclerosis. *Journal of Cerebral Blood Flow and Metabolism* 29 (12), 1867–1878. [cited at p. 4, 91]
- Speziale, S., Sivaloganathan, S., 2009. Poroelastic theory of transcapillary flow: Effects of endothelial glycocalyx deterioration. *Microvascular Research* 78, 432–441. [cited at p. 49]
- Speziale, S., Tenti, G., Sivaloganathan, S., 2008. A poroelastic model of transcapillary flow in normal tissue. *Microvascular Research* 75 (2), 285–295. [cited at p. 31, 42, 44, 45, 51, 54, 66, 70]
- Squire, J., Chew, M., Nneji, G., Neal, C., Barry, J., Michel, C., 2001. Quasi-periodic substructure in the microvessel endothelial glycocalyx: A possible explanation for molecular filtering? *Journal of Structural Biology* 136 (3), 239–255. [cited at p. xxii, 2, 47, 49, 52]
- Sriram, K., Vazquez, B., Yalcin, O., Johnson, P., Intaglietta, M., Tarkovsky, D., 2011. The effect of small changes in hematocrit on nitric oxide transport in arterioles. *Antioxidants and Redox Signaling* 14, 175–185. [cited at p. 22]
- Starling, E., 1896. On the absorption of fluids from the connective tissue spaces. *Journal of Physiology* 19 (4), 312–326. [cited at p. xxi, 64]
- Stevens, A., Hlady, V., Dull, R., 2007. Fluorescence correlation spectroscopy can probe albumin dynamics inside lung endothelial glycocalyx. *American Journal of Physiology - Lung Cellular and Molecular Physiology* 293 (2), L328–L335. [cited at p. 54]
- Sugihara-Seki, M., Akinaga, T., Itano, T., 2008. Flow across microvessel walls through the endothelial surface glycocalyx and the interendothelial cleft. *Journal of Fluid Mechanics* 601, 229–252. [cited at p. xxi, xxii, 45]
- Sugihara-Seki, M., Fu, B., 2005. Blood flow and permeability in microvessels. *Fluid Dynamics Research* 37, 82–132. [cited at p. xxi, 1, 2, 7, 38, 49, 65, 67, 69, 82]
- Taylor, G., 1953. Dispersion of soluble matter in solvent flowing slowly through a tube. *Proceedings of the Royal Society of London. Series A, Mathematical and Physical Sciences* 219 (1137), 186–203. [cited at p. 52]
- Tsay, R., Weinbaum, S., 1991. Viscous flow in a channel with periodic cross-bridging fibres: Exact solutions and brinkman approximation. *Journal of Fluid Mechanics* 226, 125–148. [cited at p. 48]
- Turner, M., Clough, G., Michel, C., 1983. The effects of cationised ferritin and native ferritin upon the filtration coefficient of single frog capillaries. Evidence that proteins in the endothelial cell coat influence permeability. *Microvascular Research* 25 (2), 205–222. [cited at p. xxi, 21]

- Urick, R., 1947. A sound velocity method for determining the compressibility of finely divided substances. *Journal of Applied Physics* 18 (11), 983–987. [cited at p. 70]
- Valenzuela-Rendon, J., Manning, R., 1990a. Chronic lymph flow and transcapillary fluid flux during angiotensin II hypertension. *American Journal of Physiology* 259, R1205–R1213. [cited at p. 60, 90]
- Valenzuela-Rendon, J., Manning, R., 1990b. Chronic transvascular fluid flux and lymph flow during volume-loading hypertension. *American Journal of Physiology* 258, H1524–H1533. [cited at p. 60, 90]
- van den Berg, B., Spaan, J., Rolf, T., Vink, H., 2006. Atherogenic region and diet diminish glycocalyx dimension and increase intima-to-media ratios at murine carotid artery bifurcation. *American Journal of Physiology - Heart and Circulatory Physiology* 290, H915–H920. [cited at p. 48, 54]
- van den Berg, B., Vink, H., Spaan, J., 2003. The endothelial glycocalyx protects against myocardial edema. *Circulation Research* 92, 592–594. [cited at p. xxiv, 47, 54, 56, 90]
- VanTeeffelen, J., Brands, J., Stroes, E., Vink, H., 2007. Endothelial glycocalyx: Sweet shield of blood vessels. *Trends in Cardiovascular Medicine* 17, 101–105. [cited at p. 2, 3, 47, 48, 53, 54, 65]
- VanTeeffelen, J., Dekker, S., Fokkema, D., Siebes, M., Vink, H., Spaan, J., 2005. Hyaluronidase treatment of coronary glycocalyx increases reactive hyperemia but not adenosine hyperemia in dog hearts. *American Journal of Physiology - Heart and Circulatory Physiology* 289, H2508–H2513. [cited at p. 53]
- Vink, H., Duling, B., 2000. Capillary endothelial surface layer selectively reduces plasma solute distribution volume. *American Journal of Physiology - Heart and Circulatory Physiology* 278 (1), H285–H289. [cited at p. 52]
- Vlahu, C., Lemkes, B., Struijk, D., Koopman, M., Krediet, R., Vink, H., 2012. Damage of the endothelial glycocalyx in dialysis patients. *Journal of the American Society of Nephrology* 23, 1900–1908. [cited at p. 48]
- Ward, B., Bauman, K., Firth, J., 1988. Interendothelial junctions of cardiac capillaries in rats: Their structure and permeability properties. *Cell and Tissue Research* 252 (1), 57–66. [cited at p. 48]
- Weinbaum, S., 1998. 1997 Whitaker distinguished lecture: Models to solve mysteries in biomechanics at the cellular level; A new view of fiber matrix layers. *Annals of Biomedical Engineering* 26 (4), 627–643. [cited at p. xxiv, 21, 39, 43, 44, 64, 89]

- Weinbaum, S., Tarbell, J., Damiano, E., 2007. The structure and function of the endothelial glycocalyx layer. *Annual Review of Biomedical Engineering* 9, 121–167. [cited at p. 47]
- Weinbaum, S., Tsay, R., Curry, F., 1992. A three-dimensional junction-pore-matrix model for capillary permeability. *Microvascular Research* 44 (1), 85–111. [cited at p. 48]
- Weinbaum, S., Zhang, X., Han, Y., Vink, H., Cowin, S., 2003. Mechanotransduction and flow across the endothelial glycocalyx. *Proceedings of the National Academy of Sciences USA* 100, 7988–7995. [cited at p. xxii, 3, 49]
- Yang, Y., Schmidt, E., 2013. The endothelial glycocalyx: An important regulator of the pulmonary vascular barrier. *Tissue Barriers* 1 (1), e23494. [cited at p. 56]
- Zamboni, P., Galeotti, R., Menegatti, E., Malagoni, A., Tacconi, G., Dall’Ara, S., Bartolomei, I., Salvi, F., 2009. Chronic cerebrospinal venous insufficiency in patients with multiple sclerosis. *Journal of Neurology, Neurosurgery, and Psychiatry* 80, 392–399. [cited at p. 4]
- Zhang, X., Adamson, R., Curry, F., Weinbaum, S., 2006. A 1-D model to explore the effects of tissue loading and tissue concentration gradients in the revised Starling principle. *American Journal of Physiology - Heart and Circulatory Physiology* 291 (6), H2950–H2964. [cited at p. 21]

Index

- adherens junctions, 3
- albumin, 65
- astrocytes, 4

- basement membrane, 4
- blood-brain barrier, 3
- boundary value problem, 32
- breakdown of the blood-brain barrier, 4

- connective layer, 1
- Crank-Nicolson scheme, 73

- diffusional permeability coefficient, 5

- efficiency, 35
- endothelial cells, 3
- endothelium, 1
- equivalent parameters, 38

- fenestrae, 1
- filtration coefficient, 5
- finite difference scheme, 32, 73
- Freeze's scheme, 32

- glycocalyx, 2

- Heaviside step function, 78
- hemorrhage, xxi
- hydraulic conductance, 5
- hydraulic conductivity, 5
- hydraulic permeability, 5
- hydrostatic pressure, xxi
- hypertension, 48
- hypovolemia, 64

- initial value problem, 32
- inter-cellular cleft, 1

- interstitial fluid, xxi

- Lambert W function, 27, 79
- lymphatic system, xxi

- microalbuminuria, 48
- middle layer, 1

- net pressure, 10
- neuro-vascular unit, 4
- Newton-Raphson method, 27

- oedema, xxi
- omega function, 27, 79
- ordinary differential equation, 78
- osmotic pressure, xxi

- Péclet number, 31
- partial differential equation, 77
- pericytes, 4
- permeability coefficients, 5
- product logarithm, 27, 79
- protein wash-down, 63
- proteinuria, 48

- reflection coefficient, 6
- Runge-Kutta schemes, 33

- shooting scheme, 32
- specific storage, 68
- Starling's forces, 63
- Starling's law, 21

- tight/occludens junctions, 3
- trans-cellular pores, 1
- travel time, 17

- van't Hoff law, 67
- vesicles, 1